# AN INVESTIGATION INTO THE ROLE OF COMPOUNDS AFFECTING FRICTION, WEAR AND LUBRICITY

Gerhard Marais

# AN INVESTIGATION INTO THE ROLE OF COMPOUNDS AFFECTING FRICTION, WEAR AND LUBRICITY

by

Gerhard Marais

A dissertation submitted in partial fulfilment
of the requirements for the degree

**Master of Engineering (Chemical Engineering)**

in the

Department of Chemical Engineering

University of Pretoria
Pretoria

**15 December 2010**

# Synopsis

The *high frequency reciprocating rig (HFRR)* is typically used to determine the lubricity of diesel fuels and has been accepted as the universal test apparatus in most countries of the world. A study was undertaken to analyse results obtained with the *HFRR* instrument by identifying crucial factors contributing to friction and wear mechanisms during a lubricity test under given conditions that may lead to a better understanding of test results obtained. The transient temperature distribution on a semi-infinite disk due to a *circular continuous oscillatory heat source* was also modelled. The model was used to calculate the contact temperature of a contact similar to what can be expected in the *HFRR* apparatus.

For lubricated tests a mixture of n-hexadecane (cetane) as base fluid and palmitic acid as lubricity additive was used. Experimental results, including results obtained by running unlubricated (dry) tests and results obtained from literature were all considered to formulate the hypothesis that a fully functional additive film will not survive the full duration of the lubricity test, which is *75 minutes* (ISO 12156-1, 2003). Friction values obtained in the experiments conducted were much higher than what is expected for boundary films formed by long chain carboxylic acids. Comparable friction values were obtained in the first few seconds of the tests, but the friction values increased indicating the destruction of the boundary film. Metal oxide lubrication dominates for the remainder of the test. Information of the exact mechanism prevailing in the crucial first few seconds of the test should be obtained by increasing the data acquisition rate of the apparatus. It is believed that *junction growth* through *adhesion* is the dominant factor in the initial stages of the test. *GC×GC/TOF-MS* showed the formation of hexane and heptane, which is a strong indication of the catalytic decomposition of the $C_{16}$-hydrocarbons in the sample.

KEYWORDS: adsorption, boundary lubrication, contact temperature, diesel lubricity, *HFRR*, palmitic acid.

# Acknowledgements

The author would like to thank Professor Philip de Vaal for his valuable guidance and support during this project.

I would also like to thank SASOL for the opportunity to take part in this challenging but rewarding project and also for the funds made available for the purchase of new machinery. Thank you very much.

Thank you also to the National Research Foundation for additional funding that they contributed to the purchase of new machinery, through their THRIP-initiative.

Special thanks to Dr. Pedro Gonnet for valuable inputs regarding some of the modelling problems encountered.

Another word of thanks also to Professor Egmont Rohwer and Elize Smit from the Department of Chemistry at the University of Pretoria for their help concerning the *GC×GC/TOF-MS* tests performed in this investigation.

# Table of Content

# Nomenclature list

| | | |
|---|---|---|
| $A$ | Area or bearing area | $m^2$ |
| $A$ | Amplitude of oscillation | $m$ |
| $A_m$ | Asperity contact area | $m^2$ |
| $A_t$ | Total real area of contact | $m^2$ |
| $b$ | Journal bearing length | $m$ |
| $c$ | Bearing clearance | $m$ |
| $C_p$ | Specific heat capacity | $J/kg.K$ |
| $E$ | Young's modulus / Modulus of elasticity | $GPa$ |
| $F$ | Friction force | $N$ |
| $k$ | Thermal conductivity | $W/m.K$ |
| $r$ | Journal bearing radius or normal radius | $m$ |
| $r_{asp}$ | Heat partition coefficient of asperity | - |
| $r_{plate}$ | Heat partition coefficient of plate | - |
| $R$ | Universal gas constant | $J/gmol.K$ |
| $p_m$ | Asperity contact pressure | $Pa$ |
| $p, P$ | Pressure | $Pa$ |
| $p_o$ | Yield pressure | $Pa$ |
| $Q$ | Heat | $J$ |
| $\dot{q}_s$ | Heat flux at the surface | $W/m^2$ |
| $s$ | Shear strength of material | $Pa$ |
| $S$ | Probability variables | - |
| $t$ | Time | $s$ |
| $t'$ | Time of application of heat source | $S$ |
| $T$ | Frictional torque | $N.m$ |
| $T$ | Temperature | $°C$ |
| $\Delta T_m$ | Flash temperature | $°C$ |
| $T_b$ | Bulk fluid temperature | $°C$ |
| $T_m$ | Asperity contact temperature | $°C$ |

| | | |
|---|---|---|
| $v$ | Sliding or entrainment velocity | *m/s* |
| $W$ | Load | *N* |
| $x, y, z$ | Displacement in specific direction or position | *m* |
| $x_o, y_o, z_o$ | Original position | *m* |
| $x', y', z'$ | Position of heat source | *m* |

Greek

| | | |
|---|---|---|
| $\alpha$ | Pressure coefficient for viscosity | $Pa^{-1}$ |
| $\rho$ | Density | $kg/m^3$ |
| $\theta$ | Angle | *rad* |
| $\phi$ | Dimensionless $\tau = t - t'$ | - |
| $\phi$ | Shear activation volume | $m^3$ |
| $\Phi$ | Dimensionless time | - |
| $\tau$ | Shear stress | *Pa* |
| $\tau$ | t – t' | *s* |
| $\tau_m$ | Asperity contact shear stress | *Pa* |
| $\eta$ | Dynamic viscosity | *Pa.s* |
| $\omega$ | Angular velocity | *rad/s* |
| $\omega$ | Frequency of oscillation | $s^{-1}$ |
| $\mu$ | Friction coefficient | - |
| $\kappa$ | Thermal diffusivity | $m^2/s$ |
| $\upsilon$ | Poisson ratio | - |
| $\upsilon$ | Effective vibrational frequency of molecule | $s^{-1}$ |
| $\gamma$ | Adhesion or surface energy | $mJ/m^2$ |
| $\Omega$ | Pressure activation volume | $m^3$ |
| $\Omega$ | Surface over which the heat source acts | $m^2$ |

# Chapter I

# INTRODUCTION

## 1. Background

In modern diesel engines the fuel also fulfils the role of the lubricant in the fuel distribution system. Ever-increasing operating temperatures and pressures that are necessary to ensure optimal combustion in terms of both engine efficiency and environmental legislation, have placed new demands on the properties of diesel fuels - specifically those related to friction and wear. Traditional crude oil-based diesel has good inherent lubricity due to the high content of aromatic and polar oxygenated compounds, but through the process of desulphurisation - to comply with environmental legislation - these compounds are removed, having a detrimental effect on the lubricity of the fuel (Oláh, Szirmai and Resofszki, 2005). In the Fischer-Tropsch (FT) process the synthesis gas also undergoes desulphurisation due to the fact that sulphur poisons the FT catalyst. During product work-up hydrotreatment and hydrogenation cause the loss of more polar and unsaturated compounds, yielding a low lubricity FT diesel (Schaberg *et al.*, 1999). Additives are therefore needed to improve the lubricity of both crude oil diesel and synthetic diesel to comply with local and international diesel specifications like SANS 342, ASTM D975 and EN 590. Dosing of additives needs regulation and is expensive for refineries.

Laboratory-based lubricity tests need to be conducted under conditions that correspond as closely as possible to the prevailing conditions in the practical application, but at the same time need to be completed within a reasonable time – conflicting requirements, since the more extreme the conditions, the shorter the duration of the test, but the further the test conditions are removed from the practical application. Currently, local and international diesel specifications include the ISO 12156 or ASTM D6079 diesel lubricity standard, which utilizes the *HFRR*.

Other laboratory bench tests like the *Scuffing Load Ball-on-Cylinder Evaluator (SL-BOCLE)* and *The Oscillation, Friction and Wear Machine (SRV)* are also used in industry.

## 2. Problem Statement

There are many reported inconsistencies with all the bench tests currently available for diesel lubricity testing. These inconsistencies become even more prevalent when lubricity additives are added to the fuels. Test repeatability for additised fuels have been reported to be up to three times higher than for base fuels (Nikanjam, 1991). Also the effect of additives in these bench tests only becomes detectable at concentrations much higher than necessary in the practical application. The HFRR is believed to underestimate the lubricity properties of diesel, which leads to overdosing of additives with a significant cost implication (Nikanjam, 1991) (Zhmud & Roegiers, 2009) (World Wide Fuels Charter, 2002).

The HFRR, used as specified by ISO 12156-1 (2003) or ASTM D6079 (2005), gives only a single parameter, *the wear scar diameter*, which should be below *460 µm* at the sliding conditions set out by the standard. According to Oláh *et al.* (2005) there is no direct correlation between wear scar size and the physical damage on tribological surfaces after sliding. They report of several cases where a diesel fuel failed in the practical application, whilst having passed the ISO 12156 or ASTM D6079 standard and vica versa.

It is clear that a more fundamental understanding of friction, wear and lubricity - with regard to diesel base fuels and additives - is required.

## 3. Objectives

The objective of this study was to analyse results obtained using the *HFRR* instrument by identifying crucial factors contributing to friction and wear mechanisms

that may lead to a better understanding of interactions between the surfaces and lubricants under the test conditions.

Seeing that all of these mechanisms depend largely on temperature, the goal of this study was also to derive a model that describes the contact temperature profile due to frictional heat generated.

## 4. Method, scope and limitations

The *HFRR* apparatus, as supplied by PCS Instruments, was used as diesel lubricity bench test for all the work in this investigation, seeing that it is the specified test method.

This work only focussed on the lubricity component of the diesel specification. There are several other properties like *flash point*, *density*, *cetane number*, *cold flow properties* and *aromatic content* that also have to be considered to meet the requirements of international diesel standards. In meeting these requirements, compromises will be made regarding lubricity (Schaberg *et al.,* 1999).

A diesel mixture may contain in excess of *10 000* components. For simplification in terms of interpretation of results and mathematical correlation, a binary mixture was used for all experiments. Cetane or n-hexadecane was used as base fuel with palmitic acid as additive.

# Chapter II

# LITERATURE

Jost and Scofield (1981) estimated that the application of tribological principles could help to achieve a national energy saving of between £468 and £700 million per annum in the United Kingdom. A decent understanding of tribology is therefore crucial for the global economy. This chapter gives an outline of the most important literature concerning friction, wear and lubrication from the 1500's to the present day.

Reynolds (1886) developed lubrication theory, based on results of Tower (1883). Noticing both the effects of elastohydrodynamic and boundary lubrication, he realised that these would be extremely difficult to describe mathematically. The interactions in a tribo-contact are so plentiful and localised and fluid and solid properties so far removed from that in the bulk that empirical relations are often as close as we can come to the underlying truth.

This chapter gives a short overview of the different regimes of lubrication as well as physio and chemical surface layers and discusses the effect they have on lubricity. Friction is explained from an atomic viewpoint, which shows that there are strong similarities between solid and liquid friction. A short section on wear is also presented and the chapter ends with an overview of experimental options available for studying diesel lubricity.

---

## 1. Regimes of lubrication: Bulk to molecular lubrication

The ability to reduce both friction and wear of moving machine parts has long been the two most important factors in enhancing component efficiency. Increasingly stringent environmental legislation forces diesel engine manufacturers to increase common rail injection pressures, changing the sliding conditions in diesel injectors. These injectors can fail if the diesel does not have sufficient lubricating properties. **Figure 1** shows the effect of load, liquid viscosity and sliding speed on friction coefficient. The four regimes of lubrication (hydrodynamic, elastohydrodynamic, mixed and boundary) are explained in the next section.

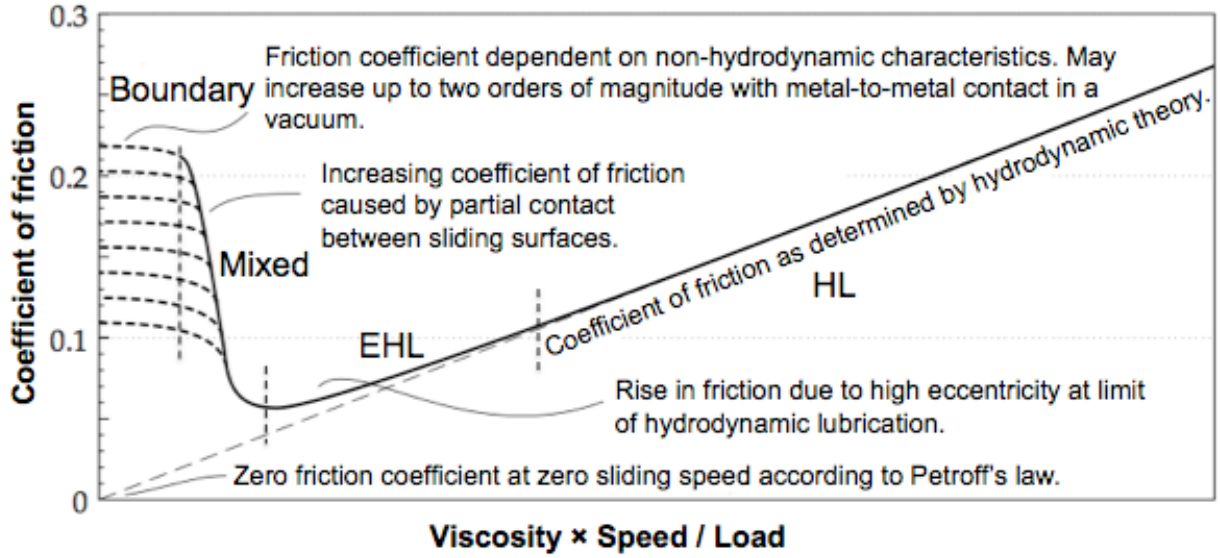


***Figure 1**. The Stribeck curve as adapted from Stachowiak and Batchelor (2005: 183).*

## 1.1. Hydrodynamic lubrication: The history of lubrication theory

Hydrodynamic lubrication is defined as the lubrication mechanism achieved when a viscous fluid film of sufficient thickness is compressed between two surfaces and the hydrodynamic pressure generated is sufficient to prevent the surfaces from touching.

The lubrication of journal bearings became a field of interest in the late 1800's. In 1883 *Petroff's Equation*, named after its founder, was presented as an empirical result of a vast amount of experiments. He found that under certain conditions frictional torque (*T*) is a function of lubricant viscosity ($\eta$), bearing area (*A*), relative velocity (*v*) and clearance (*c*), as indicated by (2.1) (Bhushan, 2002: 435 – 436).

$$T = Fr = \frac{2\pi\eta_o r^3 b\omega}{c} \qquad \text{where} \qquad A = 2\pi rb \text{ and } v = \omega r \qquad (2.1)$$

Therefore friction coefficient ($\mu$) will be a linear function of $v, \eta$ and *P* at a constant bearing clearance as indicated by (2.2) and **Figure 1**.

$$\mu = \frac{T}{W} = \frac{\eta_o vA}{cW} = \frac{\eta_o v}{cP} \qquad (2.2)$$

The mathematical description of hydrodynamic fluid flow was derived by Stokes (1845) and Lord Raleigh, and used by Reynolds (1886) to fit Tower's (1883) journal bearing lubrication results. He derived the *Reynolds Equation*, which forms the theoretical platform on which fluid lubrication modelling is based. There are two conditions for hydrodynamic lubrication (Stachowiak & Batchelor, 2005: 102):

- The two surfaces should have sufficient relative velocity so that a lubricating film, capable of carrying the load, can be formed; and
- The surfaces should be inclined. Parallel surfaces will not form a film capable of supporting the required load, except if they move towards each other squeezing out fluid on the sides.

The *Reynolds Equation* is essentially a simplified momentum balance applied over a cubic fluid particle in three dimensions. The following assumptions were made in the derivation of the *Reynolds Equation* (Stachowiak & Batchelor, 2005: 102) (Bhushan, 2002: 441) (Szeri, 1998: 71):

- Body forces were neglected;
- Constant pressure throughout the film;
- No slip at the boundaries;
- Newtonian fluid;
- Laminar flow;
- Fluid inertia was neglected;
- Constant fluid density (incompressible);
- Constant viscosity throughout generated film; and
- Smooth surfaces.

The full equation will not be derived in this text, but Reynolds (1886), Stachowiak & Batchelor (2005: 103) and Hamrock, Schmid & Jacobson (2004: 181) presented very thorough and "easy to understand" derivations. The Reynolds Equation could be solved for more complex geometries, thermal behaviour and dynamic loading with the development of numerical techniques and the improvement of computational resources. Non-Newtonian behaviour and the effects of surface roughness can also be included in the model and solved within reasonable times on a desktop computer using computational fluid dynamics (CFD) (Spikes, 2004).

From the *Reynolds Equation* it became clear that thick-film lubrication properties were a direct function of the viscosity of the fluid. Reynolds (1886) already appreciated the strong effect that viscosity would have on lubrication theory of the future. For a lack of better words, the following quotation is taken from Reynolds (1886).

> *"The chief question regarding viscosity is a simple one – within a particular fluid is viscosity constant? If it is, our equations may be useful; if it is not then the introduction of viscosity into the equations render them so complex that it is almost hopeless to expect anything of them".*

A fluid is defined by its incapability to sustain tangential or shearing stress. Of course all fluids are capable of sustaining stress at certain conditions of motion, making them mathematically imperfect or viscous. Stress on a fluid particle is caused by force, which will distort the fluid in one or either of the following ways (White, 2006: 19):

- Extensional strain or stretching, which increases or decreases the size of the particle; and
- Shear strain, which changes the shape of the particle from say cubic to rhombic.

The coefficient of viscosity ($\eta$) is the shear stress divided by the rate of distortion.

Viscosity in liquids is primarily due to two types of intermolecular interactions, the interaction between the lubricant molecules themselves and the attachment of lubricant molecules to the surface (Tabor, 1981).

Intermolecular van der Waals dispersion forces are both temperature, pressure and chain length dependent. Polar groups will introduce additional intermolecular forces but these are usually small (Tabor, 1981). Increased temperature results in expansion of the fluid that causes reduction in intermolecular forces and therefore viscosity (Bhushan, 2002: 430) according to the relation in (2.3).

$$\eta = \eta_o \exp\left(-E/RT\right) \tag{2.3}$$

The activation energy ($E$) is dependent on the chain length of the lubricant and the intermolecular forces. For *20 - 30* carbon chains the activation energy reaches a steady

value of between *20* and *25 kJ.gmol*$^{-1}$. In terms of the effect of chain length on viscosity, the viscosity of a homologous series increases linearly with the addition of a carbon up to about *500* carbons. For chain lengths longer than *500* carbons the mechanism of motion changes from segmental to reptation or “snake-like” motion (Tabor, 1981), which is responsible for the viscosity function’s deviation from linearity. Pressure increase for liquids result in compression of a fluid element which forces molecules closer to each other, thereby increasing the intermolecular forces and the dynamic viscosity. The viscosity may change by several orders of magnitude under the effects of pressure. Several authors suggest the relation in (2.4), called the *Barus law* (Bhushan, 2002: 432), (Hu & Zhu, 2000), $\alpha$ is the viscosity-pressure coefficient (*Pa*$^{-1}$).

$$\eta = \eta_o \exp(\alpha P) \tag{2.4}$$

Reynolds (1886) assumed that the no-slip conditions holds for hydrodynamic lubrication, which means that the molecular forces between the wall and the lubricant molecules are strong enough to prevent detachment due to shear. This assumption was based on engineering practise and is generally correct. Viscous heating, as a result of increased pressure, can cause desorption of the lubricant molecules from the surface causing slip, especially on hydrophobic surfaces (Spikes, 2004). Increased pressure causes deviation of the friction coefficient from the *Reynolds Equation* or *Petroff’s Equation* as indicated by **Figure 1** and introduces a more complex lubrication regime: elastohydrodynamic lubrication.

## 1.2. Elastohydrodynamic lubrication

When the contact pressure increases and the sliding speed decreases the fluid is no longer entrained as effectively and the film thickness diminishes to a level where it is smaller than the average height of the surface asperities. Yet the surfaces are kept apart by the fluid. The maximum contact pressure generated in a *high-frequency reciprocating rig* (HFRR) (discussed later), assuming elastic deformation of the surfaces, can be calculated with (2.5) below (Bhushan, 2002: 103).

$$P_{\max}\Big|_{elastic} = \left(\frac{6WE^{*2}}{\pi^3 r^2}\right)^{1/3} \tag{2.5}$$

where $\frac{1}{E^*} = \frac{1-\upsilon_{ball}^2}{E_{ball}} + \frac{1-\upsilon_{disk}^2}{E_{disk}}$ and $\frac{1}{r} = \frac{1}{r_{ball}} + \frac{1}{r_{disk}}$

*AISI E-52100 steel*, the material used for the HFRR specimens, has a Young's modulus of *210 GPa* and a Poisson ratio of *0,3* (MatWeb Material Property Data, 2010). The calculated Hertzian contact pressure is *825 MPa*. Using the *Barus law* of (2.4) and assuming a viscosity-pressure coefficient ($\alpha$) of $10^{-8}$ $Pa^{-1}$ (Tabor, 1981), the viscosity increases by a factor of more than *3 800*. The harder the fluid is pressed, the higher the viscosity and the more difficult it becomes to extrude the liquid. Due to this immense increase in viscosity, it is possible for asperities to elastically deform each other through the liquid film without touching, thereby increasing the bearing area, while preventing wear. The effect of viscous heating at these high viscosities increases desorption of lubricant near the wall leading to wall slip (Spikes, 2004). According to Stachowiak & Batchelor (2005: 281) the mathematical description of EHL needs three components:

- Fluid dynamics theory;
- Elastic deformation of the solid bodies; and
- An equation relating viscosity to pressure like the *Barus Equation*.

EHL calculations are routinely based on the *Reynolds Equation*. The deformation of the solid surfaces and the effect of surface roughness can be included through the film thickness variable present in the *Reynolds Equation* and a viscosity-pressure relation can be included in the description. This is fundamentally wrong seeing that the *Reynolds Equation* was derived under the assumption of constant viscosity. When viscosity becomes a strong function of pressure, which is a function of position, an extra variable - pressure dependent viscosity - is introduced that leads to the addition of two terms in the momentum balance. These terms complicate the momentum balance even further and severe assumptions have to be made to solve them. A study by Rajagopal and Szeri (2003) indicated that proper accounting of the pressure dependence of lubricant viscosity would yield slightly higher pressures and much higher viscosities, relative to the classical Reynolds analysis.

**Figure 1** shows that a bearing operating in EHL will have the lowest possible friction. According to Tabor (1981) this decreased friction is a result of a thermally activated molecular reorientation process, which is dependent on contact pressure and shear rate. This is explained in more detail in the section on friction.

## 1.3. Boundary lubrication

At very high loads, low lubricant viscosity and low sliding velocity the two surfaces come so close together that some asperities come into contact while a thin layer of lubrication alleviates others. This thin layer of lubrication is the last line of defence in which the lubricant's physical and chemical interaction with the solid surface controls friction and wear, therefore the bulk viscosity of the lubricant becomes totally irrelevant. The boundary lubrication regime is considered the regime that controls component life (Bhushan, 2002: 428). The following two quotations taken from Spikes (1993) give very good explanations of boundary lubrication.

> *"In what is often called complete lubrication, the kind of lubrication investigated by Towers and Osborne Reynolds, the solid surfaces are completely floated apart by the lubricant. There is however, another kind of lubrication in which the solid faces are near enough to influence directly the physical properties of the lubricant. This is the condition found in 'dry' or 'greasy' surfaces. What Osborne Reynolds calls 'boundary conditions' then operate and the friction depends not only on the lubricant, but also on the chemical nature of the solid boundaries. Boundary lubrication differs so greatly from complete lubrication as to suggest that there is a discontinuity between the two states."* Sir William Hardy (1922)

> *"…in the case of the heating up of the crankpins of gas engines it is common practise to substitute castor oil for the mineral oil, with the results that the friction diminishes to its normal value and smooth running results. Now the value of viscosity for castor oil does not differ appreciably from that of a good lubricating mineral oil, so it is evident that the former possesses some lubricating property*

*apart from its viscosity. Although considerable attention has been devoted to the study of this property of good lubricants, no definite relation has yet been found between it and other physical properties of the oil, and the property itself is somewhat vaguely referred to as 'oiliness'."* Stanton (1926)

The aim of a boundary lubricant can be summarised with equations (2.6) and (2.7):

$$\mu = \frac{F}{W} \qquad \text{where} \qquad F = A_t s \qquad \text{and} \qquad W = A_t p_o \tag{2.6}$$

$$\therefore \mu = \frac{s}{p_o} \tag{2.7}$$

For a dry adhesive metal contact, where the effect of ploughing is neglected, the friction force ($F$) will be the shear strength of that metal ($s$) multiplied by the real area of contact ($A_t$). All the asperities in contact will deform plastically as a result of the normal force ($W$) and the maximum attainable pressure will be the plastic flow stress or yield pressure of the material ($p_o$). The value of yield pressure is very similar to the indentation hardness of the material. To obtain a low friction coefficient ($\mu$), a material with low shear strength and high hardness is required - conflicting requirements. The aim of the boundary lubricant is to provide a surface with low shear strength while not influencing the hardness of the material (Stachowiak & Batchelor, 2005: 358).

Our current understanding of boundary lubrication leads us to believe that it can be categorised into four mechanisms depending on the conditions of temperature and pressure: *adsorption lubrication*, *surface localised viscosity enhancement*, *amorphous layers* and *sacrificial films*.

At low temperature (up to *150°C*) and high load conditions (up to *1 GPa*) *adsorption lubrication* is most often the mechanism at hand. Physisorption and chemisorption of additive molecules to the surface controls friction and wear (Stachowiak & Batchelor, 2005: 360). Different models for *adsorption lubrication* were developed over the years and generalised to all boundary lubrication mechanisms. In 1922 Hardy proposed the model in **Figure 2**. Bowden and Tabor (1950: 223) proved that metal-metal is contact still present under normal boundary lubrication although friction coefficients were quite

low. Their model is shown in **Figure 3**. Adamson (1990: 479) included the friction contribution of unorganised boundary lubricant near the contact region into his model, shown in **Figure 4**.

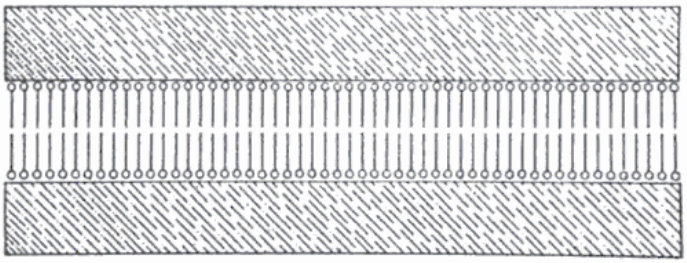

***Figure 2**. Boundary lubrication model suggested by Hardy in 1922. Taken from Bowden and Tabor (1950: 223).*

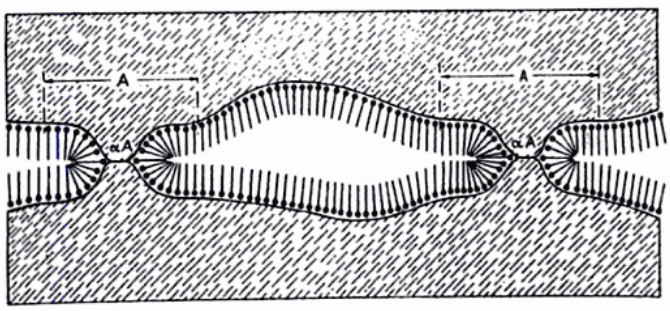


***Figure 3**. Boundary lubrication model suggested by Bowden and Tabor . Taken from Bowden and Tabor (1950: 223).*

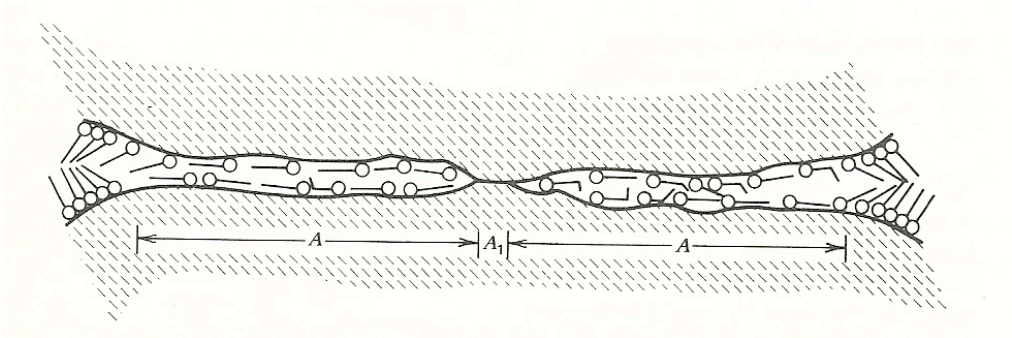


***Figure 4**. Boundary lubrication model suggested by Adamson (1990: 479).*

The primary difficultly with regard to boundary lubrication is temperature. At high temperatures and medium loads *chain matching* improves lubrication. When the additive and the solvent are both paraffinic and they have similar chain lengths the additive

adsorbs to the surface and the solvent aligns itself parallel to the additive in between the adsorbed molecules. Very high loads can be carried if the chain lengths are the same. *Thick films of amorphous layers* also provide good lubrication under these conditions. An example of this is the lubrication of steel with zinc dialkyldithiophosphate (ZnDDP), where amorphous layers of phosphate containing iron and zinc was found (Stachowiak & Batchelor, 2005: 386).

At high-temperature-high-load conditions extreme pressure lubrication is at hand. This mechanism works on the principle of continuous destruction and reformation of a lubricating film, therefore the name *sacrificial films*. An example of extreme pressure lubrication is the formation of iron sulphides on a steel surface. The iron oxides must first be removed to expose clean metal surface onto which the sulphur can react. This process of wear leads to the very high contact temperatures necessary for extreme pressure lubrication (Stachowiak & Batchelor, 2005: 388).

According to Tabor (1981) friction in boundary lubrication is also a result of a thermally activated reorientation process, which is dependent on contact pressure and shear rate. This time only parts of molecules are reoriented as opposed to EHL where the reorientation process involved whole molecules. This is explained in more detail in the section on friction.

## 1.4. Lubricity vs. Viscosity: Mixed lubrication

It is very rare for sliding systems to operate exclusively in the boundary lubrication regime, unless the sliding velocity and the fluid viscosity are very low. Most practical systems operate in the mixed lubrication regime where the load is carried by both boundary films and hydrodynamically-generated pressure (Spikes, 1993). The term “lubricity” usually refers to the condition where friction and wear are determined by the physical properties of the surfaces and the properties of the fluid, other than viscosity (ASTM D6079, 2005). The effect of viscosity can however not be eliminated from any practical contact.

HFRR results often indicate proportionality between measured wear scar diameters (MWSD) and the inverse of viscosity (Wei & Spikes, 1986). Knowing that the HFRR

operates in the mixed lubrication regime, this suggests that viscosity still has a major effect on the wear mechanism. One should however remember that a compound with a high viscosity usually also has a high concentration of polar impurities with good boundary lubrication capabilities so that the effects of the different factors cannot be readily distinguished (Wei & Spikes, 1986).

# 2. Physio-chemical characteristics of surface layers

## 2.1. Surface layers

Any metal surface can be classified into *5* layers. These layers are discussed in the order of decreasing depth, starting with the deepest layer just above the bulk material.

The *deformed layer* is a result of plastic deformation or work hardening and has different properties than the bulk material itself. The effect of work hardening is explained in the section on friction.

The *Beilby layer* is formed during machining of the component where some of the metal or alloy melts and gets quenched by the cooler surface below. This quenched product is hardened and has an amorphous or microcrystalline structure.

*Chemically reacted layers* are usually a result of metal exposure to a gas or vapour. These layers usually consist of oxides, chlorides, sulphides or nitrides depending on the environment. As long as metal surface is exposed, reaction will occur. The chemically reacted layer is also not limited to a monolayer and the thickness depends on the reaction temperature, the reactivity of the compounds and reaction time.

The *physisorbed layer* consists of molecules physically adsorbed to the metal surface or chemically reacted layer. A metal surface at ambient conditions will almost without exception have a physisorbed layer of water vapour on it. These molecules are held in position by weak van der Waals forces and are easily removed by vacuum or by washing the sample with the proper solvent.

The *chemisorbed layer* consists of molecules chemically adsorbed (reacted) by covalent or ionic bonds onto the metal or chemically reacted layer. These molecules are held in position by strong forces and are not easily removed.

The major differences between physisorption and chemisorption are summarised in **Table 1** and also shown in ***Figure 5*** (Bhushan, 2002: 11) (Selwood, 1975: 2).

***Table 1**. Major differences between chemisorption and physisorption.*

| *Physisorption* | *Chemisorption* |
|---|---|
| Multiple layers can be formed. | Limited to a monolayer, but molecules can be physisorbed onto a chemisorbed layer. |
| Takes place at lower temperatures. | Takes place at higher temperatures due to the activation needed. |
| Independent of any action of the adsorbent. | Activity of the adsorbent is important. |
| Non – specific. | Specific. |
| Limited by the rate of diffusion of the adsorbent. | Activation energy is required for the chemisorption to take place. |

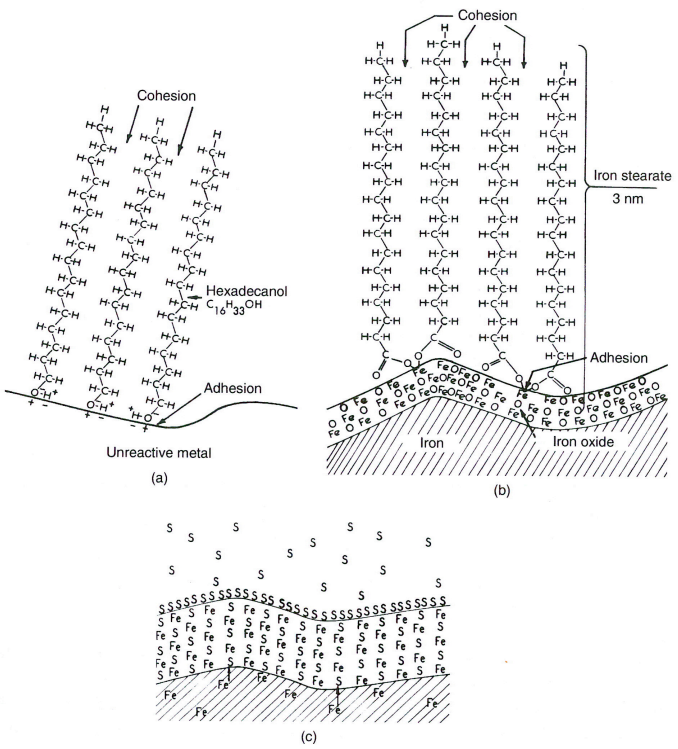


***Figure 5**. (a) Physisorption of three polar hexadecanol molecules to metal surface; (b) Chemisorption of stearic acid on an iron surface to form a monolayer of iron stearate; (c) A chemically reacted inorganic film of iron sulphide (Bhushan, 2002: 535).*

In the case of platinum lubricated by lauric acid, effective lubrication was only possible up to a temperature of *70°C*, which corresponds to the melting point of lauric acid. The lauric acid was physisorbed to the platinum surface due to the inertness of the surface. When a copper surface was lubricated by lauric acid, the critical temperature of lubrication was around 95°C, which corresponds to the melting point of copper laurate. The transition temperature increases with increase in acid chain length. The presence of a partially irreversible soap film indicates that chemisorption took place on the surface (Stachowiak & Batchelor, 2005: 364).

Stachowiak and Batchelor (2005: 381) reported a friction transition temperature for palmitic acid and cetane of *240°C* where for other acids dissolved in cetane the transition temperature was between *120°C* and *160°C*. This high transition temperature is a result of *chain matching*.

## 2.2. Adsorption of polar additives in a tribological contact

According to Bowden and Tabor (1950: 200) the adsorption of fatty acids onto steel is only effective if an oxide layer is present on the surface. Fatty acids show no better performance in lubricating inert metals than non-polar paraffinic molecules. According to Stachwiak and Batchelor (2005: 365 - 370) the reactivity of the metal is very important. On inert metals, such as platinum and silver, no oxide layer or chemisorbed layer is formed. On very reactive metals, such as iron, oxides are formed very rapidly, but these metals are so reactive that they act as catalysts for the decomposition of organic compounds to gases such as methane, carbon monoxide and hydrogen under severe sliding conditions. In other words they destroy the lubricant. The presence of an oxide layer decreases the reactivity of the surface to such a level that chemisorption can take place.

The chemisorption of fatty acids onto oxides leads to formation of metal soaps. Their polarity allows strong adsorption that ensures that almost all available surface sites are occupied, almost independent of the amount of surface sites already occupied (Stachowiak & Batchelor, 2005: 362), therefore this adsorption will tend to be of the

simple *Langmuir* type (Adamson, 1990: 429). According to Tabor (1981) the formation of a multilayer under friction conditions is not likely.

### 2.3. The effect of oxygen and water on the lubrication of metal surfaces

Oxygen and water will always be present in a lubricating system unless an effort is made to remove them. The effect of oxygen and water on lubrication will have a strong dependence on the metal surface used, as explained above. With the exception of noble metals, contact between oxygen and a metal surface will lead to an immediate generation of an oxide layer on the surface that will become hydrated by a physisorbed layer of water. Wear of this oxide layer exposes nascent metal surface, which is oxidised rapidly if the contact is air lubricated. In the case where a steel contact is liquid lubricated it may take a few seconds for the oxide layer to reform. In this time no chemisorption is possible and the clean metal surface acts as a catalyst for organic decomposition (Stachowiak & Batchelor, 2005: 369). The presence of oxygen and water is therefore crucial to the lubrication of steel surfaces. Water, however can have an extremely negative impact if its concentration is high enough to form a free water phase.

## 3. Friction

Friction is the force resisting relative motion of solid surfaces or fluid layers sliding over each other. The first important realisation with regards to friction is that it is not a fundamental force like, for instance, gravity. Friction is the dissipation of energy from the contact area as a result of molecular collisions across the interface (Yoshizawa, Chen & Israelachvili, 1993).

Leonardo da Vinci (1452 - 1519), Guillaume Amontons (1706), Bernard de Bélidor (1737), Leonard Euler (1748) and Charles-Augustin de Coulomb (1780, 1785) were the early pioneers of friction studies (Yoshizawa, *et al.*, 1993). The three laws of friction are mentioned below (Szeri, 1998: 8):

*Amontons 1$^{st}$ Law*: The friction force is proportional to the normal force in sliding;

*Amontons 2nd Law*: Friction force is independent of apparent contact area; and
*Coulomb's Law*: Kinetic friction force is independent of sliding velocity.

In mixed lubrication, three distinct friction mechanisms interact with each other, namely *metal-to-metal friction*, *boundary film friction* and *viscous friction*. *Viscous friction* is not discussed here, but whether the fluid is Newtonian or non-Newtonian the *viscous friction* force is proportional to the applied load, even for very small loads. For metals and boundary films there is a finite "yield stress" that must be applied before motion can start (Yoshizawa, *et al.*, 1993). All of these mechanisms of friction have one thing in common: molecular interaction between contacting surfaces or *adhesion* (Ludema, 1996: 92).

## 3.1. Metal-to-metal friction: Adhesion of metal surfaces

*Metal-to-metal friction* can be divided into three mechanisms (Szeri, 1998: 9):

- The force to shear adhesive junctions between contacting metal surfaces;
- Asperity plastic deformation, which is the main contributor to static friction; and
- Ploughing, which is the force required to make a softer material flow ahead of an advancing hard asperity.

These three friction mechanisms are responsible for the two most destructive wear mechanisms: *adhesive* and *abrasive wear*, which will be discussed in more detail later. Adhesion between *clean* metal surfaces can be decreased by minute contamination with water, oxygen or lubricant. Adhesion also decreases with increased surface roughness and hardness (Stachowiak & Batchelor, 2005: 533). Surfaces of the same metals experience great adhesion as both surfaces undergo plastic flow, which increases the contact area and mutual welding of the two surfaces occurs (Bowden & Tabor, 1939).

When two clean metals are brought into contact by a normal force, intimate contact occurs at the asperities. Asperities deform elastically up to the elastic limit where plastic deformation starts below the surface. As the load increases the plastically deformed area propagates upwards to the surface until the whole contact area is plastically deformed and the average contact pressure is equal to three times the yield strength of

the material. If an asperity radius of *1 μm* is assumed, a load of less than *1 mN* is sufficient to cause plastic deformation (Szeri, 1998: 1) (Stachowiak & Batchelor, 2005: 468).

When the influence of ploughing is neglected, the friction is shown by (2.7) as discussed earlier.

$$\mu = \frac{s}{p_o} \tag{2.7}$$

According to Tabor (1959) the value of the friction coefficient for *clean* metals should be around *0,2* if (2.7) is used ($s = p_Y/2$ and $p_o = 3p_Y$). Experimental results on *clean* metal surfaces yield friction coefficients of up to *10*. The effect of work-hardening will have a negligible effect on friction coefficient seeing that it increases both the interfacial shear strength and $p_o$, which is why surface hardness has no effect on friction coefficient (Tabor, 1959). The discrepancy in (2.7) led Tabor to consider the *combined* effect of normal and tangential stresses.

### 3.1.1. The role of combined stresses: Junction growth (Tabor, 1959)

When two *clean* metal surfaces are loaded onto each other with a load, *W*, and the deformation is plastic (yield pressure, $p_o$), the contact area will increase up to a point where it can just support the load over an area $A_o$. Upon application of a tangential force, *F*, a tangential stress, *s*, is applied. The criterion for plastic flow in a real contact is shown in (2.8). When $s = 0$, $p = p_o$ which means that $K = p_o$.

$$p^2 + \alpha s^2 = K^2 \Rightarrow p^2 + \alpha s^2 = p_o^2 \tag{2.8}$$

Application of a tangential force will increase the contact area from $A_o$ to *A*. This increase in area will cause *p* to drop, and therefore *s* should increase to keep the contact plastic. All of this happens before the onset of macroscopic sliding.

The presence of contaminants like oxides or lubricant will cause junction growth to end sooner thereby limiting *adhesion*, but the behaviour of clean and lubricated surfaces

are almost identical in the initial stages of junction growth. As long as the shear strength of the interface is larger than the stress required to keep the junction in a plastic state the junction area will continue to grow. When the shear stress reaches the shear strength of the interface, macroscopic sliding occurs. This does not necessarily mean that the boundary film should be penetrated, although some penetration may occur. The boundary film will possess some finite shear strength and junction growth can continue up to this shear strength just as for unlubricated contacts.

The basic equation for junction growth is derived below with the use of **Figure 6**.

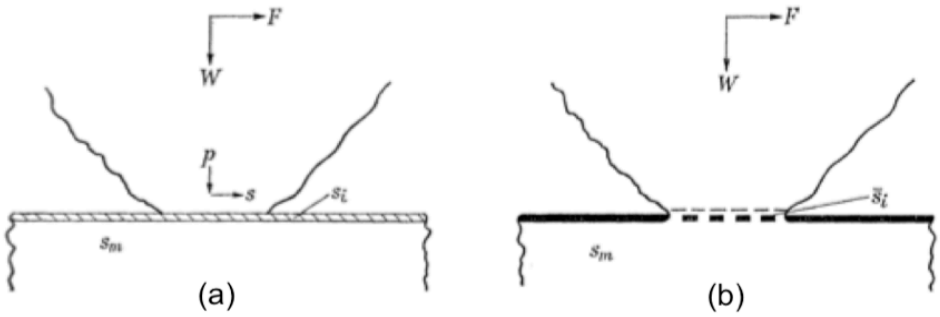


***Figure 6**. (a) Junction growth stops when the shear stress reaches the interface shear strength, $s_i$. (b) In a real contact, where load is carried by boundary film, clean metal and oxides the interface strength is depicted by $\bar{s}_i$ (Tabor, 1959).*

For a three-dimensional contact (axially symmetrical), equation (2.8) is the criterion for plastic flow. $p_o$ will be some multiple of the shear strength of the bulk metal, $s_m$ and sliding will occur when the shear stress, $s$, is equal to the interface shear strength, $s_i$. Therefore equation (2.9) will be the condition for macroscopic sliding.

$$p^2 + \alpha s_i^2 = \alpha s_m^2 \tag{2.9}$$

When the assumption is made that $s_i = k s_m$, where $k$ is less than unity, the friction coefficient will be as shown in (2.10).

$$\mu = \frac{F}{W} = \frac{s_i A}{pA} = \frac{s_i}{p} = \frac{1}{\sqrt{\alpha\left(k^{-2} - 1\right)}} \tag{2.10}$$

According to (2.10) when *k* = *1,* implying *clean* metal surfaces, $\mu \to \infty$, but a small reduction in *k*, will cause a massive drop in friction coefficient. This drop is so great that the value of *α* has very little importance. When *k* = *0,95* the friction coefficient drops to around unity, which supports experimental observations.

During the early stages of lubricated metal contact some film material of critical shear stress, $s_i$ and some metal with shear strength, $s_m$, are important in the contact. The average shear strength of the contact, $\bar{s}_i$, is used as in **Figure 6(b)**.

In order to prevent adverse friction, one has to minimise the extent to which *adhesion* takes place, which means that junction growth should be limited (Ludema, 1996: 90). *Adhesion* will cause the formation of transfer particles, which can cause *abrasive wear* by ploughing. Ploughing was neglected by Tabor (1959), but will be a function of the extent of *adhesive wear*. This is mentioned here but not considered further.

### 3.1.2. The six stages of friction

The six stages of friction experienced when two metals are brought into contact and a tangential force is applied, are shown in **Figure 7**.

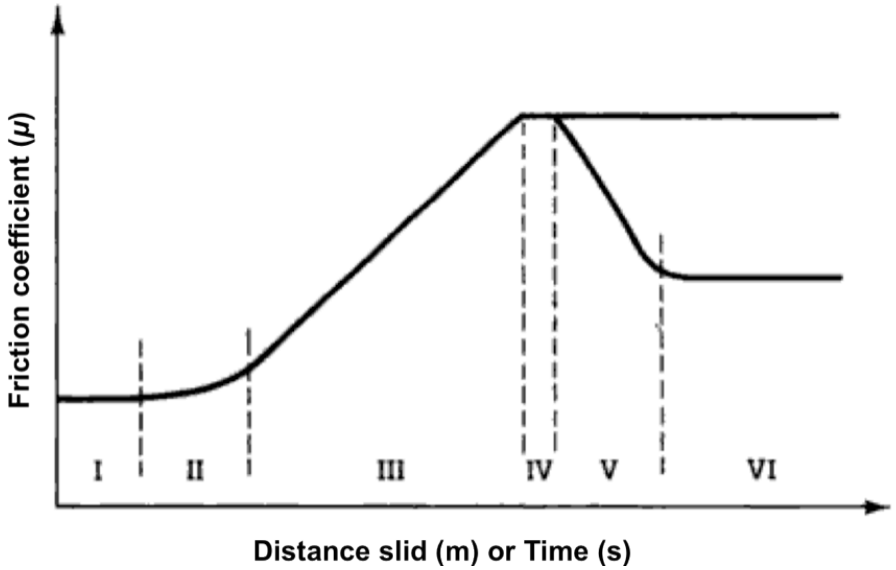


***Figure 7****. The six stages of friction (Szeri, 1998: 21).*

The first stage (*I*) of friction involves ploughing of the surfaces by asperities. Ploughing of the surfaces exposes clean metal due to wear of oxide layers or other contaminants.

Strong metal *adhesion* results in increased friction coefficients (*II*) (*III*). Another cause of the increase in friction could be due to the *abrasive* nature of work hardened wear particles trapped in the contact. At some stage plastic deformation will cease to happen as most of the asperities have been levelled out (*IV*) and the load is supported elastically over a larger area of contact (*V*) (*VI*). Very little *adhesion* occurs which decreases the friction coefficient.

## 3.2. Shear strength of boundary films: Adhesion of lubricant molecules

The frictional response of boundary lubricants is known to be a stress-aided thermally activated phenomenon (Tabor, 1981) (Briscoe & Evans, 1982). The mechanism is not only dependent on temperature, normal force, contact area and velocity, but also chemistry effects like saponification, chain length and polarity, which will determine orientation and intermolecular forces.

Several authors have performed experimental analysis of the frictional processes of different boundary lubricants (Briscoe *et al.*, 1973) (Briscoe & Evans, 1982) (Tabor, 1981) (Timsit & Pelow, 1992) (Yoshizawa, *et al.*, 1993) (Subhalakshmi *et al.*, 2008). Most of these experiments were performed with glass or mica surfaces for two reasons:

- Very smooth surfaces can be obtained with glass or mica. Surface roughness is a very important factor seeing that the monolayer thickness of acids and soaps are usually less than *5 nm*; and
- Optical methods were used to measure the surface area and film thickness.

For these experiments to give a true approximation of the shear strength of boundary films, surface contact and wear had to be eliminated. A short summary of their findings is presented.

### 3.2.1. The effect of pressure

The following example gives a good explanation of the pressure dependency of shear strength: A tin surface and a steel surface has an indentation hardness of *7 kg/mm*$^2$ and *700 kg/mm*$^2$ respectively. If both surfaces were lubricated with a metallic soap film under load, the tin surface would have a *100 times* greater area over which friction could take place, yet the friction coefficient differs by no more than a factor of 2. This gives an indication that the shear strength of the film increases as the pressure increases (Tabor, 1981).

The effect of pressure on the shear strength of polymers, acids and metallic soaps was determined by keeping the sliding velocity constant. The temperature of the contact was also assumed to be constant. This is a valid assumption seeing that the sliding velocities used by the experimenters were in the order of micrometres per second. This assumption may not be valid at higher velocities. The shear strength was found to be proportional to the contact pressure. The results could be represented by (2.11).

$$\tau = \tau_o + \alpha P \tag{2.11}$$

where $\tau_o$ is the shear strength at atmospheric pressure. According to Tabor (1981) the value of $\alpha$ lies between *0.05* and *0.1* for a very wide range of film materials.

### 3.2.2. The effect of temperature

A challenge experienced in determining the $\tau$-$T$ relationship of polymers, organic acids and metallic soaps, was the degradation of these molecules at even moderate temperatures. Changes in palmitic acid film thickness and refractive index were evident from temperatures as low as *40°C* (Briscoe & Evans, 1982). Experiments were carried out at constant pressure and sliding velocity and the relation in equation (2.12) was found.

$$\tau = \tau_o^{'} - \beta T \tag{2.12}$$

The shear strength of all films was found to decrease with increasing temperature. The results used in obtaining the relation were obtained before oxidative degradation occurred.

### 3.2.3. The effect of velocity

The effect of velocity on the shear strength of organic acid and metallic soap films were determined at very low velocities and within very small ranges. The relation is shown as (2.13).

$$\tau = \tau_o^{''} + \theta \ln v \qquad (2.13)$$

Briscoe and Evans (1982) used sliding velocities of *0 - 3 µm/s* and Subhalakshmi (2008) used velocities of *12 - 15 nm/s* with lateral force microscopy (LFM).

### 3.2.4. Friction on a molecular level: Adhesion of molecules

According to Yoshizawa *et al.* (1993) friction is related to *adhesion hysteresis*. This is explained with the help of **Figure 8** and **Figure 9**.

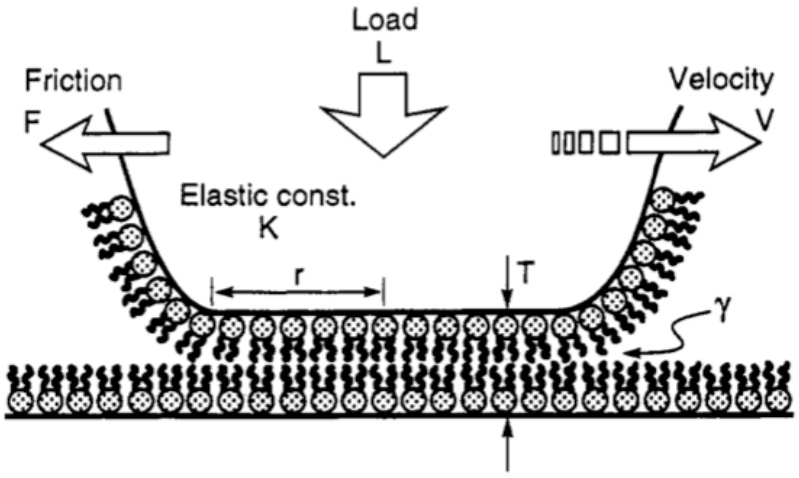


***Figure 8**. A tribological contact with adsorbed or reacted boundary film on each of the contacting surfaces (Yoshizawa et al., 1993).*

*Adhesion* measurements are usually made with a loading-unloading or advancing-receding process. A characteristic of strong *adhesion* is that the unloading or receding force is larger than the loading or advancing force, implying that more bonds had to be broken upon separation than were formed on coming into contact. In a sliding tribological contact a similar phenomenon occurs, only laterally instead of vertically. The front of the contact experiences a loading condition where the back experiences an unloading condition. Yoshizawa *et al*. (1993) found a good correlation between frictional energy and the difference in *adhesion* or surface energy ($\Delta\gamma$).

*Adhesion hysteresis* can be contributed to interdigitation of molecular groups by thermally activated interdiffusion, interpenetration, chain entanglement or reorientation. “Liquid-like” films and totally frozen “solid-like” films show very low *adhesion hysteresis* and therefore quite low *μ*. “Amorphous-like” films show high *adhesion hysteresis* coupled with high values of *μ*. This is explained with the help of **Figure 9**.

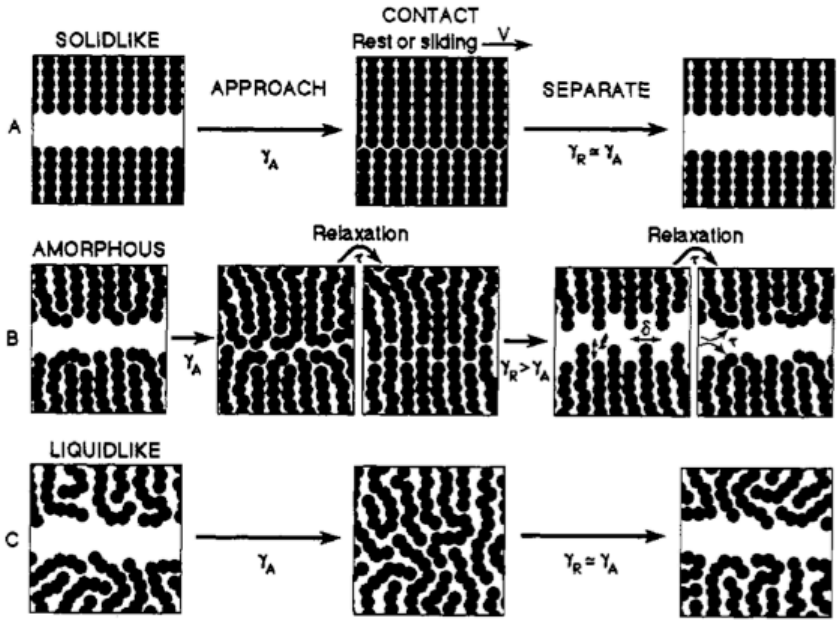


***Figure 9**. Friction and adhesion mechanisms representation for (A) solid-like films, (B) amorphous films and (C) liquid-like films (Yoshizawa et al., 1993).*

For solid-like films there is very little chain interdigitation which leads to very little energy transfer between the molecules. This results in low friction. For amorphous-like films the inverse of the characteristic interdigitation relaxation time ($\tau$ in **Figure 9**), which

is equal to $v/\delta$ laterally and $v/\ell$ vertically, where *v* is the sliding speed, is very close to the effective vibrational frequency of the molecule ($\upsilon$). Therefore the molecules have enough time to interdigitate as they pass each other, but not enough time to completely disentangle. This leads to the maximum friction coefficient possible for the system at that temperature. Liquid-like films are significantly interdigitated and the inverse of their entanglement and disentanglement times are much larger than the effective vibrational frequency of the molecule, which means that the system is always close to equilibrium leading to low friction (Yoshizawa *et al.*, 1993) (Tabor, 1981) (Briscoe & Evans, 1982).

The molecular interactions can be explained mathematically with use of the Eyring equation discussed in the next section.

### 3.2.5. The Eyring equation

In 1935 Henry Eyring developed a mathematical model for activated processes, similar to the Arrhenius relation, and adapted it to describe the viscosity of liquids and the plasticity of solids in 1936. The model works on the principle that, in the case of solids for example, plastic deformation takes place by discreet processes involving small numbers of molecules. The motion of each molecule is restricted by the presence of neighbouring molecules. This potential barrier is overcome by applied shear stress and thermal activation. The model was adapted to describe the shear properties of organic boundary films. The model, as derived by Briscoe and Evans (1982), is presented below:

The inverse of the average time for a molecule to move across the potential barrier is shown in equation (2.14).

$$\frac{1}{t} = \upsilon \exp\left(-\frac{Q' + P\Omega - \tau\phi}{kT}\right) \qquad (2.14)$$

where t = Time (*s*);

$\upsilon$ = Effective vibration frequency of molecule ($s^{-1}$);

*Q'* = Activation Energy (*J/molecule*);

$\Omega$ = Pressure activation volume ($m^3$);

$\tau$ = Shear stress (*Pa*);

$\phi$ = Shear activation volume ($m^3$);

*k* = Boltzman constant = $1{,}381\times10^{-23}\ J.molecule^{-1}.K^{-1}$ (The Boltzman constant is the gas constant divided by Avogadro's number)

The average velocity of a molecule crossing the potential barrier over a distance, *b*, can be calculated by use of equation (2.15), which considers the effect of shear in the positive and negative direction of movement.

$$v_{mol} = \upsilon b \exp\left(-\frac{Q^{'} + P\Omega}{kT}\right)\exp\left(\frac{\tau\phi}{kT}\right) - \upsilon b \exp\left(-\frac{Q^{'} + P\Omega}{kT}\right)\exp\left(-\frac{\tau\phi}{kT}\right)$$

$$\therefore v_{mol} = 2\upsilon b \exp\left(-\frac{Q^{'} + P\Omega}{kT}\right)\left(\frac{\exp\left(\frac{\tau\phi}{kT}\right) - \exp\left(-\frac{\tau\phi}{kT}\right)}{2}\right) \qquad (2.15)$$

$$\therefore v_{mol} = 2\upsilon b \exp\left(-\frac{Q^{'} + P\Omega}{kT}\right)\sinh\left(\frac{\tau\phi}{kT}\right)$$

Of course there is no means to measure molecular velocity, but sliding velocity is a known value and is proportional to the molecular velocity. Equation (2.16) is adapted to include sliding velocity, *v*, and an unknown velocity, $V_o$.

$$v = 2V_o \exp\left(-\frac{Q^{'} + P\Omega}{kT}\right)\sinh\left(\frac{\tau\phi}{kT}\right) \qquad (2.16)$$

Experimental work shows an exponential dependence between shear stress and velocity (Briscoe, Scruton & Willis, 1973) (Briscoe & Evans, 1982). An assumption is made that:

$$\frac{\tau\phi}{kT} > 1$$

The hyperbolic sine function can be simplified to an exponential function as in (2.17) and upon substitution and rearrangement the Eyring equation is obtained in (2.18)

$$\sinh\left(\frac{\tau\phi}{kT}\right) \approx \frac{1}{2}\exp\left(\frac{\tau\phi}{kT}\right) \tag{2.17}$$

$$v = V_o \exp\left(-\frac{Q^{'} + P\Omega}{kT}\right)\exp\left(\frac{\tau\phi}{kT}\right) \quad \Rightarrow \quad \tau = \frac{kT}{\phi}\ln\left(\frac{v}{V_o}\right) + \frac{Q^{'} + P\Omega}{\phi} \tag{2.18}$$

Briscoe and Evans (1982) and Subhalakshmi *et al.* (2008) have used the Eyring equation with limited success. The reason for this is that $V_o$, $Q'$, $\phi$ and $\Omega$ are not constants. Experimental results obtained by Subhalakshmi *et al.* (2008) indicated that $V_o$, $Q'$, $\phi$ and $\Omega$ should be functions of *T* or *p* or *V* or any two of them or all three of them. These relations are unknown.

### 3.2.6. Pressure ($\Omega$) and shear ($\phi$) activation volumes

According to Briscoe and Evans (1982), the $\tau$-*P* relation, where $\alpha = \Omega/\phi$, yields the most reliable data. The ratio of $\Omega$ and $\phi$ is the parameter that largely controls the frictional force. The stress activation or process coherence volume refers to the size of the segment that moves in the direction of applied shear (Subhalakshmi *et al*., 2008). The volume of a palmitic acid molecule is about *0,4 nm*$^3$ and values obtained for $\phi$ are in the order of *5 nm*$^3$, which indicates that several molecules are involved in the shear process. The pressure activation volume is the increase in volume necessary to permit molecular motion (Briscoe & Evans, 1982). The values of $\Omega$ are in the order of *0,1 nm*$^3$, which is approximately the size of an ethyl group (Briscoe & Evans, 1982).

The larger the ratio of $\Omega/\phi$, the larger the friction will be. The process is explained in terms of frictional work. The potential barrier that accounts for friction is shown below as (2.19) (see equation 2.14).

$$E = Q^{'} + P\Omega - \tau\phi \tag{2.19}$$

The higher the energy (*E*), the higher the friction will be. Application of shear stress ($\tau$) leads to a reorientation of the molecules to obtain the lowest possible shear. This movement is a function of temperature and sliding velocity. Increase in external pressure limits the reorientation of the molecules due to increased confinement and additional energy ($P\Omega$) is needed to achieve the reorientation. Low friction will only occur when a large amount of reorientation does not result in a large increase in the local volume. This is usually the case with longer chain polymers, where inter-chain van der Waals forces are strong and the film is well ordered. With shorter chains, like n-hexadecane, which has no polarity, a large local volume change is necessary to achieve reorientation. Molecules move as individuals, rather than groups as a result of lower inter-chain attractive forces and for this reason the films are highly disordered. Molecules with polarity that attach to the surface are very organised and this leads to very low friction, as in the case of metal soap lubrication.

### 3.2.7. The friction of chemisorbed and physisorbed acids and polymers

According to Bhushan (2002: 14) a chemisorption film is limited to a monolayer on each surface and therefore most of the interaction is assumed to be between the end-groups (-$CH_3$'s) (Tabor, 1981). The chemisorption of palmitic acid to iron oxide is illustrated in **Figure 10**. A palmitic acid molecule occupies an area of around *0,2 nm*$^3$ and has a length of about *2 nm* (Briscoe & Evans, 1982). Tabor (1981) measured a calcium stearate film thickness of around *5 nm*, which remained unchanged under the effect of pressure and shear. This is proof that the chains remain vertically orientated during sliding. It is known that high molecular mass polymers arrange themselves in the direction of applied shear (Tabor, 1981) as shown in **Figure 11**. It seems plausible that in case (a) of **Figure 11** shear is a result of an interaction between the methyl (-$CH_3$) end groups, where in case (b) it is a result of interaction between methylene (-$CH_2$) groups (Tabor, 1981) (Briscoe *et al.*, 1973). These two cases are energetically very similar.

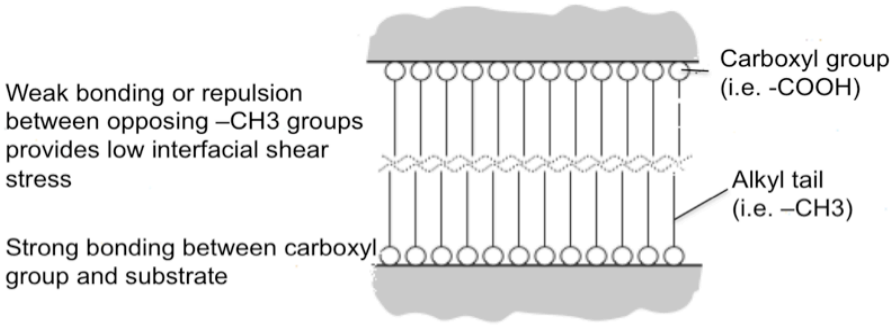


***Figure 10**. Interaction of iron(II)palmitate end groups (Stachowiak & Batchelor, 2005: 362).*

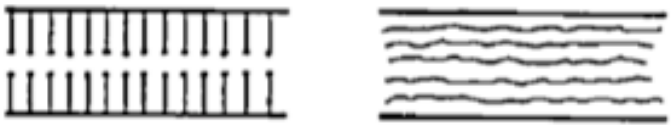

(a) (b)

***Figure 11**. The difference in orientation between an adsorbed hydrocarbon film (a) and a polymer film orientated in the direction of shear (b) (Tabor, 1981).*

Briscoe and Evans (1982) showed that a monolayer of behenic acid ($C_{22}$) and a multilayer of three layers gave similar friction results, provided that an orderly structure of the multilayer is retained. According to Bhushan (2002: 536) viscosity effects become applicable at a film thickness equivalent to between *7* and *10* monolayers. Multilayers also showed similar durability to monolayers. These results proved that there is a single plane of shear in the tribo-contact and that the multiple layers don't shear on each other. This finding makes sense when comparing the similar friction results obtained for long chain polymers and monolayers of stearic acid obtained by Briscoe *et al*. (1973).

A comparison of the shear behaviour of stearic acid compared with calsium stearate deposited on mica surfaces yielded interesting results. $\tau$-*P* tests performed by Briscoe and Evans (1982) showed that the $\tau_o$ value of calcium stearate was higher than for the acid, and that the value of *α* approached zero for calcium stearate compared to a value of *0,038* for stearic acid. The $\tau$-*v* relation changed from an increasing function for stearic acid to a decreasing function for calcium stearate.

# 4. Temperature increase as a result of friction

Temperature has an immense effect on any lubrication process. This is not surprising seeing that on an atomic scale almost all mechanical, chemical and electrical phenomena are dependent on thermal energy to activate or assist them. Furthermore, the effect of degradation of the surface-lubricant system's physical and chemical properties is the main contributor to friction and wear (Bhushan, 2002:287).

Temperature fluctuations have considerable effects on all regimes of lubrication. In hydrodynamic and elastohydrodynamic lubrication, temperature increase causes an exponential decrease in apparent viscosity. It also causes a decrease in the pressure-viscosity coefficient. A reduction in both of these parameters will lead to decreased lubricant film thicknesses. In boundary lubrication the physical and chemical adsorption and desorption equilibrium and kinetics are governed by temperature (Stachowiak & Batchelor, 2005: 327).

In a lubricating system the source of increased temperature, logically, is friction, but what is the mechanism of temperature increase? According to Bhushan (2002: 287) most of the frictional energy, generated by moving surfaces in contact, is used up in plastic deformation in the material close to the surface. Plastic deformation leads to increased lattice vibrations, which are sound waves called phonons. This sound energy is eventually converted to heat. When conditions favour elastic deformation between contacting surfaces, only small energy losses of *0,1%* to *10%* occur by phonons (typically less than *1%*).

A short overview of the history of the development of flash temperature theory is presented below.

## 4.1. Flash temperature history

Man first made use of flash temperatures when he rubbed two sticks together to make fire. The contact area between the two sticks was made to assume the role of a heat source and, with the addition of air, eventually caused fire (Blok, 1963). This is not where the term "flash temperatures" originated though. During a low contact-stress

situation, where the real area of contact is much smaller than the apparent contact area, contact occurs on multiple asperities quite far from each other; for example, if the fraction of contact area to apparent area is *0,001*, the mean pressure may be in the order of *1 GPa* (Blok, 1937). Asperity collision under these high pressures results in numerous high local temperature *flashes* of a very short duration ($10^{-3}$ *s* or less), although the mean temperature rise over the region of nominal contact may be small. These temperature *flashes* have been reported to be in the order of a *1000ºC* (Archard, 1959) and can therefore easily cause surface oxidation, lubricant desorption, phase change in the metal or surface melting. It became increasingly important to know these flash temperatures, despite the mathematical and experimental difficulties encountered in obtaining them. Blok (1937), Carlslaw & Jaeger (1959) and Archard (1959) were some of the researchers who made important contributions to flash temperature theory.

In the modelling concept used in literature (Blok, 1937; Archard, 1959; Bhushan, 2002; Carslaw & Jaeger, 1959) heat is generated by friction and is a function of the relative speed of the two specimens. **Figure 12** is used to explain the concept.

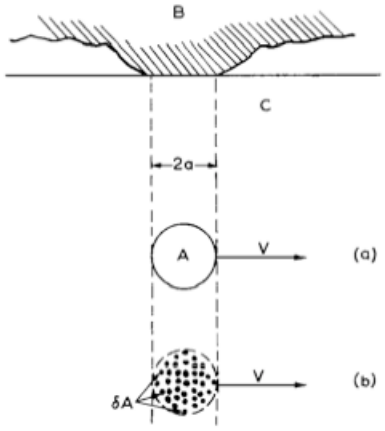


***Figure 12**. A circular asperity contact where body B moves to the right at velocity, v, over a stationary body C. (a) Single large contact, (b) Multiple contact points (Archard, 1959).*

In **Figure 12** the contact area is the heat source and as long as the bodies B and C remain in contact heat will be generated. It is therefore a continuous heat source, which is dependent on the speed of body B. Body B is heated by a stationary heat source,

seeing that relative to B the heat source doesn't move. Body C, however, is heated by a moving heat source and the temperature distribution is highly dependent on velocity. A dimensionless number that incorporates the velocity of each specimen is defined in equation (2.20) and is called the Peclet number (*Pe*), where *v* is the sliding velocity, *κ* is the thermal diffusivity and *a* is the contact dimension (contact radius for circular and contacts and half the width for a rectangular contact etc.) (Stachowiak & Batchelor, 2005: 329).

$$Pe = \frac{va}{2\kappa} \tag{2.20}$$

From **Figure 13** it is clearly visible that the higher the velocity of the heat source the lower the penetration of heat will be into the stationary body. This causes a long "tail" of increased temperature on the surface.

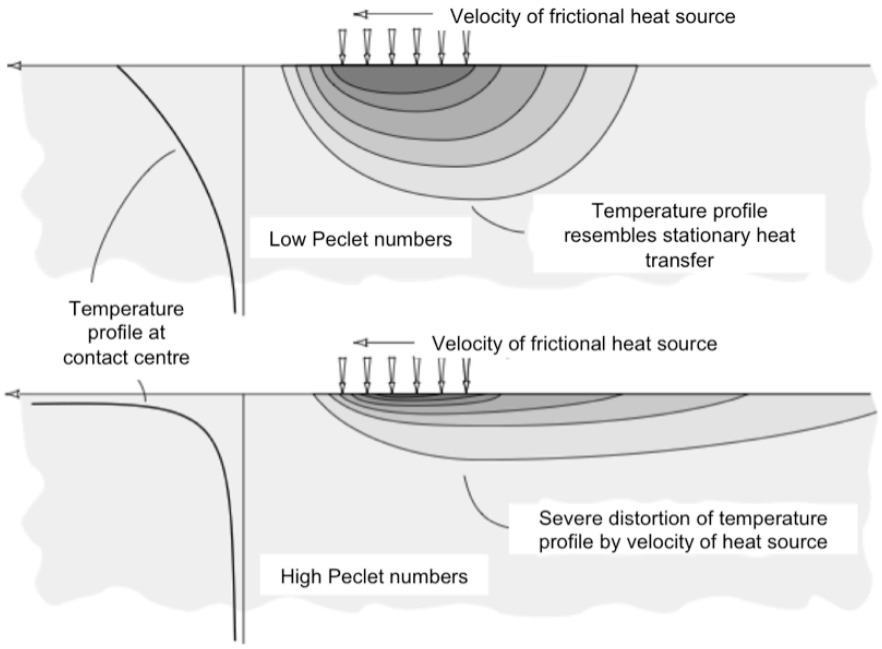


***Figure 13**. Difference in vertical temperature distribution for low and high Peclet numbers (Stachowaik & Batchelor, 2005: 331).*

A look at the system in **Figure 13** from the top will also show that the faster the heat source moves, the smaller the horizontal distribution of heat will be (Archard, 1959). At high velocities the temperature distribution will be independent of the shape of the heat

source and only the cross-sectional width will matter (Bhushan, 2002: 293). Therefore a circular heat source of diameter, *a*, will have the same temperature distribution as a rectangular heat source of width, *a*. This is not the case for low Peclet numbers.

Empirical relations to calculate the temperature distributions due to circular, square, rectangular and line contacts were developed by Archard (1959), Blok (1937) and Jaeger (1943). These equations for average and maximum flash temperatures are only defined for certain Peclet number ranges. There are different equations for $L < 0,1$, $0,1 < L < 5$ and $L > 5$. All these equations were summarized well by Stachowiak and Batchelor (2005: 334). The following assumptions were made:

- Thermal properties of materials are independent of temperature;
- Single contact area regarded as a plane source of heat;
- Frictional heat uniformly generated at the area of contact;
- Heat transfer occurs by conduction of heat into the solids only. The effects of radiation and convection to the lubricant were neglected;
- Flash temperature increase is an effect of plastic deformation only; elastic deformation will not affect any flash temperature changes;
- Coefficient of friction is known and has a steady value; and
- No transient temperature behaviour is taken into account; only steady state values were reported.

These empirical relations cannot be used for an oscillating heat source due to its periodic nature. A model will have to be developed to calculate the periodic HFRR contact temperature.

To simplify the mathematics considerably, one has to assume that there is only a single contact area as opposed to numerous small asperity contacts (**Figure 12**). The modelling approach by Chang (2006) is based on a statistical approach to describe the contact on an asperity level, but this is described later.

Flash temperature theory does not take into account the heat generated by viscous shear. Especially in the elastohydrodynamic lubrication regime, where viscosity can increase by more than a thousand fold, this heat generation accounts for quite a large temperature increase (Archard, 1959).

## 4.2. Partition of heat in a contact situation

In a real contact situation it is the same heat source heating both the top specimen and disk and therefore heat is divided. Exactly how that heat is partitioned is discussed in the section below.

The total amount of heat $q_o$ *(J)* is divided as shown by equation (2.21) and (2.22)

$$Q_s\big|_{asp} = r_{asp} \cdot q_o \qquad \text{and} \qquad Q_s\big|_{plate} = r_{plate} \cdot q_o \tag{2.21}$$

$$\text{where} \qquad r_{asp} + r_{plate} = 1 \tag{2.22}$$

According to Blok (1937) there will be no temperature jump between any point on the top specimen and the point of contact on the disk. There can be only one contact temperature. Therefore, the procedure to calculate the partition fractions, $r_{asp}$ and $r_{plate}$, is to set $T(t)|_{asp}$ equal to $T(t)|_{plate}$ and solve that equation simultaneously with equation (2.22).

When both the top specimen and the disk are heated by a uniform circular stationary heat source, there is no temperature distribution on the surface, and the procedure described above is simple. At higher velocities and periodic functions, though, there is a temperature distribution on the surface of the body heated by the moving heat source. Therefore the one surface has a uniformly distributed temperature while the other has a temperature profile, so that the heat supplies $r_{asp}q_o$ and $r_{plate}q_o$ will not be evenly distributed over the contact (Blok, 1937), which causes a problem.

However, in a pin-on-disk machine, with specimens made from the same material, the interfacial temperature of the disk will be far lower than that of the pin, seeing that the pin moves over cool material at each time interval. The temperature distribution of the surface will therefore be determined by the heat flow of the disk (Stachowiak & Batchelor, 2005: 336). In an oscillating contact though there will be a steady temperature rise in the disk, which again complicates heat partition (Greenwood & Alliston-Greiner, 1992).

# 5. Wear

Wear is defined as the physical removal of material under conditions of load and relative motion. In a tribological application it is wear that causes most of the problems and not friction. Friction is responsible for higher energy consumption, but the energy cost is small compared to the cost of replacing expensive gears and equipment due to failure. High friction does not necessarily mean that high wear rates will be experienced.

## 5.1. Different modes of wear

The mode of wear that often has the most detrimental effect on sliding or oscillating metals in contact is *adhesive wear*. *Adhesive wear* is characterised by very high wear rates and unstable friction coefficients, caused by scuffing and seizure. In extreme cases adhesion may lead to complete seizure. When two metals in direct contact move relative to each other the adhesion between them may be so strong that some metal is transferred from one of the surfaces to the other through a continuous process of “cold welding” and “weld breaking”. Adhesive wear can be minimised by the introduction of a lubricant or a reaction film. These normally promote other forms of wear like *corrosive wear* or *oxidative wear*, which are much milder than *adhesive wear* (Stachowiak & Batchelor, 2005: 542 - 550).

*Corrosive wear* in metals refers to any type of wear associated with a chemical reaction happening on the surface, with *oxidative wear* referring to the corrosion due to atmospheric oxygen. Corrosion in a sliding contact will follow one of the mechanisms mentioned below:

- A durable lubricating film can be formed preventing further corrosion and wear;
- Sacrificial films with a short lifetime can be formed. These films are formed and broken continuously leading to high wear rates, although friction may be low. An example of this is extreme pressure lubrication;
- There may be a galvanic coupling between the film and the substrate leading to high rates of wear; or

- The corrosion and wear processes can act independently, both causing material loss by its own mechanism.

Corrosive wear is often characterised by a reduction in friction coefficient (Stachowiak & Batchelor, 2005: 553).

*Abrasive wear o*ccurs whenever a material is loaded to or slid over a harder material or a material of equal hardness. *Abrasive wear* in metals usually happens by one of three mechanisms: micro cutting, micro fracture or ploughing. Asperities of the harder material can cut the softer material, removing shavings or chips from the surface similar to the process of machining. Sliding of the harder asperities can also cause grooves in the softer material although no material is removed from the surface. This is called ploughing and is characterised by material being displaced to the sides of the grooves. When the softer material is brittle, *fracture* of the material can occur, although this is a problem encountered more with ceramics. Metals are generally quite ductile and wear may rather occur as a result of repeated loading and deformation. This is called *fatigue wear*. Very often, wear debris become trapped between the two moving surfaces as a result of other wear mechanisms such as *adhesion*. These particles are usually work-hardened and could cause extensive damage. This is called *three-body abrasive wear* (Stachowiak & Batchelor, 2005: 483 - 488).

In well-lubricated contacts *adhesion* may be negligible. Yet high wear rates could persist as a result of *fatigue wear*. It was mentioned earlier that elastic and plastic deformation initiates a few millimetres below the surface and then propagates upwards. During this process the material orientates itself parallel to the surface in a similar manner than a solid boundary lubricant would. The formation of surface and subsurface cracks can lead to the formation of wear particles. *Surface crack initiated fatigue wear* usually occurs as a result of unlubricated reciprocating sliding when a high degree of reorientation of the material is experienced. The formation of surface cracks at weak spots in the material can lead to wear particles if conditions are harsh enough for the crack to grow. *Surface crack initiated fatigue wear* is highly dependent on the presence of oxygen. Oxidation of the material inside the crack prohibits re-adhesion or “crack healing”, which increases the rate of wear. *Subsurface crack initiated fatigue wear* occurs as a result of elastic and plastic deformation below the surface. Inclusions and

other imperfections inside the material cause the formation of voids, which initiates crack growth parallel to the surface. At some time this crack propagates upwards and a wear particle breaks loose. This idea forms the basis of the *delamination theory of wear. Fatigue* is generally an important wear mechanism at moderate friction coefficients. At high friction wear is dominated by adhesion, while at low friction the subsurface forces may not strong enough to initiate and sustain crack growth (Stachowiak & Batchelor, 2005: 571 - 578).

Other forms of wear include *erosive wear*, *cavitation wear*, *fretting wear*, *impact wear*, *melting wear* and *diffusive wear*. These are considered to be negligible to the mechanisms discussed above for the application under study here.

All diesel lubricity tests, discussed in the next section, are concerned with the rate of wear. Their “lubricity values” are usually a form of time-dependent wear scar measurement or a load carrying capacity. The modelling of wear is an almost impossible task, but Fox (2005) published some work on the correlation of measured wear scar diameters (*MWSD*) on a high frequency reciprocating rig (HFRR) with additive concentration.

## 5.2. A model for diesel fuel additive lubricity (Fox, 2005)

Fox (2005) used an HFRR to obtain the MWSD’s of diesel samples with different polar additives at a range of concentrations. He found that for all the additives tested a plot of MSWD vs. additive concentration resembled a reverse sigmoidal shape, as indicated by **Figure 14**.

The model proposes that the lubricity additive dissolved in diesel will equilibrate with adsorbed additive molecules on the metal surfaces of the specimens used on the HFRR. These additives may adsorb chemically (specifically) or physically (non-specifically). At very low concentrations the surface is only partially covered by an adsorbed film. This film is not strong enough to resist the combined forces of load and shear due to its incoherent and disordered state and high wear is observed. The wear

scar diameter at very low additive concentrations is usually independent of the type of additive.

At some critical concentration 'I/II' a rapid decrease in wear is observed. The concentration value for an additive to become effective will be dependent on the enthalpy of interaction between an additive molecule and a surface site. The extent of the wear reduction will be a function of the enthalpy of adsorption of additive molecules on the surface. The concentration range over which the reduction in wear takes place concerns the entropy between the additive molecules, which infers their ability to form a well ordered film capable of reducing wear. The reduction in wear continues up to a concentration 'II/III'.

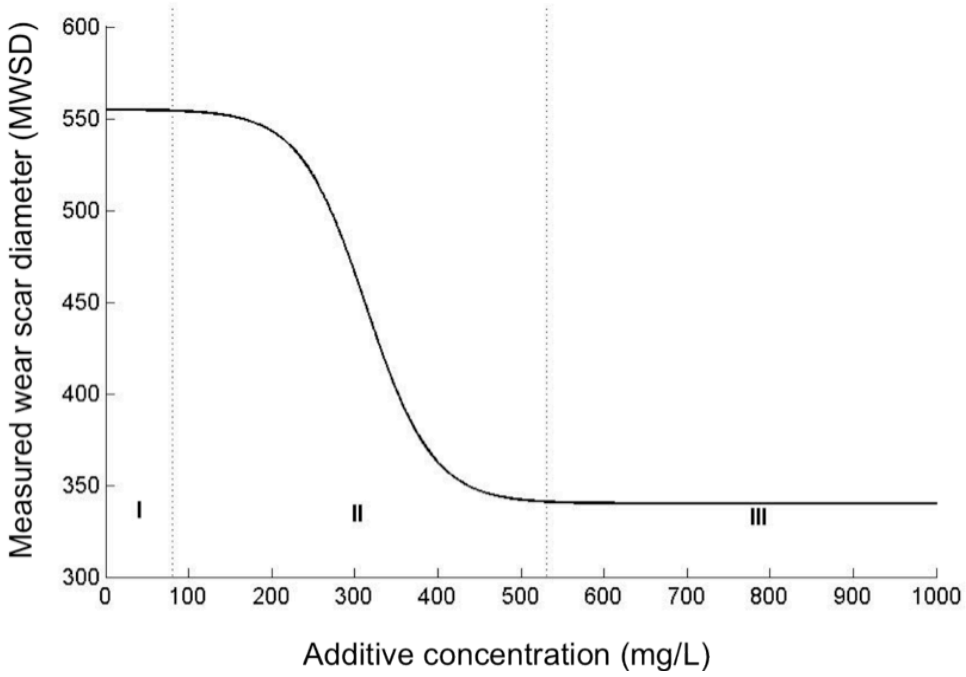


***Figure 14**. Idealised reverse sigmoidal curve for correlating additive concentration to wear (Fox, 2005).*

No further reduction in wear scar diameter is observed at a concentration higher than 'II/III' due to the fact that the surfaces are fully covered by film. There is a possibility that a multilayer of additive may form, but neither the friction nor the wear will be highly affected by the formation of a multilayer.

Wear scar vs. concentration data obtained for esters by Anastopoulos *et al.* (2005), Anastopoulos *et al.* (2002) and Anastopoulos *et al.* (2001) and for diesel blends by Barbour, Rickeard and Elliott (2000) substantiate Fox's proposed model as shown by their results shown in **Figure 15**.

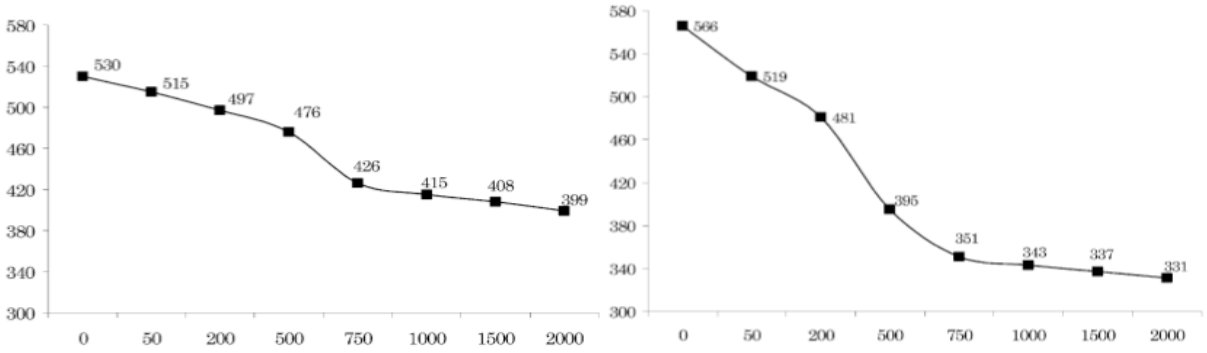


***Figure 15**. Wear scar diameter (micron) vs. concentration (mg/l) results obtained for esters by Anastopoulos et al. (2001).*

As seen in **Figure 15** the curves in section 'I' and 'III' are not exactly flat as illustrated in the idealised curve of **Figure 14**.

## 6. A boundary lubrication approach (Chang, 2006)

According to Chang (2006), four interrelated processes govern any lubrication process:

- A mechanical process that determines the stress, mode of deformation and true area of contact;
- A micro-contact thermal process that determines the asperity temperatures;
- A physio-chemical process of boundary films; and
- A stochastic process of random micro-contacts.

These four processes are coupled and cannot be removed from each other. The approach by Chang (2006) brings these four processes together with the use of *7* variables and *7* equations. The approach is discussed below.

Any lubrication process involves two rubbing surfaces each with a certain surface roughness. The first step in his approach was defining the two rubbing surfaces as statistical asperities. The asperities were assumed to be spherical tipped with a certain statistical height distribution, as described by Greenwood and Williamson (1966).

The second step was defining event-averaged micro-contact variables for each asperity pair in contact. These were defined for each collision pair as the severity of the processes generally differed between asperity pairs. System-level variables could be obtained by statistically integrating each of these micro-contact variables. Seven micro-contact variables were defined as the following:

$A_m$ Area of micro-contact (mechanical variable);

$P_m$ Asperity contact pressure (mechanical variable);

$\tau_m$ Asperity shear stress (mechanical variable);

$T_m$ Asperity temperature (thermal variable);

$S_a$ Probability that the surface is covered by an adsorbed film ($S_a < 1$);

$S_r$ Probability that the surface is covered by a chemical reaction film ($S_r < 1$);

$S_n$ Probability of a contact with no boundary protection ($S_n < 1$).

The seven equations suggested by Chang (2006) are shown below as (2.23) to (2.29).

$$S_a + S_r + S_n = 1 \tag{2.23}$$

$$P_m = f\left(\delta_m, \mu_m\right) \tag{2.24}$$

$$A_m = f\left(\delta_m, \mu_m\right) \tag{2.25}$$

where $\mu_m$ is friction coefficient and $\delta_m$ is relative normal approach.

One may ask how pressure can be a function of friction coefficient, which is asperity shear stress divided by asperity pressure? This is to include the difference in pressure as a function of mode of deformation (elastic vs. plastic), which will definitely affect the pressure and the contact area.

$$\tau_m = S_a\tau_a + S_r\tau_r + S_n\tau_n \tag{2.26}$$

where $\tau_a = f(T_m, P_m)$ is the shear strength of an adsorbed film;

$\tau_r = f(T_m, P_m)$ is the shear strength of a chemically reacted film; and

$\tau_n$ is the shear strength of the weaker surface in the sliding contact.

$$S_a = f(T_m, P_m) \tag{2.27}$$

$$S_r = f(T_m, P_m, \tau_m) \tag{2.28}$$

$$T_m = T_{bulk} + \Delta T_m \tag{2.29}$$

where

$T_{bulk}$ is the temperature of the bulk fluid in close proximity to the contacting surfaces.

$\Delta T_m = f(P_m, A_m, \tau_m, v)$ where $v$ is relative sliding velocity of the surfaces.

The solution to these seven equations could be statistically integrated to yield the system variables as a function of time.

This is a very short summary of Chang's (2006) boundary lubrication modelling approach. The approach itself seems quite understandable, but closer investigation of each of these suggested functions uncovers the reasons why a fundamentally correct boundary lubrication model does not exist.

# 7. Overview of experimental options

## 7.1. Diesel lubricity test methods

Investigations in the field of diesel lubricity have achieved fresh prominence since the problems with low sulphur diesel in Sweden during the 1990's. The level of crude oil hydrodesulphurization was found to have a detrimental effect on engine lifetime. As a

result of this, lubricity additives had to be added to the fuel. Lubricity specifications became a diesel property that needs regulation (Oláh, Szirmai & Resofszki, 2005).

The best method to quantify fuel lubricity is by use of fuel injection equipment (injectors or rotary and distributor type pumps). This is however time-consuming and impractical for daily use. Test methods that distinguish between poor and acceptable fuel lubricity levels in relatively short times are a necessity, especially for refineries.

A great variety of lubricity test methods exist, but most of them were designed primarily for testing lubricating oils (Margaroni, 1998). These tests are too severe and insensitive for diesel testing. Some of the most popular test equipment used for diesel lubricity testing is mentioned below. Each of these rigs has a characteristic "lubricity value", which is an indication of the wear rate of the fuel sample.

- High frequency Reciprocating Rig (HFRR);
- Scuffing Load Ball on Cylinder Evaluator (SL-BOCLE);
- Ball on Cylinder Evaluator (BOCLE);
- OPTIMOL Oscillating, friction, wear Test Machine (SRV "*Schwingung Reibung Verschleiss*");
- Ball-on-three-disks (BOTD) method; and
- High Temperature Oscillating Machine (HiTOM).

Of all the test rigs mentioned above, only the HFRR was designed for low sulphur diesel testing. The rig was designed under the supervision of Prof. H.A. Spikes at Imperial College, and has been the prescribed diesel lubricity test rig since 1997 (Nikanjam, 1999) (ASTM D6079, 2005) (ISO 12156, 2003) (Fox, 2005).

The other popular diesel lubricity test method is the SL-BOCLE, although it wasn't designed with diesel testing in mind.

Results obtained for different diesel-additive combinations by use of these test rigs are extensively covered in literature. Most of these papers have a very pragmatic approach and usually focus on one or both of the following:

- Comparison of the "lubricity values" obtained with different test rigs at different sliding conditions (Blizard & Bennett, 1996) (Lacey, *et al.*, 2001); and
- Determination and comparison of the ability of oxygen-, nitrogen-, aromatic- and sulphur-based additives to improve the lubricity of a base fuel (Wei & Spikes,

1986) (Knothe & Steidley, 2005) (Anastopoulos, *et al.*, 2005) (Matzke, *et al.*, 2009).

Macroscopic lubricity testing provides limited insight into the underlying principles. Tribology is a molecular phenomenon and therefore studying surfaces at molecular level is a crucial component of understanding macroscopic results.

## 7.2. The analysis of boundary films in-situ

The analysis of boundary films is a problem as old as the science itself and is, without a doubt, one of the reasons that boundary lubrication is still not understood well after about a century of research. One of the reasons for this is that it is rarely possible to carry out both friction and adsorption studies on identical surfaces. On surfaces where it is possible to study adsorption, e.g. glass and mica, friction behaviour changes dramatically and the researcher is limited to low contact pressures. When “engineering surfaces” like metals are used to study friction, one loses the ability to study adsorption, due to the fact that most adsorption analysis techniques use optical methods (Spikes, 1993) (Tabor, 1981).

Use of vacuum-based surface analytical techniques, like the scanning electron microscope (SEM), are also prohibited, because volatile components will evaporate and deposit on windows and other sensitive parts of the vacuum chamber. Furthermore supernatant solvent or base oil will obscure the film (Spikes, 1993). SEM can therefore only be used to analyse the damage on cleaned surfaces upon the completion of a friction test.

According to Spikes (2004) two of the most popular methods for studying boundary films in-situ are:

- Optical interferometry;
- Scanning microscopy techniques (Lateral force microscopy); and
- Surface force apparatus (SFA).

In any tribological contact load is being carried by both the boundary film and the metal or oxide, as indicated by **Figure 4**. The frictional behaviour of the lubricant film alone is difficult to isolate in a macroscopic friction test. With LFM and SFA a

microscopic friction test can be carried out and the effect of the lubricant can be isolated. These methods do however have some limitations. The films associated with diesel lubricity are no more than *2 nm* thick. In order to effectively isolate the frictional behaviour of the lubricant film, the surface roughness of the material should be lower than the film thickness. Such a low surface roughness is difficult to obtain with a metal surface. The other limitation is that the sliding speed of an LFM tip is in the order of micrometres per second and therefore no liquid is entrained into the contact (Glovnea *et al*., 2003). At present the only method capable of measuring *nm* thickness films in realistic contacts are based on optical interferometry.

The *ultra-thin film interferometer* is really an EHL test rig, which gives film thicknesses as a function of entrainment speed for engineering contacts at high shear rate and pressure. At very low entrainment speeds the boundary lubricating properties of a sample becomes very evident as the film thickness becomes almost independent of entrainment speed. Currently film thicknesses of as low as *0,3 nm* can be measured (Glovnea *et al.*, 2003).

## 7.3. Analysis of tribological surfaces

Two methods to analyse tribological surfaces after the completion of a friction test are X-ray photoelectron spectroscopy (XPS) and infrared reflection absorption spectrometry with grazing-angle FTIR (Spikes, 2004) (Rashmi, Sahoo & Biswas, 2009). Rashmi *et al.* (2009) have used both these methods to indicate the presence of metallic soaps on metal surfaces formed during a friction test.

One can also use other measurements to infer what is happening on the surface without physically examining the surface itself. One such measurement is electrical contact resistance.

## 7.4. Measurement of Electrical Contact Resistance (ECR)

The measurement of electrical contact resistance of the sliding contact is one of the oldest methods used for establishing film presence. This measurement was included in

the HFRR. When metal-to-metal contact is established between the top and bottom specimens the electrical resistance is zero, seeing that clean metals are very conductive. Surface interactions like chemical reaction, physical adsorption and chemisorption separate the two surfaces, acting like a resistor. A hydrodynamic film will essentially yield an infinite contact resistance, provided the film is non-conductive.

According to Stachowiak and Batchelor (2005: 319) the contact resistance increases in quite a complex manner as the film thickness increases and one should therefore be very careful. Many phenomena, such as the conductivity of the film itself, can affect this measurement and it should only be used to give an idea of the lubricant film build-up and breakdown.

In the HFRR a circuit voltage of *15 mV* is applied over the specimen contact and a balance resistor in series as indicated by **Figure 16**. These two resistors form a *potential divider circuit*. Equations (2.30) and (2.31) are used to calculate the percentage film.

$$V_{in} = I\left(R_1 + R_2\right) \qquad V_{out} = IR_2 \tag{2.30}$$

$$\%Film = 100 \times \frac{V_{out}}{V_{in}} = 100 \times \frac{R_{balance}}{R_{balance} + R_{contact}} \tag{2.31}$$

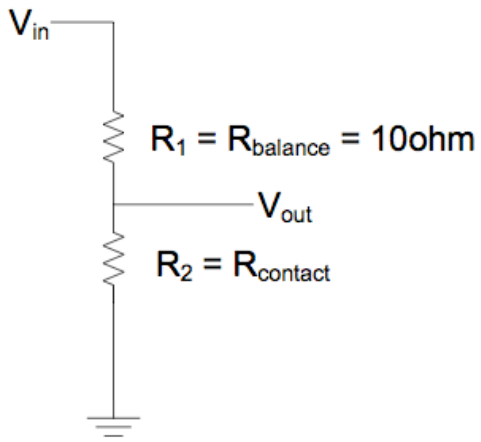


***Figure 16**. The circuit used for measuring the electrical contact resistance in the HFRR.*

According to PCS Instruments (2005) a balance resistor of *10 Ω* gives satisfactory results when testing diesel fuels.

Onion and Suppeah (1984) did some work on the measurement of contact resistances of diesel fuels, indicating that boundary films are products of dynamic operation. They also found that these films have very similar relations between resistance and load for static and dynamic conditions. These films also remained quite strong when diesel was replaced with a fluid with no lubricating properties or with no fluid at all.

The presence of an applied voltage may have some effects on the type of film formed in the contact, but according to Onion and Suppeah (1984) this effect was very small. They found that self-generated emf's of up to *3,5 mV* were detected in contacts with no applied voltage.

# Chapter III

# EXPERIMENTAL WORK

Experimental work was done to explore the underlying principles of how boundary films are adsorbed, reacted and desorbed as an effect of the surface temperature, pressure and shear. The work utilised the HFRR for all the friction tests conducted.

*"…the processes involved in boundary lubrication are very localized, hidden within the impenetrable walls of a contact, far away from the gaze of the curious scientist", H.A. Spikes (1993)*

---

## 1. Apparatus

### 1.1. The High Frequency Reciprocating Rig (HFRR)

The HFRR, supplied by PCS Instruments, uses an electromagnetic vibrator to oscillate a loaded top specimen (ball) on a fixed bottom specimen (disk), which is held in a small bath. An electrical heater controls the temperature of the test lubricant (fuel) in the bath. The friction force transmitted between the specimens and the electrical contact resistance (ECR) is measured. Measurement of the wear scar on the top specimen is used to quantify the lubrication of the sample. A schematic diagram of the HFRR is shown in ***Figure 17***.

The HFRR has been included in the European diesel standard EN 590 (2008), which utilizes the ISO12156-1 (2003) method and also in the American diesel standard ASTM D975 (2009) which utilizes the ASTM D6079 (2005) method. **Table 2** summarises the ISO 12156 test method.

The HFRR was supplied without an environmental chamber, meaning that laboratory humidity and temperature were not controlled. The *WS 1.4* correction in ISO 12156-1 (2003) takes this into account (the wear scar diameter corrected to a standardized water vapour pressure of *1,4 kPa*). ASTM D6079 (2005) specifies that as long as the

laboratory humidity is above *30%* the *Mean Wear Scar Diameter* (*MWSD*) will be sufficient and no correction is required. ISO 12156-1 (2003) gives a chart of acceptable laboratory conditions. Test results will only be valid when the laboratory conditions are acceptable.

***Table 2**. Summary of the ISO 12156-1 (2003) method.*

| Property | ISO 12156 |
|---|---|
| Stroke | *1 ± 0.02 mm* |
| Test temperature | *60 ± 2 °C* |
| Applied normal load | *200 ± 1 g* |
| Frequency of oscillation | *50 ± 1 Hz* |
| Fluid volume | *2 ± 2 ml* |
| Relative humidity | Refer to chart in ISO 12156-1 (2003). |
| Test duration | *75 ± 0,1 min* |
| Bath surface area | *6 ± 1 $cm^2$* |
| Test ball (top specimen) | |
| Material | Grade 28 (ANSI B3.12) of AISI E-52100 steel |
| Hardness | Rockwell hardness “C” Scale number *58-66* |
| Surface finish ($R_a$) | *$R_a$ < 0,05 µm* |
| Diameter | *6 mm* |
| Test disk (bottom specimen) | |
| Material | AISI E-52100 steel |
| Hardness | Vickers hardness “*HV30*” Scale number *190-210* |
| Surface finish | Turned, lapped and polished to *$R_a$ < 0,02 µm* |
| Diameter | *10 mm* |
| Repeatability at 60C° | 63 *µm* |
| Reproducibility at 60°C | 102 *µm* |

The HFRR software performs the *WS1.4* correction and the equation used for the calculation is available in the standard. ISO 12156-1 (2003) specified a minimum lubricity of *WS1.4 ≤ 460 µm* and ASTM D6079 (2005) specified a *MWSD ≤ 460 µm.*

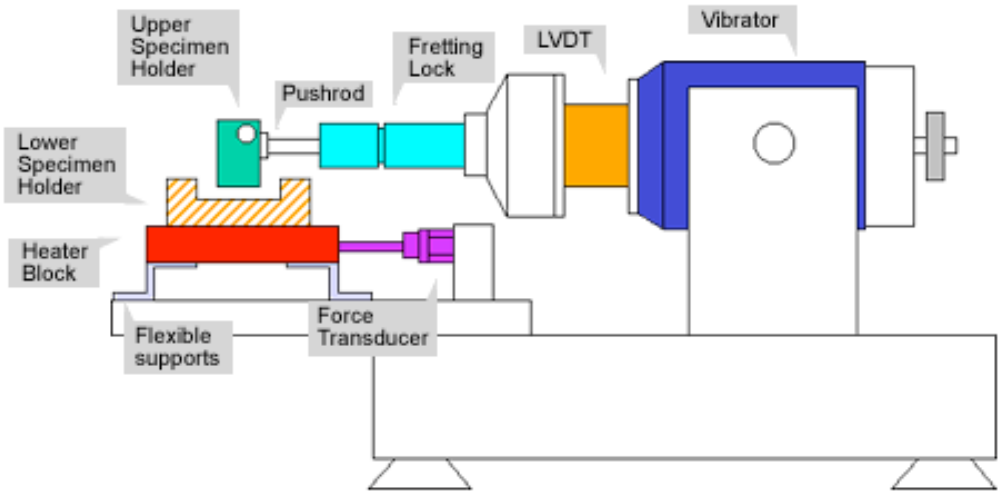


***Figure 17**. Diagram of HFRR mechanical unit (PCS Instruments, 2005).*

Very often it happens that diesel engines fail as a result of insufficient lubricity although the diesel gave sufficient HFRR results (*WS1.4 < 460 µm*) (Olah *et al.*, 2005). Wear scar diameters do not give any information about the wear mechanism at hand or the amount of damage incurred on the surfaces. The extent of surface damage does not always correlate well with the wear scar diameter.

According to Olah *et al*. (2005) there are two basic scar types:

- Wear scars where material loss leads to mechanical failure by adhesion or abrasion; and
- Wear scars where the surfaces are polished (discoloured) without any material loss or harm.

With this in mind, Olah *et al*. (2005) developed a complementary rating method to assist in the evaluation of HFRR results. The complementary rating system is a visual rating method, where the wear scar of the top specimen (ball) is compared to the pictures in **Figure 18**. Six ratings were designated to the pictures, ranging from *full lubrication* (rating of 1) to *no lubrication* (rating of 6).

This visual rating method does not form part of the ISO 12156 or the ASTM D6079 standard, but its development proves that the measurement of wear scar diameter is not enough to characterise the effectiveness of a lubricant.

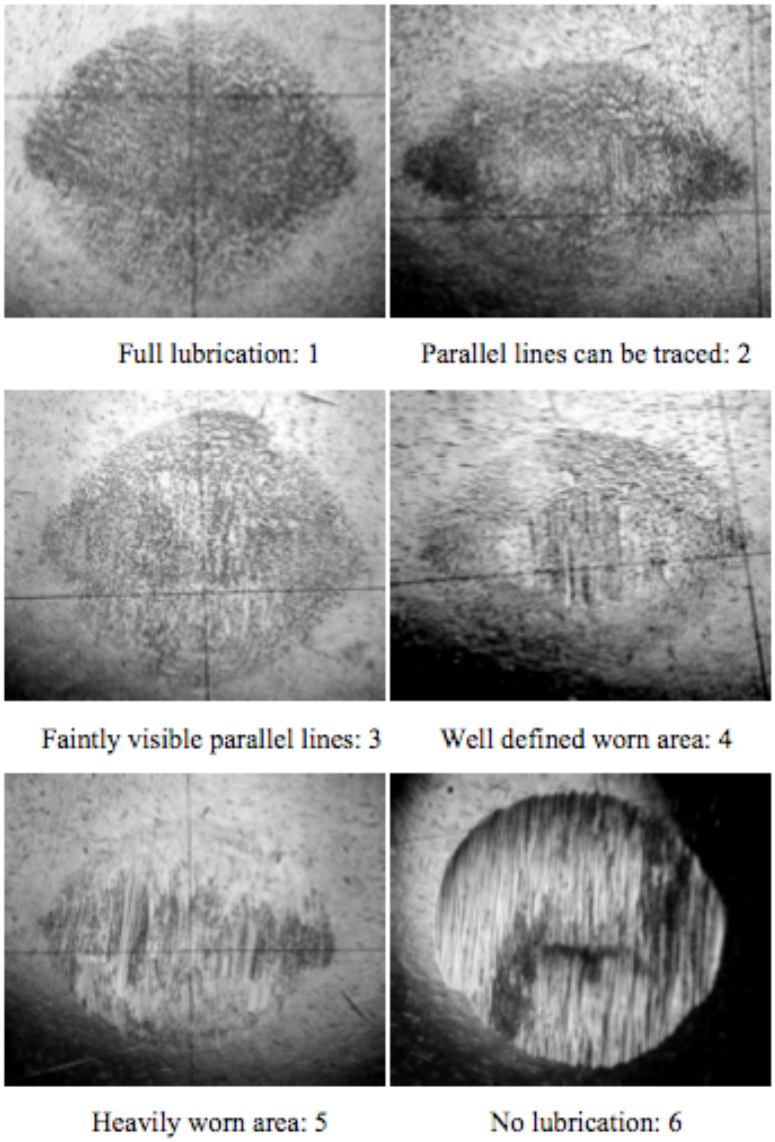


***Figure 18**. A visual rating method to assist in HFRR results evaluation (Olah et al., 2005).*

## 1.2. Fourier Transform Infrared Spectrometry

A PerkinElmer Spectrum 100 FT-IR with Spectrum Version 6.3.5 software was used for the analysis of the liquid fuel samples before and after friction tests. The horizontal attenuated total reflectance (HATR) sampling accessory was used together with a zinc selenide (ZnSe) crystal. This setup provided sufficient path length to detect the small concentrations of the additive in the base fuel.

### 1.3. Comprehensive 2-D gas chromatography with time-of-flight mass spectrometry (*GC×GC/TOF-MS*)

A LECO Pegasus® 4D *GC×GC/TOF-MS* system, at the Department of Analytical Chemistry at the University of Pretoria, was used for analysis of the diesel samples. A 7890A GC from Agilent Technologies was used together with a 7683B series autosampler (AS) also from Agilent Technologies.

### 1.4. Scanning Electron Microscope

A JEOL JSM-5800LV low vacuum electron microscope was used to investigate the wear scars obtained on both specimens after the completion of friction and wear tests.

## 2. Experimental Design and Method

The goal of this experimental investigation was to analyse the mechanisms of friction and wear for different additive concentrations at varying sliding conditions. Diesel contains in excess of *10 000* components each with its own interactions with the surface and the other components present in the sample. It would be an enormous task to understand the role of each of these compounds at different conditions of temperature, pressure and sliding velocity. For the purpose of this investigation only a binary mixture of n-hexadecane (cetane), as base fuel, and palmitic acid, as lubricity additive, is used. Hexadecane is a linear hydrocarbon widely used in fundamental lubrication research (Glovnea *et al*, 2003). Palmitic acid is a $C_{16}$-carboxylic acid with good boundary lubrication properties (Wei & Spikes, 1986). Both these chemicals were obtained from Merck and their physical and chemical properties are shown in **Table 3**. The chemicals were used without further purification, although *GC×GC/TOF-MS* analysis of the n-hexadecane received from Merck indicated the presence of $C_{16}$-branched molecules and $C_{16}$ molecules containing double bonds. The additive was not analysed for impurities.

***Table 3**. Physical and chemical properties of the chemicals used for analysis.*

| Property | n-hexadecane ($C_{16}H_{34}$) | Palmitic Acid ($C_{16}H_{32}O_2$) |
|---|---|---|
| Purity (as received from Merck) | ≥ 99% (for synthesis) | 98% (for synthesis) |
| Molecular Weight | 226,44 | 256,42 |
| Density (at STP) (g/cm$^3$) | 0,77 | 0,852 |
| Viscosity (at 25°C) (cP) | 3,032 | Solid |
| Melting Point (°C) | 18 | 61,75 |
| Boiling Point (°C) | 287 | 271,5 |

Palmitic acid was dissolved in n-hexadecane to make up *8* concentration standards that were used for testing: *50 mg* palmitic acid/liter total sample, *100 mg/l*, *250 mg/l*, *500 mg/l*, *750 mg/l*, *1000 mg/l*, *1500 mg/l* and *2000 mg/l*. Friction and wear test were performed with the HFRR on each of the standards prepared. The experimental design could be categorised into *4* sections.

## 2.1. Wear tests performed according to the ISO 12156 standard

This method involved running an HFRR test according to the ISO 12156-1 (2003) procedure. A new ball and disk was used for each of the tests. The tests were performed twice or more times if the standard deviation of the *1$^{st}$* two were larger than *30 µm*. Great care was taken to adhere to all the cleanliness requirements of the standard (ISO12156-1, 2003). Oxidation of and the physisorption of water onto the specimens before the test can have enormous effects on the results, seeing that both of these parameters influence adhesive wear which causes most of the damage in the first few seconds of the test. The cleaning procedure can be found in the standard (ISO 12156-1, 2003) but is repeated here to emphasise its importance.

The disks and balls were soaked in toluene for a minimum of *8* hours before the test. Using clean forceps, the specimens, screws and everything that came into contact with the test fluid was transferred into a glass beaker with toluene and ultrasonically stirred for *10 min*. All the hardware and specimens were transferred to a beaker filled with acetone and ultrasonically stirred for *5 min*. The specimens were blow-dried and the test

started immediately. Upon completion of the test, the test ball was rinsed several times in toluene and acetone, ultrasonically stirred in toluene for *30 s* and finally in acetone for a further *30 s*. The ball was allowed to air dry and the wear scars were measured under the microscope. Neither the specimens nor the screws were ever touched. The wear scar diameters were measured and corrected to the *WS1.4* value.

It is a well-known fact that addition of additives beyond a certain critical concentration will not be beneficial in wear reduction (Fox, 2005) (Anastopoulos *et al.*, 2002) (Anastopoulos *et al.*, 2001). The goal of this test procedure was to find that critical palmitic acid concentration for effective wear reduction and also to compare the experimental results to the model proposed by Fox (2005).

## 2.2. Diesel analysis by *FTIR* and *GC×GC/TOF-MS*

As discussed in the *Chapter II* the experimental options to study boundary films in-situ are very limited. For this reason *FTIR* and *GC×GC/TOF-MS* were used to study the liquid fuel samples before and after a friction and wear test. According to Rashmi *et al.* (2009) metallic soaps could be detected on sliding surfaces. A difference in composition of the liquid fuel samples before and after the HFRR test will correspond to the amount of palmitic acid bonded to the metal surface. *FTIR* and *GC×GC/TOF-MS* were used to detect the difference.

According to Kajdas, Makowska and Gradkowski (2006) n-hexadecane suffered some oxidation to carboxylic acids and other oxygenates during a friction test on a non-oscillatory ball-on-disk test rig (Load = *9,81 N*, sliding speed = *0,25 m/s*, sliding distance = *500 m* and ambient conditions). Although these test conditions are more severe than the conditions prescribed by ISO 12156 and ASTM D6079, oxidation could possibly affect an HFRR test.

Another mechanism that could be responsible for changes in the test fluid composition is the catalytic decomposition of organic compounds by metals, already discussed in *Chapter II*.

*FTIR* and *GC×GC/TOF-MS* were used to identify these two mechanisms.

## 2.3. Analysis of friction and wear mechanisms with the *HFRR* and *SEM*

There are several wear mechanisms that can play a role in the HFRR tribo-contact, as discussed earlier in *Chapter II*. Analysis of the wear scar after the completion of a test, as suggested by Olah *et al*. (2005), is indeed helpful, but a dynamic wear reading is essential in understanding what wear mechanisms play a role and at what stage in the sliding experiment. The HFRR doesn't have dynamic wear measurement capabilities so tests had to be performed and stopped at regular intervals to analyse the wear scar on the top specimen.

The tests were performed for dry sliding conditions and *250 mg/l* palmitic acid at the conditions set out by ISO 12156-1 (2003) and stopped at *1 min*, *2 min*, *3 min*, *6 min*, *10 min*, *20 min*, *30 min*, *40 min* and *75 min*. The wear scar diameters were measured at each of these time intervals and photos of the wear scars were also taken. The test balls weren't cleaned for the photo at each time interval and the same liquid was left in the sample holder. To investigate the effect of stop-starting the test continuously, a test was performed without stopping for *75 min*. The wear scar diameters and damage incurred on the surfaces were compared for the two sets of tests.

The friction results from the tests performed according to ISO 12156 at different palmitic acid concentrations were also analysed.

The SEM was also used to identify wear mechanisms by analysis of the surface after the completion of HFRR tests.

## 2.4. The effect of changed sliding conditions on friction and wear

Briscoe and Evans (1982) and Subhalakshmi *et al.* (2008) have used the *Eyring Equation* with limited success, due to the fact that $V_o$, $Q'$, $\phi$ and $\Omega$ are not constants as assumed by them. Experimental results obtained by Subhalakshmi *et al.* (2008) indicated that $V_o$, $Q'$, $\phi$ and $\Omega$ should be functions of $T$ or $p$ or $v$ or any two of them or all three of them. By performing similar tests than these authors but at more combinations of pressure, temperature and sliding velocity functions that express $V_o$, $Q'$, $\phi$ and $\Omega$ could possibly be derived.

Friction and wear behaviour in the HFRR for palmitic acid was studied at different combinations of load, frequency and temperature at a palmitic acid concentration of *2000 mg/l* to ensure that a well-established film is formed. The following values were used:

- Frequency: *20 Hz*, *50 Hz* and *70 Hz*;
- Temperature: *30°C*, *60°C* and *90°C*; and
- Load: *200 g*, *300 g* and *400 g*.

To cover all the combinations of load, temperature and frequency *27* HFRR tests had to be performed. Shear stress-pressure, shear stress-temperature and shear stress-velocity relations could be obtained and compared with equations (2.11), (2.12) and (2.13) obtained by Briscoe and Evans (1982). No repeated tests were performed.

# Chapter IV

# CONTACT TEMPERATURE MODELLING

This chapter was focussed on the modelling of contact temperatures generated with the HFRR as the first step in developing a full boundary lubrication model utilising the approach by Chang (2006). The statistical approach of Greenwood and Williamson (1966) for describing surface asperities were not used here, therefore the temperature model assumed a single contact between sliding surfaces.

This chapter discusses the equations used in formulating the temperature model and some of the results at different sliding conditions. The implications of the calculated temperatures are discussed more thoroughly in Chapter V.

---

## 1. Modelling temperature in a sliding contact

The asperity temperature ($T_m$) consists of two components: the bulk temperature ($T_b$) and flash temperature ($\Delta T_m$), as indicated by Equation (4.1) and (2.29) (Chang, 2006).

$$T_m = T_b + \Delta T_m \tag{4.1}$$

The bulk temperature is governed by the heat generation and heat transfer characteristics of the system, while the flash temperature is governed by the micro-contact properties. According to Chang (2006) the flash temperature is a function of contact/lubricant conditions and micro-contact material properties. Equation (4.2) shows that it is a function of asperity pressure, shear stress, area and surface sliding velocity.

$$\Delta T_m = f\left(p_m, \tau_m, A_m, v\right) \tag{4.2}$$

Greenwood and Williamson (1966) assumed contact between spherically tipped asperities and a flat surface and used Hertzian theory to calculate the size of the various contact spots. For the sake of simplification the top specimen of the HFRR was

assumed to be cylindrical with a radius equal to the Hertzian contact radius of a ball-on-disk configuration, moving over a stationary semi-infinite solid as indicated by **Figure 19**.

A semi-infinite solid, by definition, is an idealized body that has a single plane surface and extends to infinity in all directions. This assumption is usually made when the heat transfer problem only involves a small region near the surface and the core temperature of the body remains unchanged. Most bodies can be modelled as semi-infinite for short periods of time, seeing that heat doesn't have sufficient time to penetrate the body (Çengel, 2006: 241) (Wen & Khonsari, 2007).

According to Bhushan (2002: 294) the heat flux ($W/m^2$) as a result of friction is as shown in Equation (4.3).

$$\dot{q}_s = \mu p_m |v| \tag{4.3}$$

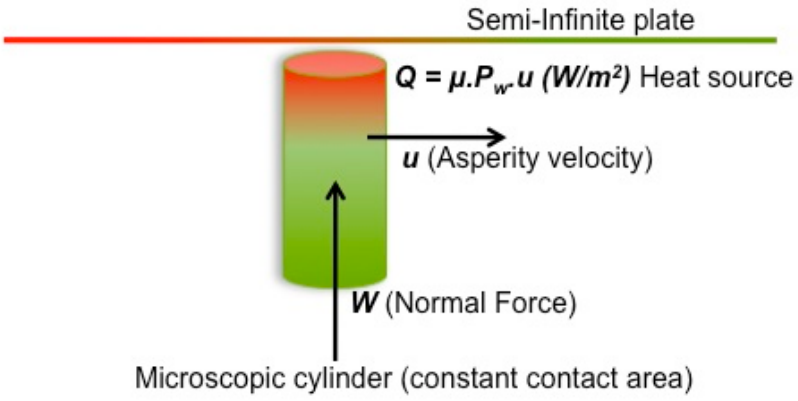


***Figure 19**. The system used for modelling asperity and plate temperature distribution.*

In a pin-on-disk unidirectional motion the heat flow equations of the disk control the temperature distribution of the interface, as discussed in *Chapter II*. When this motion becomes oscillatory, like for the HFRR, there is heat partition between the pin and the disk, which is a function of the frequency of oscillation. In this investigation only the disk temperature is calculated and adapted as heat partitions.

## 1.1. Transient semi-infinite disk temperature

The unsteady-state three-dimensional equation for heat conduction in solids or static liquids is shown as equation (4.4) (Perry & Green, 1997:5-9).

$$C_p\rho\frac{\partial T}{\partial t}=\frac{\partial}{\partial x}\left(k\frac{\partial T}{\partial x}\right)+\frac{\partial}{\partial y}\left(k\frac{\partial T}{\partial y}\right)+\frac{\partial}{\partial z}\left(k\frac{\partial T}{\partial z}\right)+q' \qquad (4.4)$$

where *q'* is the rate of heat generation by chemical reaction per unit of volume. This differential equation is satisfied by the solution in equation (4.5), if the following assumptions are made (Carlslaw & Jaeger, 1959: 256):

- Constant physical properties; and
- No heat generated by chemical reactions on the surface.

$$T\left(x,y,z,t|x',y',z'\right)=\frac{q\left(x',y',z',t'\right)}{4\rho C_p\left(\pi\kappa\right)^{3/2}\left(t-t'\right)^{3/2}}\exp\left(-\frac{\left(x-x'\right)^2+\left(y-y'\right)^2+\left(z-z'\right)^2}{4\kappa\left(t-t'\right)}\right) \qquad (4.5)$$

The point *(x',y',z')* is an instantaneous point source of heat with magnitude *q (J)*, liberated at $t = t'$. As *t* approaches *t'*, the expression tends to zero at all points except at *(x',y',z')* where it becomes infinite (Carslaw & Jaeger, 1959: 256).

Equation (4.5) must be integrated with regard to *t'* to yield a continuous point heat source. To obtain the solution for a circular continuous heat source, equation (4.5) should be integrated with respect to *x'*, *y'* and *t'*. **Figure 20** shows the modelling variables used by Wen and Khonsari (2007).

A local coordinate system $\eta O'\xi$ is displaced over a distance *s(t)* from the original position $(x_o,y_o,z_o)$. The coordinates *(x',y',z')* in (4.5) can be expressed by (4.6), (4.7) and (4.8) when it is assumed that the movement only takes place in the *x*-direction.

$$x'\left(\xi,t\right)=x_o+s\left(t\right)+\xi \qquad \text{where displacement} \qquad s\left(t\right)=\int_0^t v\left(\vartheta\right)d\vartheta \qquad (4.6)$$

$$y'\left(\eta\right)=y_o+\eta \qquad (4.7)$$

$$z' = z_o \tag{4.8}$$

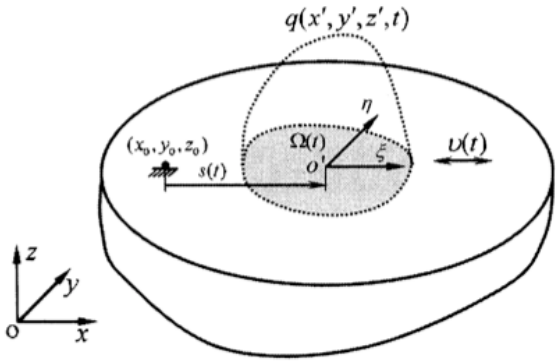


***Figure 20**. A semi-infinite body subjected to a moving heat source (Wen & Khonsari, 2007).*

The heat source could be written as shown in (4.9) (Wen & Khonsari, 2007).

$$q = q(x', y', z', t') \text{ only if } (x', y', z') \in \Omega(t) \tag{4.9}$$

Substituting (4.9) into (4.5) and integrating over the surface *Ω(t)* yields (4.10).

$$\begin{aligned} T(x,y,z,t) &= \frac{1}{4\rho C_p(\pi\kappa)^{3/2}} \int_0^t \frac{dt'}{(t-t')^{3/2}} \iint_\Omega q(x', y', z', t') \\ &\times \exp\left( - \frac{[x - x'(\xi, t-t')]^2 + [y - y'(\eta)]^2 + (z - z')^2}{4\kappa(t-t')} \right) d\xi d\eta \end{aligned} \tag{4.10}$$

Equation (4.11) is arrived at by substituting (4.6), (4.7) and (4.8) into (4.10) and represents the temperature profile generated by a moving heat source. In (4.10) $\tau = t - t'$.

$$\begin{aligned} T(x,y,z,t) &= \frac{1}{4\rho C_p(\pi\kappa)^{3/2}} \int_0^t \frac{d\tau'}{\tau^{3/2}} \iint_\Omega q(x', y', z', t-\tau) \\ &\times \exp\left( - \frac{[x - x_o - s(\tau) - \xi]^2 + [y - y_o - \eta]^2 + (z - z_o)^2}{4\kappa\tau} \right) d\xi d\eta \end{aligned} \tag{4.11}$$

The temperature profile was derived for both unidirectional and oscillating movement. **Table 4** shows some of the differences between unidirectional and oscillatory movement. Equation (4.11) was non-dimensionalised to yield the temperature profile within *Ω(t)* at any time. The non-dimensional parameters are indicated in (4.12) for unidirectional movement and (4.13) for oscillatory movement. The shape of the asperity was assumed circular so the equations are based on a circular, moving, continuous heat source with a radius, *R*.

***Table 4**. Differences in velocity, displacement and heat between unidirctional and oscillatory movement.*

| Oscillatory movement | Unidirectional movement |
|---|---|
| $v(t) = A\omega\sin(\omega t)$ | $v(t) = v$ |
| $s(t) = A\left[1-\cos(\omega t)\right]$ | $s(t) = vt$ |
| $q = q_o\lvert\sin(\omega t)\rvert$ where $q_o = \mu p_m A\omega$ | $q = q_o$ where $q_o = \mu p_m \lvert v\rvert$ |

$$\bar{X} = \frac{x-x_o}{R} \quad \bar{Y} = \frac{y-y_o}{R} \quad \bar{Z} = \frac{z-z_o}{R} \quad \Phi = \frac{vt}{R} \quad \phi = \frac{v\tau}{R} \quad \bar{r} = \frac{r}{R} \quad \bar{v} = \frac{vR}{4\kappa} \tag{4.12}$$

$$\bar{X} = \frac{x-x_o}{R} \quad \bar{Y} = \frac{y-y_o}{R} \quad \bar{Z} = \frac{z-z_o}{R} \quad \bar{A} = \frac{A}{R} \quad \Phi = \omega t \quad \phi = \omega\tau \quad \bar{r} = \frac{r}{R} \quad \bar{\omega} = \frac{\omega R^2}{4\kappa} \tag{4.13}$$

The non-dimensional equation for the temperature profile on a semi-infinite body due to a moving circular heat source is shown as equation (4.14) for unidirectional sliding and equation (4.15) for oscillatory sliding (Wen & Khonsari, 2007).

$$\frac{Tk}{2Rq_o} = \frac{\sqrt{\bar{v}}}{4\pi^{3/2}}\int_0^{\Phi}\frac{1}{\phi^{3/2}}d\phi\int_0^{2\pi}\int_0^{1}\exp\left(-\frac{\left[\bar{X}-\phi-\bar{r}\cos\theta\right]^2+\left[\bar{Y}-\bar{r}\sin\theta\right]^2+\bar{Z}^2}{\phi/\bar{v}}\right)\bar{r}d\bar{r}d\theta \tag{4.14}$$

$$\frac{Tk}{2Rq_o} = \frac{\sqrt{\bar{\omega}}}{4\pi^{3/2}} \int_0^{\Phi} \frac{\left|\sin(\Phi - \phi)\right|}{\phi^{3/2}} d\phi$$
$$\int_0^{2\pi} \int_0^1 \exp\left( - \frac{\left[\bar{X} - \bar{A} + \bar{A}\cos\phi - \bar{r}\cos\theta\right]^2 + \left[\bar{Y} - \bar{r}\sin\theta\right]^2 + \bar{Z}^2}{\phi / \bar{\omega}} \right) \bar{r} d\bar{r} d\theta \qquad (4.15)$$

where $\xi = r\cos\theta$ and $\eta = r\sin\theta$

In this work all the emphasis was placed on solving (4.15) which would give a good approximation of the contact temperature of a contact configuration such as that of the HFRR. Results for unidirectional sliding can be obtained in Tian and Kennedy (1994).

## 2. Numerical solution scheme

Solving equations (4.14) and (4.15) is quite a challenge seeing that neither equation has an analytical integrand, therefore numerical integration methods should be used. These contact temperatures are also extremely difficult to measure as discussed in *Chapter II*, so one would not be able to compare the numerical integrands with experimental values to verify the correctness of the numerical method. Furthermore, both equations (4.14) and (4.15) have singularities at $\phi = 0$, therefore when $t = t'$, increasing the degree of complexity of the numerical integration. The periodic nature of (4.15) also presented some difficulties.

To solve (4.14) and (4.15) Wen and Khonsari (2007) used a *4-point Gaussian Quadrature* over *6* subintervals for the spatial integration and a *Cautious Adaptive Romberg Extrapolation (CADRE)* for the time integration, based on extrapolation applied to *trapezoidal rule* estimates.

For the integration of (4.15) the author used the *trapezoidal rule* to integrate over $\theta$. According to Weideman (2002) application of the *trapezoidal rule* for smooth periodic functions yields very accurate results with fast convergence. The reason for this, in Lehman's terms, is that when the function is concave up (or down), the *trapezoidal rule* will overestimate (or underestimate) the true area. When integration is carried out over

one full period of the function, the error just about cancels. The code, `romberg.m`, by Heinkenschloss (2002) was used.

For the integration over $\bar{r}$ the integral was also found sufficiently smooth for the use of `romberg.m`. (Gonnet, 2010b).

The integration over $\phi$ presented the most problems due to the singularity at $\phi = 0$. Two numerical procedures were investigated:

- A vectorised adaptive quadrature, `quadva.m`, by Shampine (2008); and
- A general-purpose adaptive quadrature, `cquad.m`, by Gonnet (2010a).

It is important that the internal integrals are solved with a higher precision than the time integral. If this is not done the plots will contain discontinuities (Gonnet, 2010b).

In the *CADRE* procedure used by Wen and Khonsari (2007), the value of the integrand at the singular end point was set to zero. Both the numerical procedures mentioned above, are able to remove singularities effectively. For this reason there are small differences between the results obtained by Wen and Khonsari (2007) and those obtained by the author.

# 3. Modelling Results and Discussion

A different numerical procedure was used than Wen and Khonsari (2007) so the first section of the modelling results aims to compare results obtained by them with results obtained in this study. It also explains some of the effects of Peclet number on the results presented. In the second section the HFRR contact is modelled at the different conditions as explained in *Chapter III*.

## 3.1. Comparison of results with those of Wen and Khonsari (2007)

The results of the simulation was compared to that of Wen and Khonsari (2007) for $\bar{\omega} = 0{,}001$ and $\bar{\omega} = 1$, both at $\bar{A} = 0{,}105$. Peclet numbers for oscillating motion corresponds to $Pe = \bar{\omega}\bar{A}$.

The temperature has a certain distribution over the space, depicted by the local coordinate system *ηO'ξ*. This surface temperature distribution within the area *Ω(t)* also has a periodic nature in time, and is not necessarily in phase with the heat source, which will be shown later. **Figure 21** shows the number of cycles necessary for the dimensionless temperature to reach a steady state. One cycle corresponds to $t = 2\pi/\omega$. The maximum temperature is believed to be close to the middle of the heat source, therefore the simulation was simplified by setting $\overline{X}$ = *0*, $\overline{Y}$ = *0* and $\overline{Z}$ = *0*. There is uncertainty about the phase difference between the heat source and the dimensionless temperature, but if the temperature at $\omega t = \pi/2 + n \cdot \pi$ where *n* is an integer, gives the same value for consecutive cycles, a steady state has been reached. `quadva.m` was used for the integration over $\phi$.

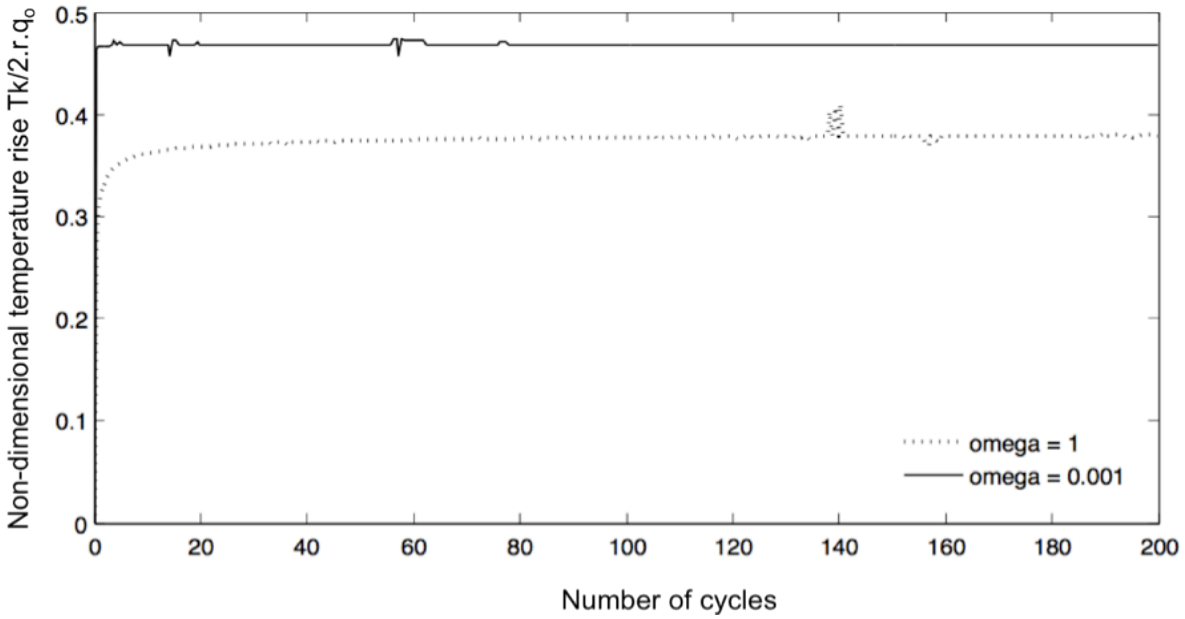


***Figure 21**. Maximum non-dimensional temperature distribution at $\overline{\omega}$ = 0,001 and $\overline{\omega}$ = 1 and $\overline{A}$ = 0,105.*

At a low oscillation frequency ($\overline{\omega}$ = *0,001*) a steady state is reached within the first oscillation. At a higher oscillation frequency ($\overline{\omega}$ = *1*) a steady state was not quite reached within the *200 cycles* plotted. According to Wen and Khonsari (2007) a steady state was only reached after about *1200 cycles*, but for all practical purposes it has reached more than *95%* of its steady value by the *20$^{th}$ cycle*.

**Figure 22** shows the non-dimensional temperature variation at steady state for *2 cycles*. For $\overline{\omega}$ = *0,001* the maximum and minimum dimensionless temperatures were *0,4932* and *0,0142* respectively and for $\overline{\omega}$ = *1* the maximum and minimum were *0,3794* and *0,2194*. A small phase shift is visible between the maximum and minimum temperatures at different frequencies. From **Figure 22** it is seen that there is a steady temperature rise in the disk, which increases as the oscillating frequency increases. The steady temperature will be the axis of oscillation. There is a periodic temperature fluctuation around this steady temperature, which corresponds to the periodic nature of the heat flux, but it is not in phase with the heat flux. According to Carslaw and Jaeger (1959: 66) the temperature lags behind the heat flux by $x\sqrt{\omega/2\kappa}$, which shows that the higher the frequency the bigger the lag will be.

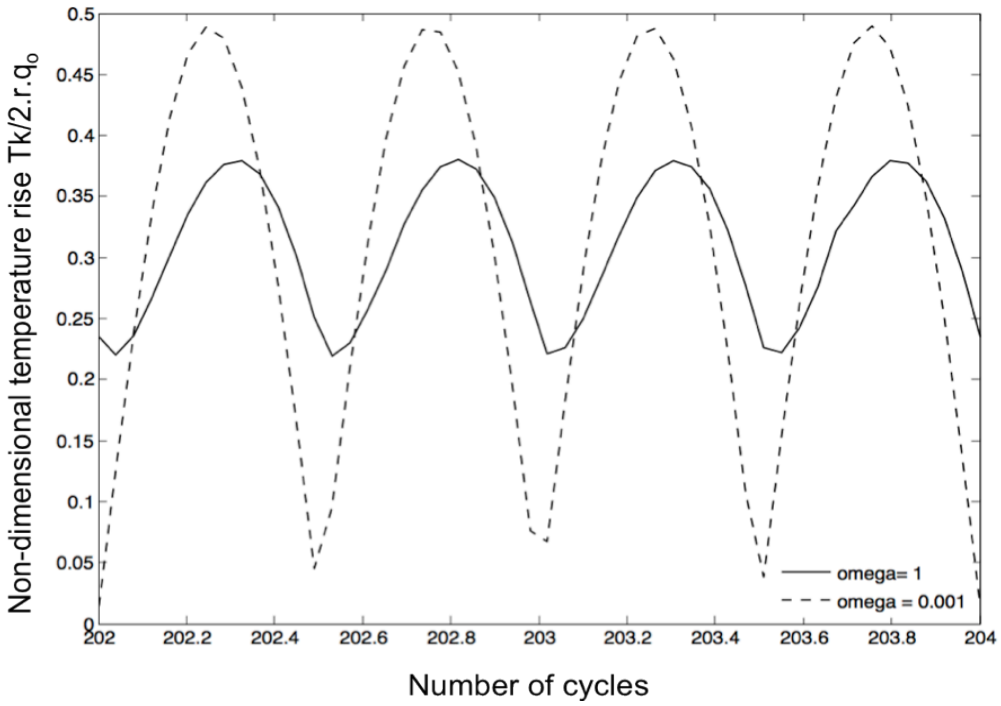


***Figure 22**. Non-dimensional temperature variation at steady state for at $\overline{\omega}$ = 0,001 and $\overline{\omega}$ = 1 at $\overline{A}$ = 0,105.*

The times at which these maximum and minimum dimensionless temperatures were found, were recorded and a simulation was performed to show the temperature distribution over the semi-infinite disk at those times for $\overline{\omega}$ = 0,001 and $\overline{\omega}$ = 1. ***Figure 23*** shows a *3-D* plot of the non-dimensional temperature distribution over the surface at

$\bar{\omega}$ = *0,001* and $\bar{A}$ = *0,105*, which indicates that the heat distribution is symmetric about the line $\eta$ = *0*.

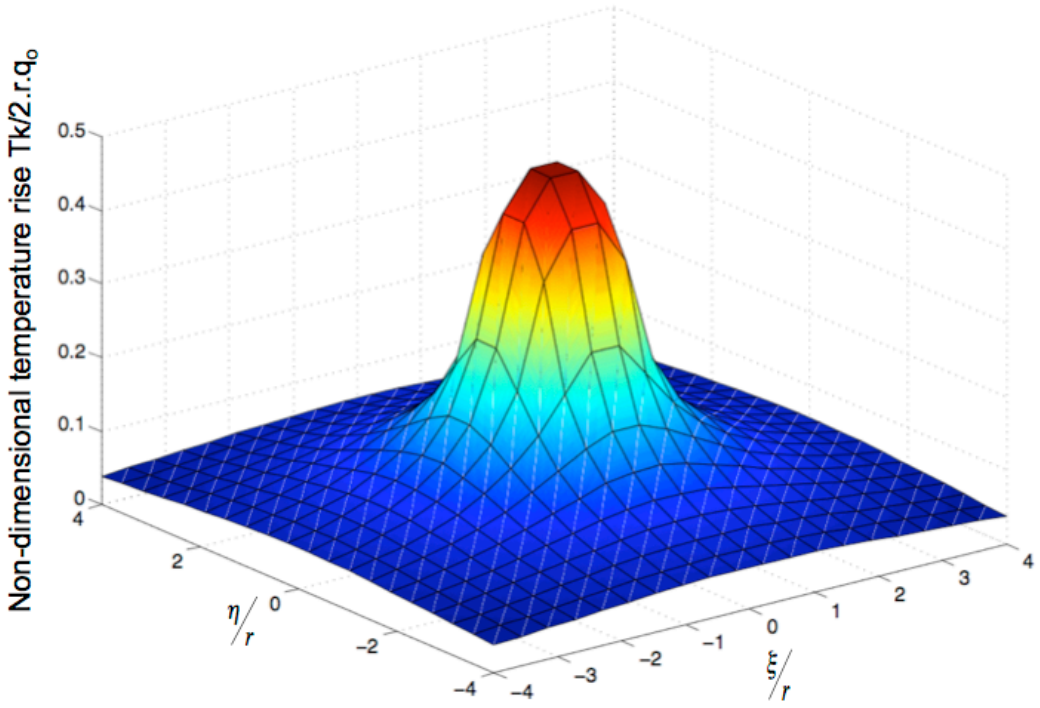


***Figure 23**. Three-dimensional plot of maximum temperature at steady state for $\bar{\omega}$ = 0,001 and $\bar{A}$ = 0,105.*

**Figure 24** shows the maximum and minimum dimensionless periodic temperature distribution at steady state for $\bar{\omega}$ = *0,001* and $\bar{\omega}$ = *1*, both at $\bar{A}$ = *0,105* and it also compares results obtained by `quadva.m` and `cquad.m` for the $\phi$-integration.

It is evident that at a lower oscillation frequency a higher maximum temperature is reached. **Figure 13** explains this beautifully. At low Peclet numbers there is enough time for heat to penetrate into the body. The additional time available for heat conduction causes a more distinct rise and fall of temperature on the surface (**Figure 22**), as the heat source delivers a flux proportional to *sin(ωt)*. At very low Peclet numbers the temperature distribution is very similar to a stationary periodic heat source.

At higher Peclet numbers heat does not penetrate deep into the body but is distributed along the sliding direction. This is also the reason that the maximum and

minimum periodic temperatures at higher $\overline{\omega}$ are closer together, as indicated by **Figure 22**.

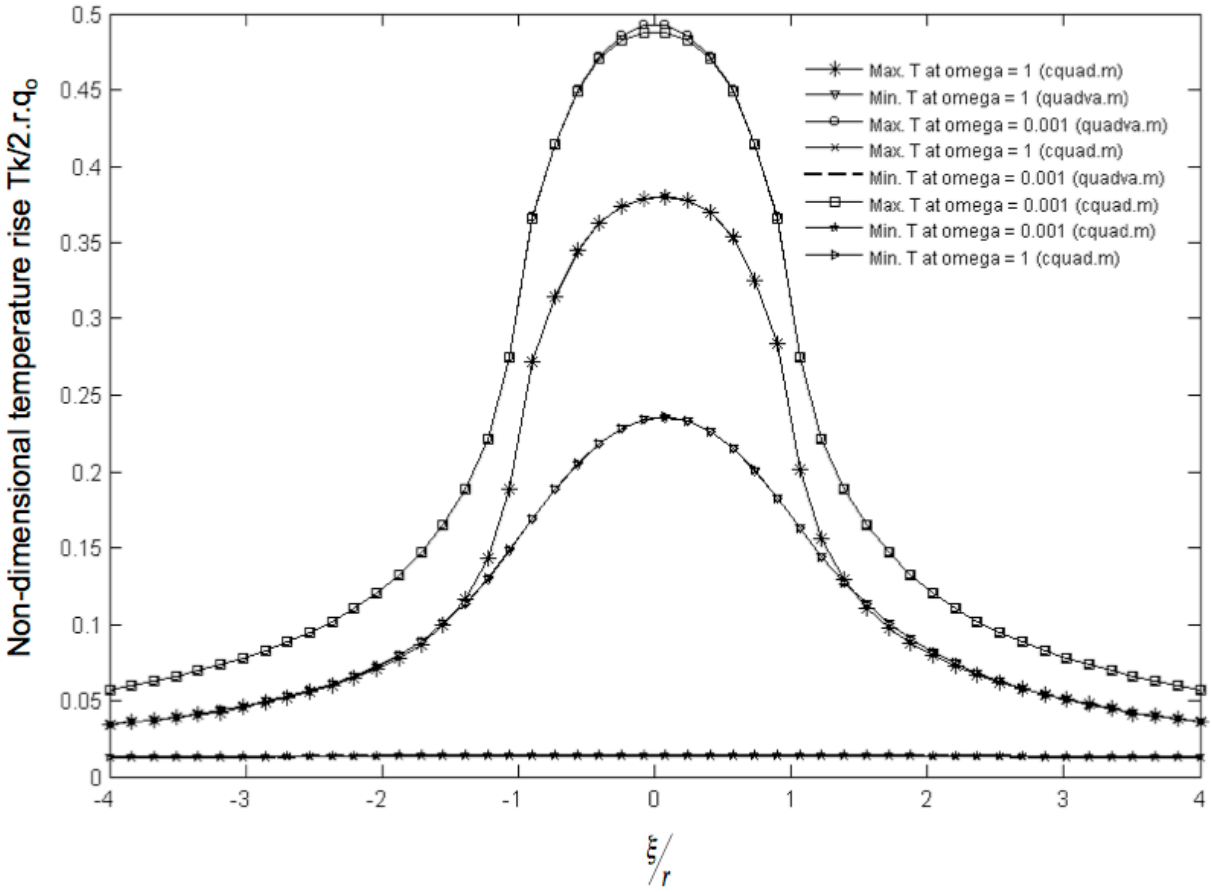


***Figure 24**. Non-dimensional periodic temperature distribution in the direction of sliding for $\overline{\omega}$ = 0.001 and $\overline{\omega}$ = 1 . Results were obtained by use of `quadva.m` and `cquad.m` for the ϕ-integration.*

The difference in results obtained between `quadva.m` and `cquad.m` for the $\phi$-integration was negligible as indicated by **Figure 24** and all the results were very similar to the results obtained by Wen and Khonsari (2007).

An investigation into the effect of dimensionless amplitude is not presented here, seeing that in the experimental procedure discussed in *Chapter III* this parameter was kept constant. According to Wen and Khonsari (2007) an increase in $\overline{A}$ will yield a lower

steady state temperature and a larger difference between the maximum and minimum temperatures at constant $\overline{\omega}$.

## 3.2. HFRR contact temperature

Knowledge of the HFRR contact temperature will enhance the researchers chances of successfully establishing and eliminating certain mechanisms in the tribological contact. The temperature model discussed above could give some approximation of the contact temperature. One should however remember that in the HFRR contact the temperature is constantly changing due to an increase in contact area as wear takes place. The formation of films and metal oxides will also have a substantial effect on the heat transfer capabilities of the surface. The validity of the assumption that the contact area is equal to the wear scar area is also uncertain.

Due to all these uncertainties it would be futile to do excessive calculations concerning the partitioning of heat for an oscillating heat source. It is assumed that all the heat is taken by the disk as discussed earlier.

The HFRR temperature was investigated as a function of oscillation frequency ($\omega$) and contact radius ($r$). A dry HFRR contact tested in accordance with the ISO 12156 conditions yielded a wear scar radius of around *650 μm*, therefore the contact radius was varied between the Hertzian contact radius and a wear scar radius for a dry test. The Hertzian contact radius was calculated as $2.76\times10^{-5}\ m$ with (4.16) below.

$$r\big|_{elastic} = \left(\frac{3Wr}{4E^*}\right)^{1/3} \tag{4.16}$$

The effect of frequency was investigated at *20 Hz*, *50 Hz* and *70 Hz*, corresponding with the frequencies investigated in *Chapter III*.

The HFRR sliding conditions were transformed into non-dimensionalised model parameters using equation (4.13), as shown in **Table 5**. The physical and thermal

properties of AISI E-52100 steel are shown in **Table 6** and were used in the simulation of the contact temperature. The number of HFRR cycles for an ISO12156 tests is *225 000* cycles. A higher Peclet number will correspond to a larger number of cycles necessary to reach a steady maximum temperature, as indicated in earlier. For the sliding conditions investigated the maximum Peclet number was obtained with an oscillating frequency of *70 Hz* and a contact radius of $6.5\times10^{-4}$ *m*. **Figure 25** shows the maximum number of cycles necessary to obtain a steady temperature. For this investigation any other set of sliding conditions will need fewer cycles to reach a steady state.

***Table 5**. Sliding conditions of the HFRR transformed into non-dimensional model parameters.*

| ISO12156 sliding conditions | Model parameter | Non-dim. Parameter |
|---|---|---|
| Oscillation frequency = *20 Hz* | $\omega = 40\pi\ s^{-1}$ | $\overline{\omega} \in [1.905\times10^{-3}, 1.507]$ |
| Oscillation frequency = *50 Hz* | $\omega = 100\pi\ s^{-1}$ | $\overline{\omega} \in [4.7634\times10^{-3}, 2.64196]$ |
| Oscillation frequency = *70 Hz* | $\omega = 140\pi\ s^{-1}$ | $\overline{\omega} \in [6.669\times10^{-3}, 3.69]$ |
| Stroke = *1mm* | $A = 0.0005m$ | $\overline{A} \in [18.1159, 0.7692]$ |

***Table 6**. Physical and thermal properties of AISI E-52100 steel.*

| **Property** | **Description** | **Value** | **Unit** |
|---|---|---|---|
| $k$ | Thermal conductivity | *46.6* | *W/m.K* |
| $\rho$ | Density | *7810* | $kg/m^3$ |
| $C_p$ | Specific heat capacity | *475* | *J/kg.K* |
| $\kappa$ | Thermal diffusivity $\kappa = k/\rho C_p$ | $1.256\times10^{-5}$ | $m^2/s$ |
| $\rho_E$ | Electrical resistivity | $2.19\times10^{-5}$ | $\Omega/cm$ |

From **Figure 25** it is seen that a steady state is only reached around the $700^{th}$ cycle, although 95% of the temperature at the $1000^{th}$ cycle is already reached at the $55^{th}$ cycle. This will take no more than *3* seconds depending on $\omega$.

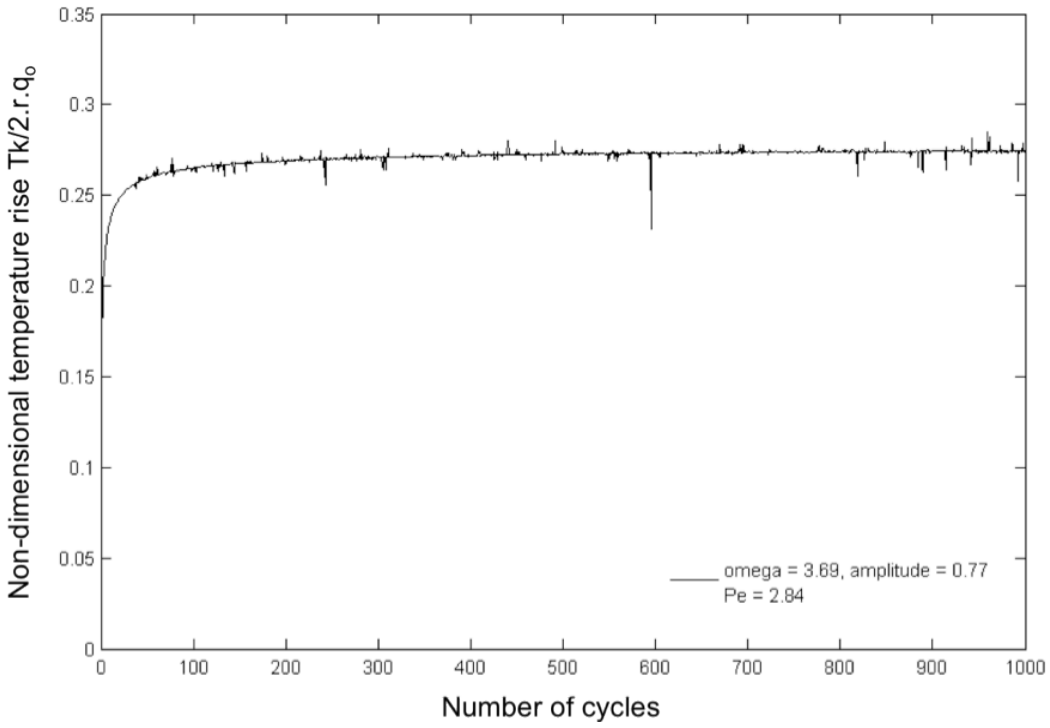


***Figure 25**. The maximum number of cycles to steady state at a Peclet number = 2.84.*

**Figure 26** shows the maximum steady state temperatures obtained at the *2000$^{th}$* cycle as a function of wear scar radius and oscillation frequency. The actual temperature rise could be calculated by use of equation (4.17).

$$T_{\max|steady} = T_{non}\frac{2r\mu P_o \omega A}{k\pi r^2} + T_{bulk} = T_{non}\frac{2\mu W \omega A}{k\pi r} + T_{bulk} \qquad (4.17)$$

**Figure 26** is a general plot that can be used to calculate the maximum temperature with use of (4.17). A thermal diffusivity of AISI E-52100 steel was used for the plot, which assumes constant values of thermal conductivity, specific heat capacity and density.

For an HFRR contact oscillating at *50 Hz* and a load of *200 g* with a friction coefficient of *2,* indicating initial junction growth and adhesion, and assuming a contact radius of *2.76×10$^{-5}$ m* and a bulk temperature of *60°C*, the contact temperature is calculated as *205°C*. If a contact radius of *1 μm* is used, which corresponds to the radius of an asperity, and all the other parameters are kept the same the maximum temperature is

calculated as *4200°C.* The melting point of steel is around *1400°C* (Perry & Green, 1997: 28-35), so a value of *4200°C* is definitely not realistic, but the model proves that temperatures in the order of a *1000°C* are obtainable, although they will only exist for very short periods of time as explained in *Chapter II* and won't be detected easily.

The model also indicates that the temperature drops very fast as the contact radius increases.

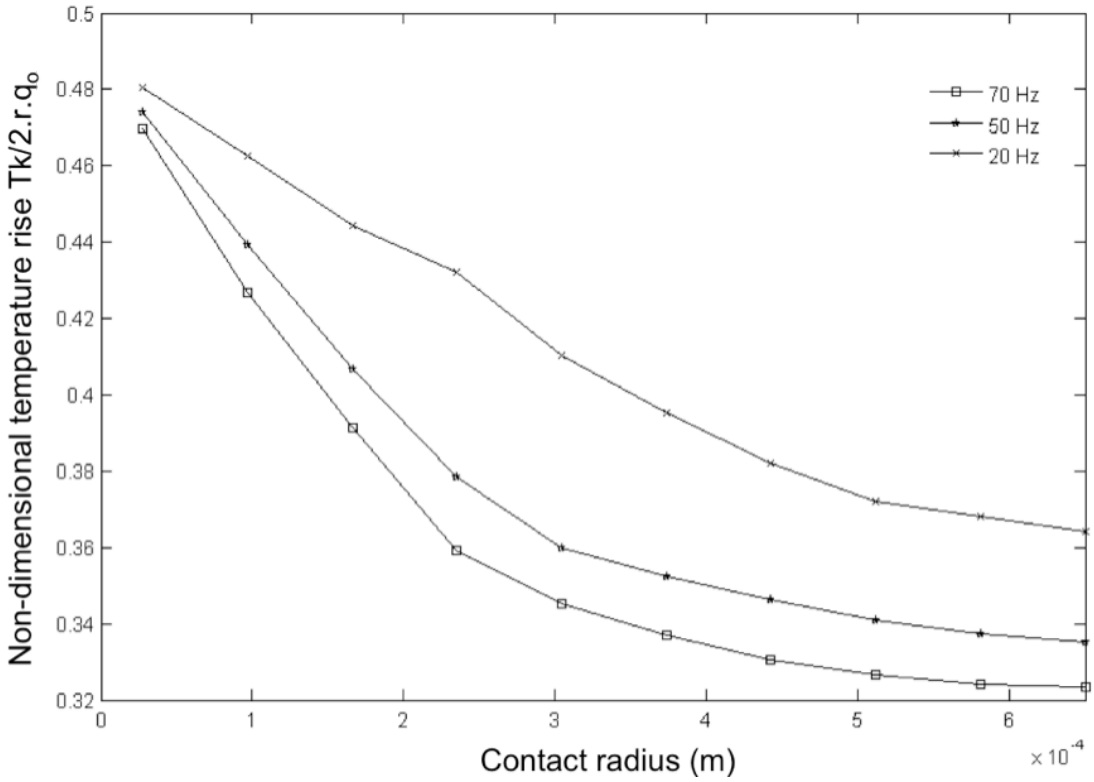


***Figure 26**. Maximum non-dimensional temperature rise as a function of contact radius for different oscillation frequencies (at steady state) (κ = 1,256×10$^{-5}$ m$^2$/s).*

Experimental validation of the model is extremely difficult as explained in *Chapter II*, but the model compares well with other models available in literature. Applying this model as a part of a more comprehensive boundary lubrication model in which the surface coverage of oxides and boundary lubricants can be approximated, together with a function which alters the thermal properties of the interface accordingly will yield more accurate results, but the development of such a model is not trivial.

# Chapter V

# RESULTS AND DISCUSSION

All the experimental and modelling results are shown and discussed in this chapter. The experimental results together with the modelling results are used in conjunction to bring more understanding to the underlying mechanisms relevant to the operation of the HFRR apparatus.

## 1. Wear tests performed according to ISO 12156/ASTM D6079

**Figure 27** shows the wear scar diameters obtained for the tests performed according to the ISO 12156-1 (2003) standard at different additive concentrations. Knothe & Steidley (2005) determined the *MWSD* of n-hexadecane according to the ASTM D6079 (2005) at *60°C* to be *572 µm*. Considering the reproducibility of the test method (*136 µm*) (ASTM D6079, 2005), this compares well with the average *MWSD* value reported here as *582 µm*.

The solid line shows the measured wear scar diameters for relative humidity larger than 30%, corresponding to the ASTM D6079 (2005) standard. The dashed line shows the *WS1.4* values, calculated as stipulated in ISO 12156-1 (2003). There is a slight difference between the two as a result of fluctuating laboratory conditions over the weeks of testing. The relative humidity varied between *30%* and *45%* and the temperature varied between *22°C* and *29°C*.

The standard deviations of the measurements are also shown for both the ISO and the ASTM tests. The general trend was that the standard deviation became larger as the additive concentration decreased, indicating that the system becomes more susceptible to small atmospheric changes the lower the additive concentration becomes.

Another interesting observation was that between *0,2* and *0,3 ml* volume was lost during each test, which corresponds to between *10%* and *15%* of the total volume.

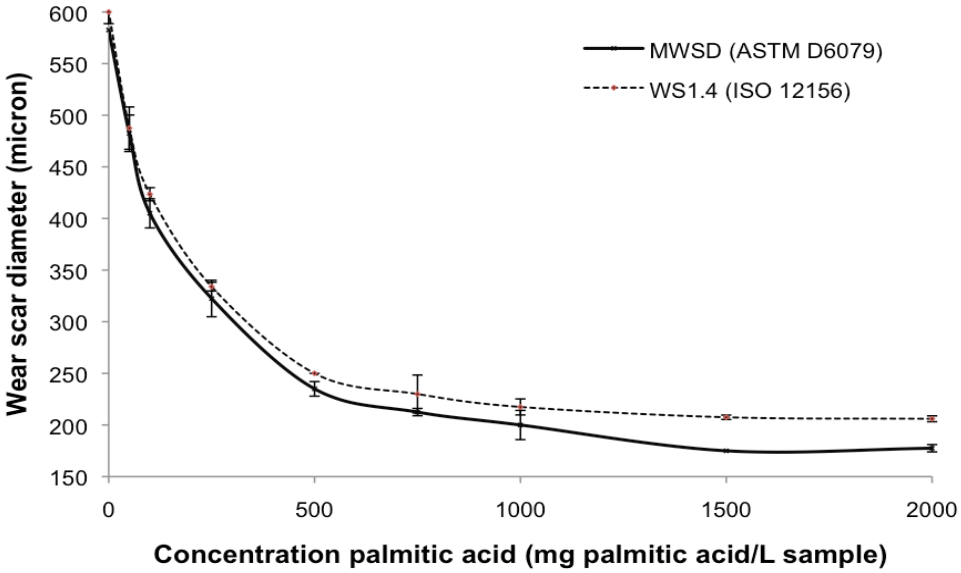


***Figure 27**. Wear scar diameter at the conditions set out in ISO 12156 and ASTM D6079 (50Hz, 60°C and 200g) for different additive concentrations.*

## 1.1. The *WS 1.4* wear scar correction vs. *MWSD*

**Figure 27** shows quite a large difference between the values obtained for the ISO 12156 and the ASTM D6079 standard. At high additive concentrations the values differed by as much as *25 µm*. The variation between the two curves is well within the test repeatability specified as *63 µm* (ISO 12156-1, 2003), but fall outside the standard deviation of this investigation at higher concentrations.

The equation used for the calculation of water vapour pressure in the ISO 12156 standard yields exactly the same values as equation (5.1), where $\mathrm{H}_R$ is the relative humidity and $p^*_{water}$ the saturation pressure at a specific temperature as shown in steam tables.

$$p_{water} = \mathrm{H}_R p^*_{water} \qquad (5.1)$$

A water vapour pressure of *1,4 kPa* at *25°C* corresponds to a relative humidity of *44%* at ambient pressure conditions. At a higher average water vapour pressure the wear

scar size will be corrected downwards, and for a lower vapour pressure upwards according to ISO 12156. Between two and four repeats were done for each of the additive concentrations, but there was no correlation between humidity and the *MWSD* or the *WS1.4* values.

In lubricated friction any oxygen and water must diffuse through the lubricant to get to the surface. The mole fraction water vapour dissolved in n-hexadecane can be calculated with *Henry's Law*, however *Henry's Law* data for water in n-hexadecane could not be found in literature.

The solubility of liquid water in n-hexadecane can be calculated with (5.2) where *A* = *6.418156*, *B* = *-4089.393,* $x_w$ is the mole fraction water and *T* is the temperature in *K* (Tsonopoulos, 1999).

$$\ln x_w = A + \frac{B}{T} \tag{5.2}$$

The results of equation (5.2) compare well with results presented by Kirchnerová and Cave (1999). Equation (5.2) shows an exponential increase in water solubility in n-hexadecane as temperature increases. More research should be done to fully understand the effect of atmospheric conditions on HFRR results.

## 1.2. Comparison of results with the model proposed by Fox (2005)

The shape of the curve obtained in **Figure 27** correspond with results by Anastopoulos *et al.* (2005), Anastopoulos *et al.* (2002), Anastopoulos *et al.* (2001) and Barbour, Rickeard and Elliott (2000). **Figure 28** shows the correlation between *WS1.4* values obtained experimentally and the model proposed by Fox (2005) in **Figure 14**. Section 'III' of the curve was adapted here to include a slight gradient, as this is more realistic for physical data. Section 'I' of the curve was negligibly small, which shows that even the slightest amount of acid does cause a wear scar reduction. A good correlation could not be obtained for section 'II' of the curve. This was not investigated further, but relating the size of the drop in *WS1.4* values between sections 'I' and 'III' and the concentration range over which this drop happens to thermodynamic properties warrants further study.

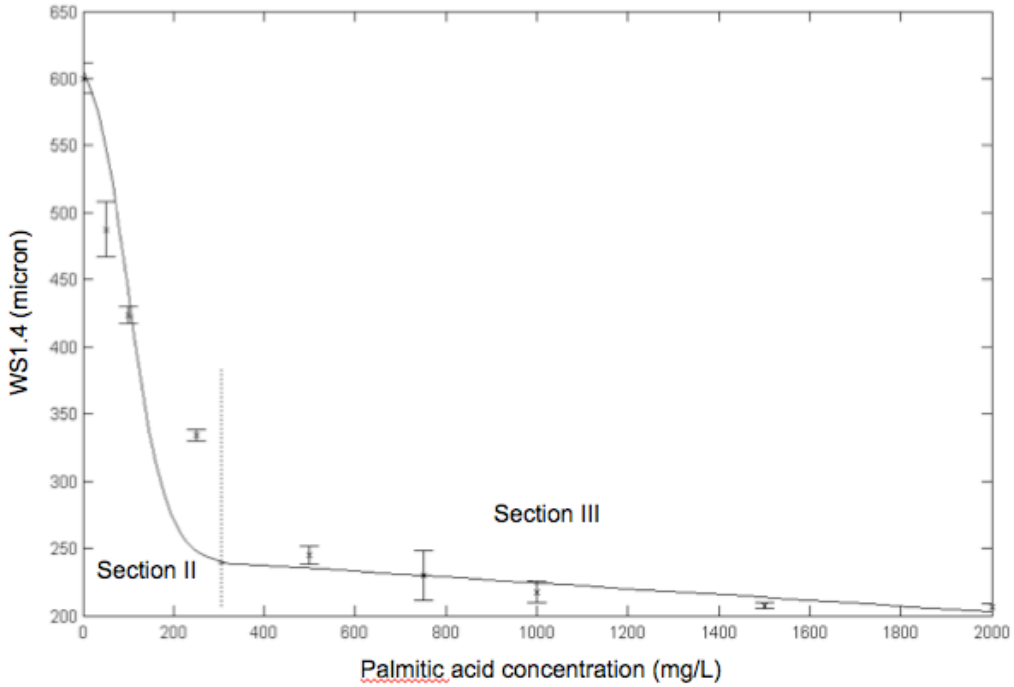


***Figure 28**. Fox's reverse sigmoidal curve fitted to the experimentally obtained data.*

## 2. Diesel analysis by *FTIR* and *GC×GC/TOF-MS*

All the concentration standards were analysed by *FTIR* analysis before and after the ISO 12156 HFRR test. The peak between wave numbers *1690 $cm^{-1}$* and *1760 $cm^{-1}$*, is characteristic of the *C=O* interaction of palmitic acid, and was used to detect any difference in the sample before and after testing. (Skoog, Holler & Nieman, 1998:410). Peaks that are characteristic of all the possible carbon-hydrogen interactions at wave numbers *2955 $cm^{-1}$*, *2919 $cm^{-1}$*, *2848 $cm^{-1}$*, *1467 $cm^{-1}$* and *721 $cm^{-1}$* were also used to detect differences before and after the HFRR test. No significant change in the transmittance of these peaks could be detected for any of the tests conducted. Reasons for this are discussed below:

There are three mechanisms that could have an effect on the composition of the sample, as discussed in *Chapter II*.

- *Catalytic decomposition of organic molecules*, which will lead to the formation of gases such as methane, carbon monoxide and hydrogen, and shorter

carbon chains in the liquid. This mechanism could cause a change in the *C=O* peak as a result of carbon monoxide gas formation.

- *Oxidation*, which will also cause the shortening of chains and the evaporation of methane, but will be accompanied by the formation of oxygenates such as carboxylic acids and ketones, which will be visible in the transmittance of the *C=O* and *C-O* peaks.
- *Metal soap formation through chemisorption*, which will cause a drop in the transmittance of the *C=O* peak, as some of the acid is reacted to the surface.

FTIR of the liquid samples alone cannot provide enough information to establish which mechanisms played a role during any test. The loss of sample during the test can be attributed to *catalytic decomposition*, which will affect a change in the C-H interactions, but possibly not in the C=O interaction depending on the formation of carbon monoxide.

*GC×GC/TOF-MS* could give a more focussed picture of what happens to the composition of the liquid sample during a test. **Figure 29** shows the relative area percentage of each compound found in the sample before and after an ISO 12156 test conducted with a palmitic concentration of *1500 mg/l*.

**Figure 29** shows that hexane and heptane were formed during the friction test. This is a strong indication of the *catalytic decomposition* of the $C_{16}$-hydrocarbons in the sample. It can't be said with certainty whether the concentration of palmitic acid decreased or increased, but oxidation of the sample did not cause other oxygenates to be formed.

*Reflectance FTIR microscopy* of the HFRR bottom specimen should be performed to indicate soap formation.

# 3. Identification of friction and wear mechanisms

## 3.1. Mechanism of oxidative friction and wear with no lubricant

**Figure 30** shows a plot of *WS1.4* values as a function of sliding time. The test had to be stopped and the wear scar measured at several intervals. This test is referred to as

the dynamic wear test and was performed at the conditions set out by ISO 12156-1 (2003). Two tests were performed in accordance with the ISO 12156 method for the full *75 min*, without stopping and their average was also plotted in **Figure 30**. The final data point of the dynamic wear test fell within the standard deviation range of the ISO 12156 tests and therefore the effect op stop-starting the test 12 times between the begin and the end of the test was proven to be negligible.

The extent of visible surface damage, together with *WS1.4* data and friction coefficient data in **Figure 31** give clues as to which wear mechanisms were dominant during the sliding process.

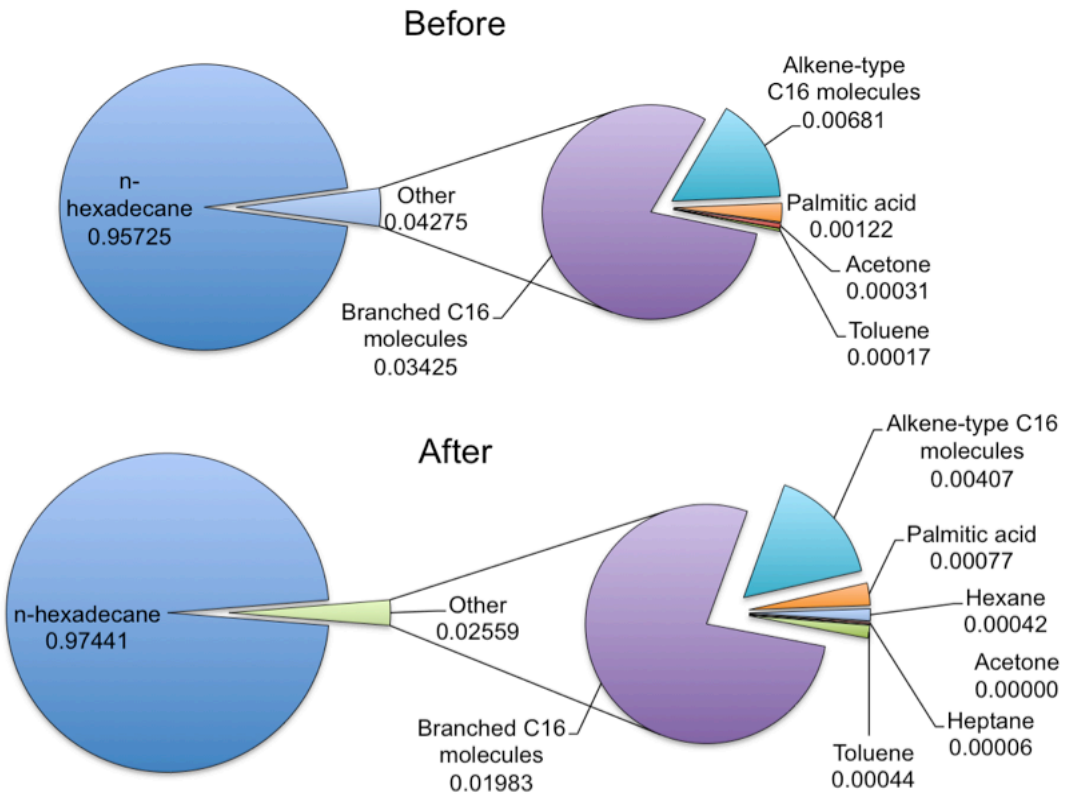


***Figure 29**. GC×GC/TOF-MS analysis results before and after an ISO 12156 HFRR test lubricated with 1500 mg/l palmitic acid.*

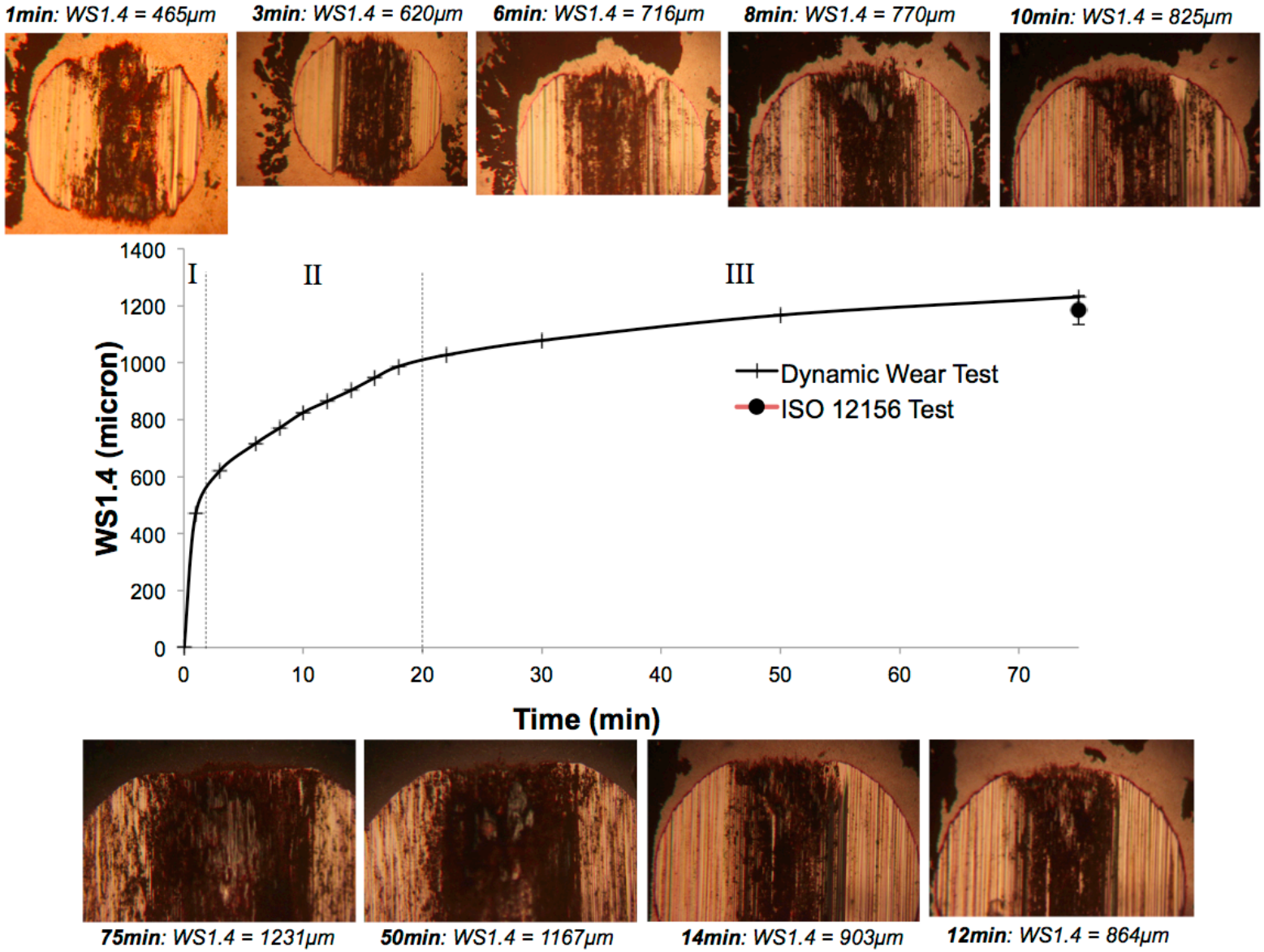


***Figure 30**. Wear rate of HFRR test with photos of wear scars as time progresses for an unlubricated (dry) system.*

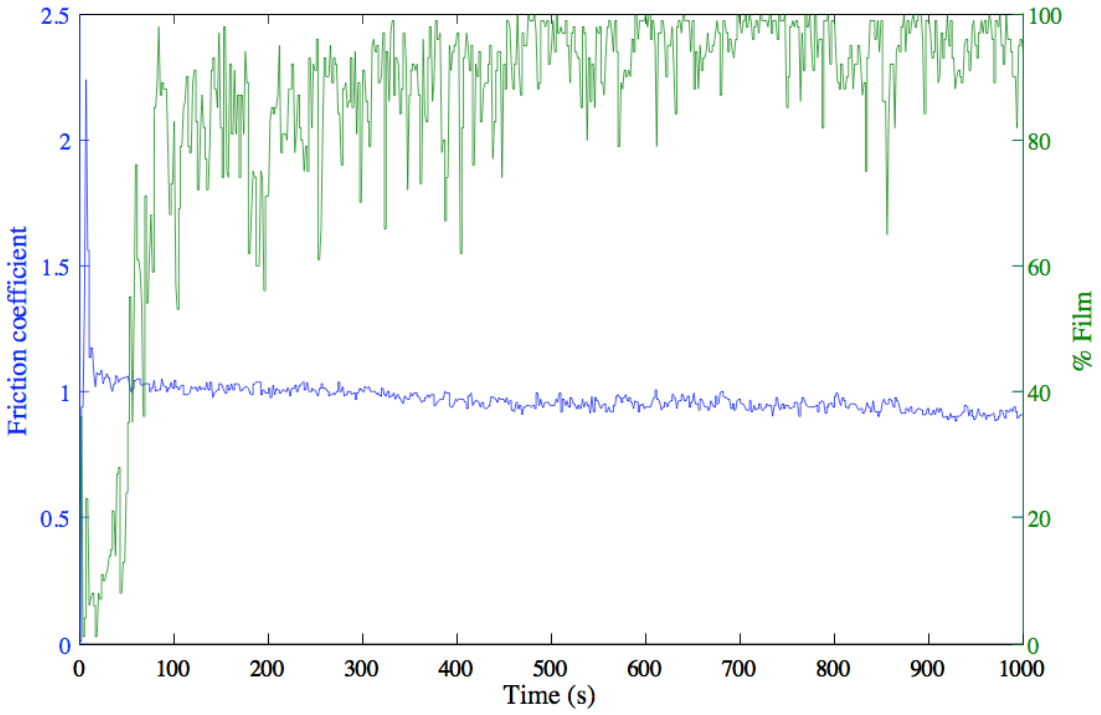


***Figure 31**. Friction coefficient and percentage film data for the first 1000s of the unlubricated test. The decreasing trend in friction coefficient was maintained until the completion of the test at 4500s.*

*Adhesion* and *abrasion* are the most dominant wear mechanisms within the first minute. A friction coefficient of more than *2* indicates strong adhesion between the ball and disk, initiating rapid wear due to “cold-welding” of the surfaces. This most probably leads to metal transfer, which causes *two* and *three body abrasive wear* as shown by the scratches in the photos of **Figure 30**.

Between the third and the twentieth minute wear seems to increase linearly with time (**Figure 30**), which indicates a change in mechanism from what was seen in the first minute. The photos in **Figure 30** show very little change although the size of the wear scar is increasing, which means that the rate of oxide growth is equal to the rate of wear scar growth. The friction coefficient shows a decreasing trend as time progresses, as can be seen in **Figure 31**.

From the twentieth minute there is a decrease in the wear rate and the friction coefficient shows still shows a slight decrease with time. There is a large increase in “dark particle” coverage as time progresses as shown in **Figure 30**.

The “dark particle” coverage of a surface tested according to ISO 12156 (**Figure 32(a)**) was larger than that of the dynamic wear test at *75 min*. This layer was removed easily by washing the specimen in toluene and acetone. A very fine dust with a red-brown appearance was also visible on the bottom specimen after the completion of both tests, as photographed in **Figure 32(b)**.

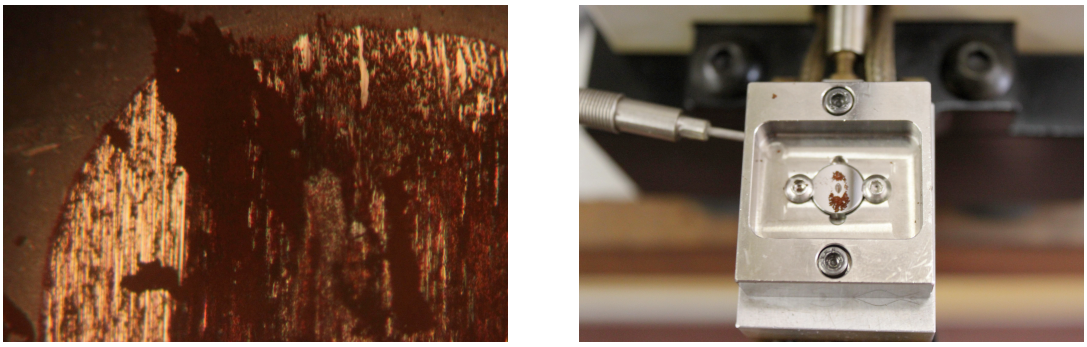

(a) (b)

***Figure 32**. (a) The wear scar obtained by running the ISO12156 test for 75min without stopping. Even more fine oxide is visible on the scar. (b) Red oxide dust is visible on the bottom specimen of the HFRR after both the dynamic wear test and the ISO12156 test.*

The proposed wear mechanism is shown schematically in **Figure 33**.

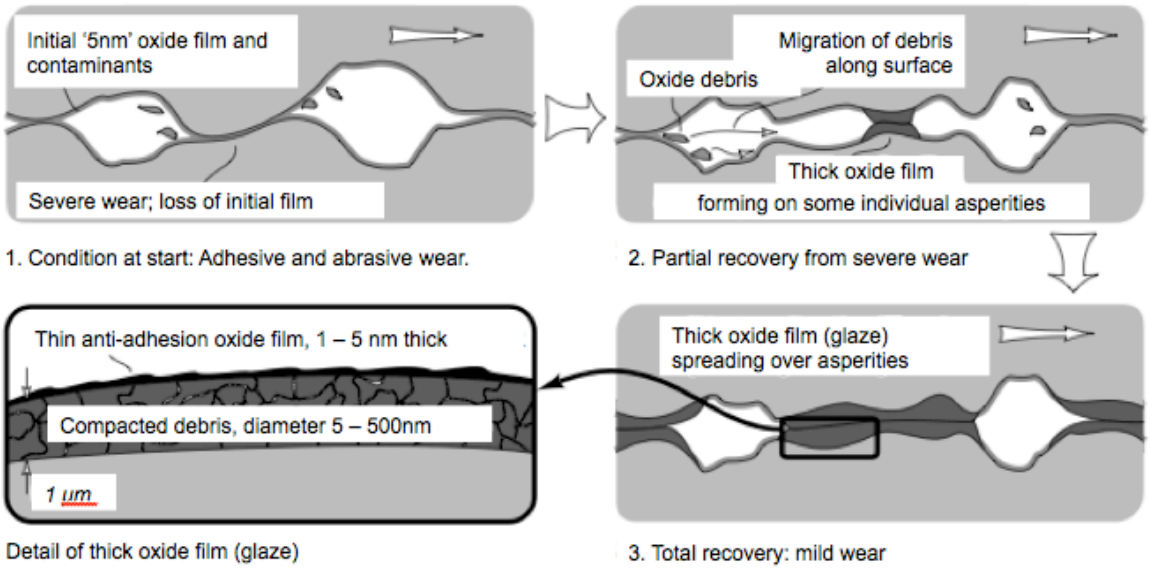


***Figure 33**. Mechanism of oxidative wear at low sliding speeds (adapted from Stachowiak & Batchelor, 2005: 564).*

In the HFRR test the average sliding speed is *0,1 m/s*. According to Stachowiak and Batchelor (2005: 564) this sliding speed is not sufficient to cause enough frictional heat needed for rapid oxidation. Fractured oxides and oxidised wear particles, as a result of initial *adhesion, abrasion* and *fatigue*, form a mixture that coagulates into 'islands' causing a reduction in friction coefficient (Stachowiak & Batchelor, 2005: 564). The wear particles formed expose nascent metal surface, which reacts rapidly with atmospheric oxygen, and the film thickens until almost the whole surface is covered with oxide, thereby inhibiting further adhesion and wear scar diameter growth.

From the results in **Figure 30** it seems as if the wear mechanism can be divided into *3 wear regimes*:

- *Regime I*. Adhesion dominated wear, with the added effects of abrasive and fatigue wear;
- *Regime II*. A transition regime, and
- *Regime III*. A regime of oxidative dominated wear.

AISI E-52100 steel contains between *96.5%* and *97.3%* iron. Other compounds include carbon, chromium, manganese, phosphorous, silicon and sulphur. Most of the oxides formed in the contact will therefore be iron oxides (MatWeb Material Property Data, 2010)

An average percentage film of *94%* was recorded for the dry test (**Figure 31**), which indicates that contact resistance not a very effective measure of determining boundary lubricant film efficiency.

## 3.2. The effect of humidity and oxides on the lubrication of a dry contact

Oláh *et al.* (2005) used Raman spectroscopy to identify the type of oxides formed on the surface during an HFRR test. Hematite ($\alpha$-$Fe_2O_3$) and magnetite ($Fe_3O_4$) were the most prominent species identified. According to Tannhauser (1962) the electrical resistivity of hematite is close to a *100* times larger than for magnetite and wustite ($Fe_{1-x}O$). The formation of hematite is most probably the cause of the high percentage film measurement. Hematite also has a distinct red-brown colour, as observed in **Figure 32** (Pourbaix, 1966: 308).

**Figure 34(b)** shows the phase diagram for the iron-oxygen system as calculated by Ketteler *et al*. (2001), which shows that a high temperatures are needed for the formation of magnetite. This corresponds well with the observation of Oláh *et al.* (2005), who found that magnetite formation is usually associated with high levels of surface damage. The physical and thermal properties of hematite and magnetite are shown in **Table 7**.

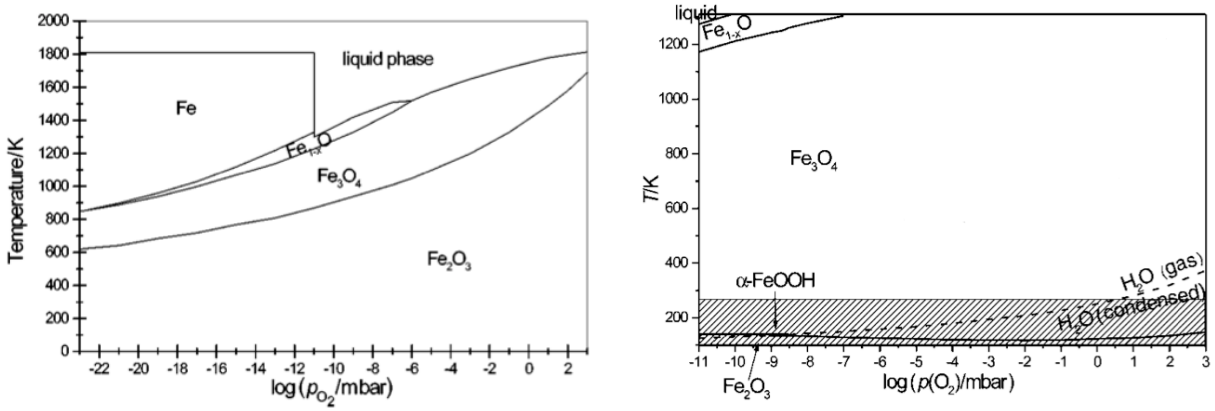


(a) (b)

***Figure 34**. (a) Phase diagram of the iron-oxygen system. (b) Phase diagram of the iron-oxygen-water system (adapted from Ketteler et al., 2001).*

***Table 7**. Physical and thermal properties of hematite and magnetite (from Mølgaard & Smeltzer, 1971). Properties at 25°C.*

| Property | Hematite ($\alpha$-$Fe_2O_3$) | Magnetite ($Fe_3O_4$) |
|---|---|---|
| Melting point | *1565°C* | *1538°C* |
| Density ($\rho$) | *5260 kg/m$^3$* | *5000 kg/m$^3$* |
| Specific heat capacity ($C_p$) | *650,6 J/kg.K* | *619,4 J/kg.K* |
| Thermal conductivity ($k$) | *3,822 W/m.K* | *6,413 W/m.K* |
| Thermal diffusivity ($\kappa$) | *1,1168×10$^{-6}$ m$^2$/s* | *2,0707×10$^{-6}$ m$^2$/s* |

These physical and thermal properties were used to calculate the contact temperatures as a result of a steel-steel, hematite-hematite and magnetite-magnetite contact for one sliding oscillation. Equation (4.17) was used to calculate the temperature. A friction coefficient of *1* was used as obtained experimentally in **Figure 31**

and sliding conditions were as specified by ISO 12156-1 (2003). The Hertzian contact radius was used for this simulation. The results are shown in **Figure 35**.

The two iron oxides have very low thermal conductivities compared to the clean steel surface, causing the contact temperatures to be very high. **Figure 35** is plotted for a single oscillation or duration of *0.02s*, which proves that high temperatures are obtainable even at larger contact radii than asperity contacts.

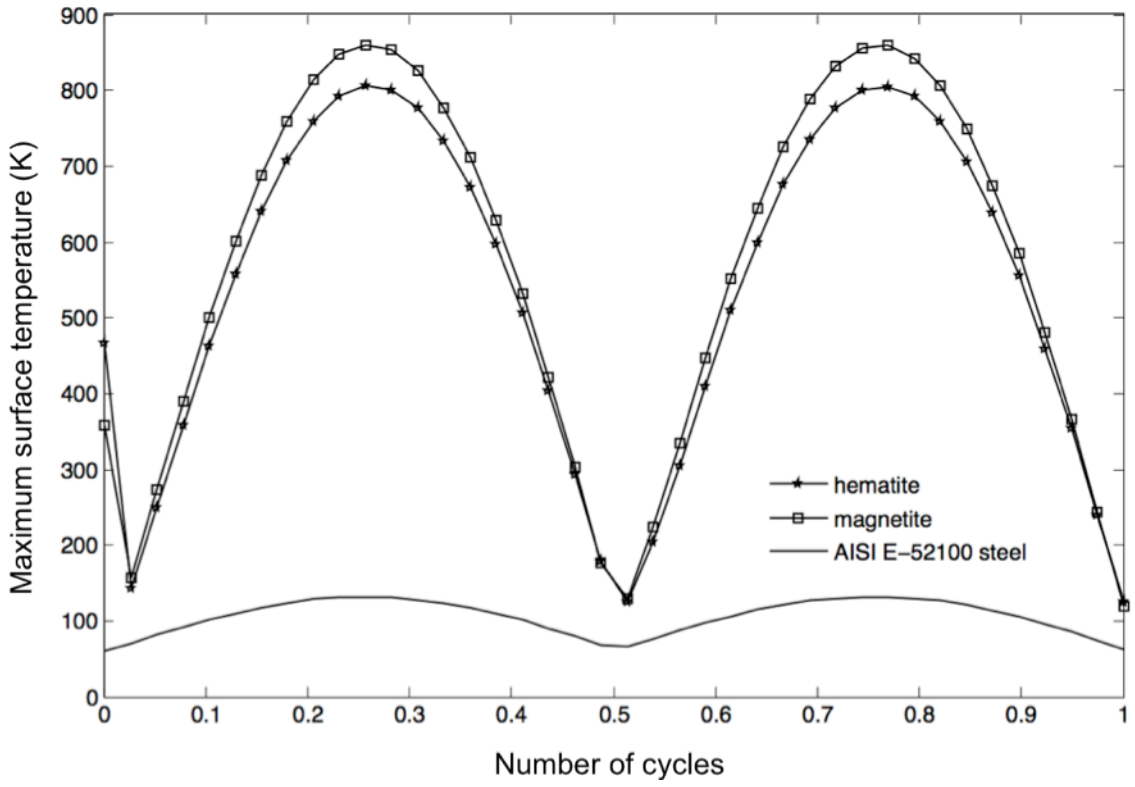


***Figure 35**. The maximum surface temperature obtained for sliding one cycle on AISI E-52100 steel, hematite and magnetite at a friction coefficient of unity and a bulk temperature of 60°C.*

**Figure 34(a)** shows the phase diagram for the iron-oxygen-water system. The introduction of water into the system introduces the formation of goethite (*α-FeOOH* or $Fe_2O_3 \cdot H_2O$), bernalite ($Fe(OH)_3$) and $Fe(OH)_2$ (Ketteler *et al.*, 2001). The colour of ferric hydroxide ($Fe(OH)_3$) is also red-brown and could also have been formed in dry sliding conditions in very humid conditions (Pourbaix, 1966: 308).

The formation of iron oxides and hydroxides decrease the reactivity of the pure metal to such an extent that boundary lubricants can physisorb or chemisorb to the surface without being decomposed during sliding. According to Stachowiak and Batchelor (2005: 384) the formation of a metal soap layer requires the reaction of an iron hydroxide and a fatty acid. Under certain conditions the soap will also be formed by the reaction of iron oxide with fatty acid, but the reactivity of the oxide is lower than that of the hydroxide. Increased humidity will therefore cause more rapid soap formation and better wear protection coupled with a decrease in friction. This is explored further in the next section.

## 3.3. Mechanism of lubricated friction and wear

Introduction of a lubricant complicates friction and wear mechanisms to a great extent. Analysis of friction and wear as a function of additive concentration was carried out at conditions set out by ISO 12156-1 (2003).

Friction coefficient data of all the concentration standards tested in this investigation is presented in **Figure 36**.

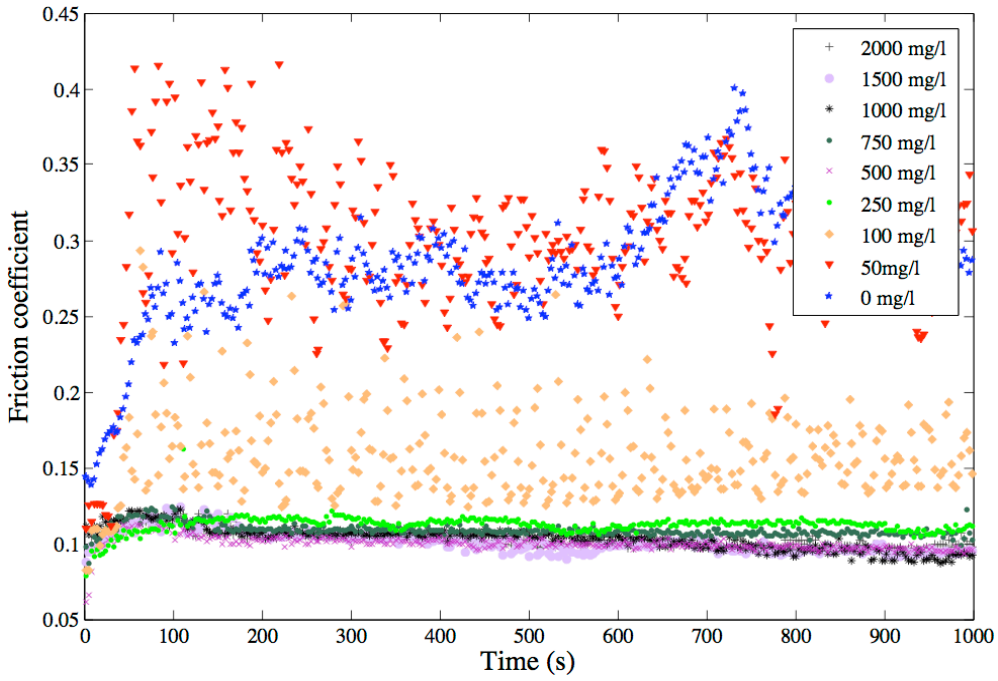


***Figure 36**. Comparison of friction coefficients obtained for all the additive concentrations. Friction becomes unstable at concentrations smaller than 100mg/l.*

**Figure 36** shows a slight decrease in the coefficient of friction of *2000*, *1500*, *1000*, *750* and *500 mg/l* palmitic acid. This is very similar to the friction behaviour of an unlubricated (dry) contact, although the average friction coefficient is *0,1* for lubricated sliding as opposed to *1* for air lubricated sliding. This large difference in friction coefficient shows that the lubricant film, although not perfect, does give some measure of protection additional to an iron oxide film.

The frictional behaviour of *2000*, *1500*, *1000*, *750*, *500* and *250 mg/l* palmitic acid in n-hexadecane were very similar, all of them having an average friction coefficient of around *0,1*. A palmitic acid concentration of *100 mg/l* and below yielded friction coefficient values between *0,15* and *0,45*. These values are still substantially lower than the values obtained for air lubricated sliding. These results agree with results obtained by Okabe, Masuko and Sakurai (quoted by Stachowiak and Batchelor, 2005: 372), who found that the "friction transition concentration" of palmitic acid in pure hexadecane is between *0,4* and *0,5 gmol/m*$^3$, which corresponds to between *103 mg/l* and *128 mg/l*. As mentioned in *Chapter II*, it is unlikely that an adsorbed film will equilibrate in a sliding contact. The "friction transition concentration" is seen as the lowest concentration at which fatty acids will replenish a friction-damaged adsorbate film during repetitive sliding. Stachowiak and Batchelor (2005: 372) also states that *adsorption lubrication* will not be effective unless the adsorbed film is in a near-perfect condition. The rate-limiting step in adsorption lubrication under sliding conditions is believed to be the re-adsorption of additive to the surface as illustrated in **Figure 37**.

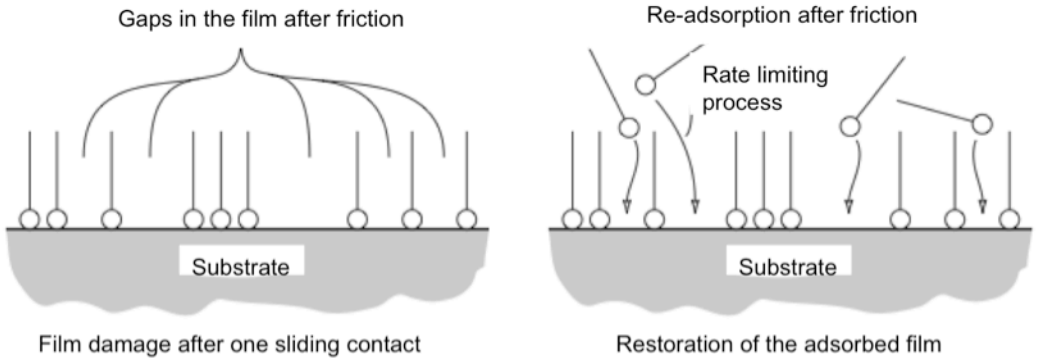


***Figure 37**. The re-adsorption of fatty acids after one sliding contact (adapted form Stachowiak & Batchelor, 2005: 372).*

The time needed for re-adsorption will be a function of the bulk concentration of palmitic acid at constant temperature. Chen and Frank (1989) did some work on the adsorption of stearic acid on aluminium surfaces. They used a time-dependent Langmuir adsorption isotherm, as shown in (5.3), to describe the adsorption.

$$\frac{d\theta}{dt} = \frac{k_a}{N_o} c(1-\theta) - \frac{k_d}{N_o}\theta \tag{5.3}$$

where $\theta$ is fractional coverage (-);

$k_a$ is the adsorption rate constant (*m/s*);

$N_o$ is the surface adsorbate concentration at full coverage (*gmol/m*$^2$);

$c$ is the additive concentration in the bulk (*gmol/m*$^3$); and

$k_d$ is the desorption rate constant (*gmol/m*$^2$*s*)

Equation (5.3) was integrated with initial condition $\theta = 0$ *at* $t = 0$. The integration gave (5.4). Equation (5.4) becomes the equilibrium Langmuir isotherm at $t \rightarrow \infty$ (5.5), where $\Delta G_a^\circ$ (*kJ/gmol*) is the free energy of adsorption at infinite dilution (Chen & Frank, 1989). **Table 8** shows the values of the constants at *25°C*.

$$\theta = \frac{k_a c}{k_a c + k_d}\left[1 - \exp\left\{-\frac{k_a}{N_o}\left(c + \frac{k_d}{k_a}\right)t\right\}\right] \tag{5.4}$$

$$\theta_{eq} = \frac{k_a c}{k_a c + k_d} = \frac{c}{c + \psi} \qquad \text{where} \qquad \psi = \frac{k_d}{k_a}\ \alpha\ \exp\left(-\frac{\Delta G_a^\circ}{RT}\right) \tag{5.5}$$

Chen and Frank (1989) investigated the kinetics of the adsorption of stearic acid onto aluminium oxide. It was assumed that the aluminium oxides are more reactive than iron oxides, so the results presented below represent the best-case scenario. **Figure 38** shows the time it takes for the additive to reach full surface coverage at *25°C*.

***Table 8**. Constants obtained by Chen and Frank (1989) for the adsorption of stearic acid on aluminium at 25°C.*

| Parameter | Value |
|---|---|
| Adsorption rate constant | $3{,}32\times10^{-4}$ |
| Desorption rate constant | $1{,}66\times10^{-13}$ |
| $N_o$ (corresponds to area of *0,2* $nm^3$/fatty acid molecule) | $8{,}3\times10^{-10}$ |
| $\Delta G_a^{\circ}$ | *-38,52* |

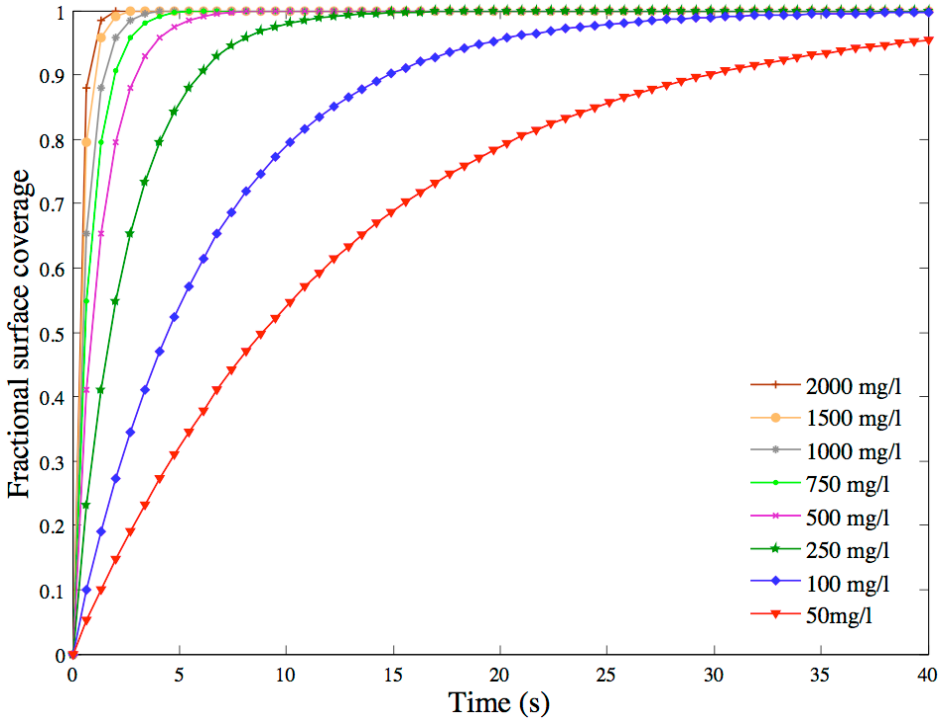


***Figure 38**. Surface coverage vs. time for different palmitic acid concentrations at 25°C.*

The HFRR, operated according to ISO 12156, will have a bulk temperature of *60°C*. Equation (5.5) shows that an increased temperature will increase the ratio $k_d/k_a$, therefore favouring desorption of additive. At *60°C* adsorption will be slower than at 25*°C*.

Before an HFRR test at *60°C* can start, the temperature has to stabilise at that setpoint temperature. This usually takes a minute or two, which should be sufficient for the additive to reach full surface coverage. When the test starts this film is slowly destroyed oscillation by oscillation until oxide-oxide or metal-oxide or metal-metal

contact occurs and the friction and contact temperature increases. Referring to **Figure 38** and knowing that the temperature will be higher than *25°C*, it is difficult to see how the additive film will restore itself to near perfect condition within the time frame of *1* oscillation (*0,02 s* at *50 Hz)*, which is necessary for effective *adsorption lubrication*. Adsorption could surely also not happen in the contact zone, due to diffusion limitations as a result of the high pressure. If the previous statement is correct there will never be adsorption of additive to the top specimen, but only to the bottom specimen in the sliding track outside the contact area. This hypothesis is proved by friction results obtained experimentally and shown in **Figure 39**.

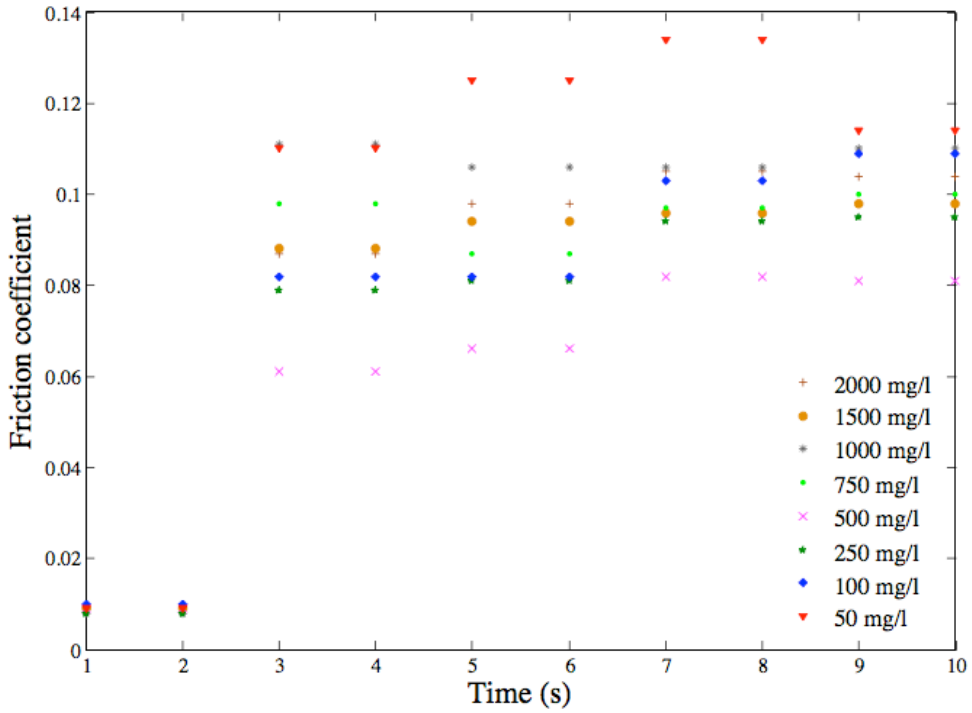


***Figure 39**. Friction coeffient in the first 10 seconds of an ISO 12156 test. The values at 1 s and 2 s are the same for all the additive concentrations.*

**Figure 39** shows that the friction coefficient in first two seconds are the same and equal for all the additive concentrations tested in this investigation. This friction value of around *0,01* corresponds well with frictional shear values obtained by Tabor (1981) and Briscoe and Evans (1982) for stearic acid and iron stearate films. At the *3rd* second the friction jumps upwards, which serves as an indication that the film was destroyed

between the *2nd* and the *3rd* and that oxide and metal contact could no longer be avoided. This took between *100* and *150* oscillations. The six stages of friction, as described in *Chapter II* causes a slight increase in friction from the *3rd* second, but the friction decreases again slightly when the asperities have been flattened out. The frictional values between the *3rd* and the *10th* second did not increase as the additive concentration decreased, nor was it related to the water vapour pressure calculated with (5.1). A combination of these two and the repeatability of the test should be responsible for this strange distribution of data points.

Increased humidity could lead to the formation of iron hydroxides with higher reactivity as discussed earlier, which could decrease the adsorption times and improve the ability of the film to decrease wear. This was however not seen experimentally. In some instances increased humidity led to increased wear and in other cases the opposite was true. This mechanism is not understood yet.

A dynamic wear test, similar to the one for an air lubricated contact, was also done for *250 mg/l* palmitic acid. The results are shown in **Figure 40**. There was a rapid increase in the wear scar diameter during the first minute. From the second minute the wear rate decreased slightly as time progressed. The photos show no sign of *adhesive* or *abrasive wear*. Only *oxidative wear* is visible. Interestingly, there were two types of oxide formations:

- An oxide layer that formed the shape of the wear scar; and
- A ring of oxide outside the contact area.

The oxide layer that formed the shape of the wear scar could not be removed by ultrasonically stirring the specimen in toluene and acetone, whereas the oxide outside the contact area was easily washed away. There are some similarities between the wear mechanism here and what was seen in **Figure 30**.

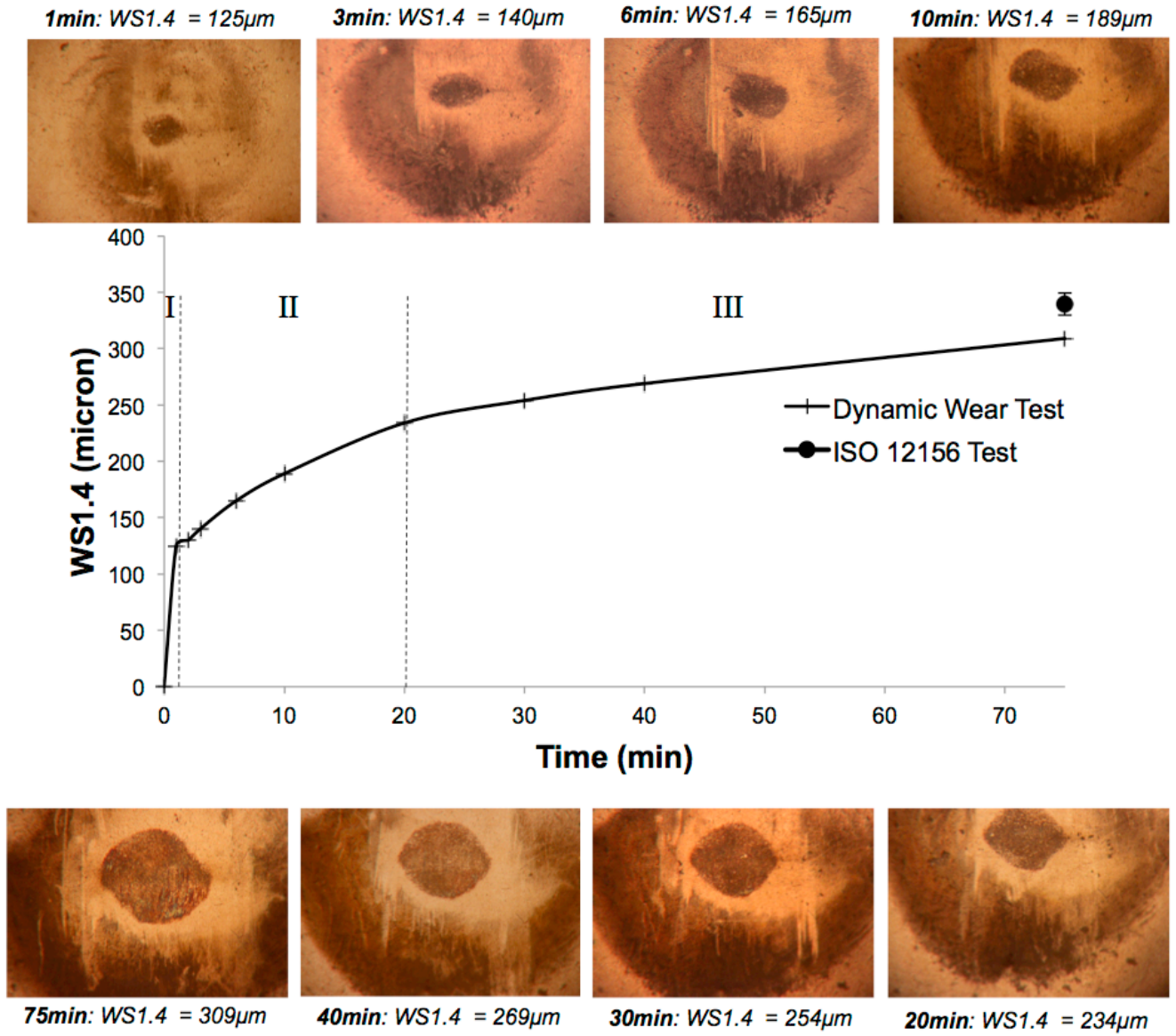


***Figure 40**. Wear rate of HFRR test and photos taken of wear for system lubricated by 250mg/l palmitic acid.*

The wear mechanism in **Figure 40** can also be divided into the *3 wear regimes* discussed earlier:

- *Regime I*. Adhesion dominated wear, this time with no signs of abrasion and fatigue;
- *Regime II*. A transition regime, and
- *Regime III*. A regime of oxidative dominated wear.

The addition of the *250 mg/l* palmitic acid in n-hexadecane caused the adhesion dominated wear regime to be smaller and it decreased the wear rate in the transition regime. At higher additive concentrations pictures of the wear scar at *75 min* looked very similar to the picture in **Figure 40**, but the wear scar diameters are smaller.

Therefore, the introduction of a lubricant eliminated *adhesive* and *abrasive wear*. According to *Chapter II adhesion* is the cause of most of the friction and wear and it happens through the mechanism of junction growth. The HFRR data acquisition system is not sufficient to study junction growth, seeing that the first measurement that the HFRR makes is at *1 s* or *50* oscillations. It would be interesting to see the wear scar diameter after *1* oscillation as a function of palmitic acid concentration at constant humidity.

Note that in both the unlubricated and the *250* mg/l palmitic acid lubricated contacts, *40%* of the wear scar diameter at *75 min* was obtained in the first minute.

The formation of a soap layer will be dependent on the temperature just outside the contact area. **Figure 41** shows the temperature distribution in the sliding direction for a steel-steel, hematite-hematite and a magnetite-magnetite contact. Magnetite is also considered here, seeing that Oláh *et al*. (2005) recorded traces of magnetite even for lubricated sliding. The ISO 12156 sliding conditions were used for the simulation together with a friction coefficient of *0,1* as found experimentally in **Figure 36**. The plot is not symmetrical around the centre of the contact, because the simulation was run for the first oscillation and a steady state has not yet been reached. From **Figure 41** it can be seen that the heat source is moving from right to left, which means that the contact is slightly more heated on the right hand side. The temperature over this “tail” will to a great extent determine which surface reactions take place. A soap layer formed by

palmitic acid is strengthened by n-hexadecane through the mechanism of *chain matching*. A transition temperature of *240°C* was reported earlier in *Chapter II*. Such high contact temperatures are not reached in HFRR contacts the size of the Hertzian radius and the soap layer will therefore survive if formed. Asperity contacts will cause local melting of a soap film that is not in perfect condition.

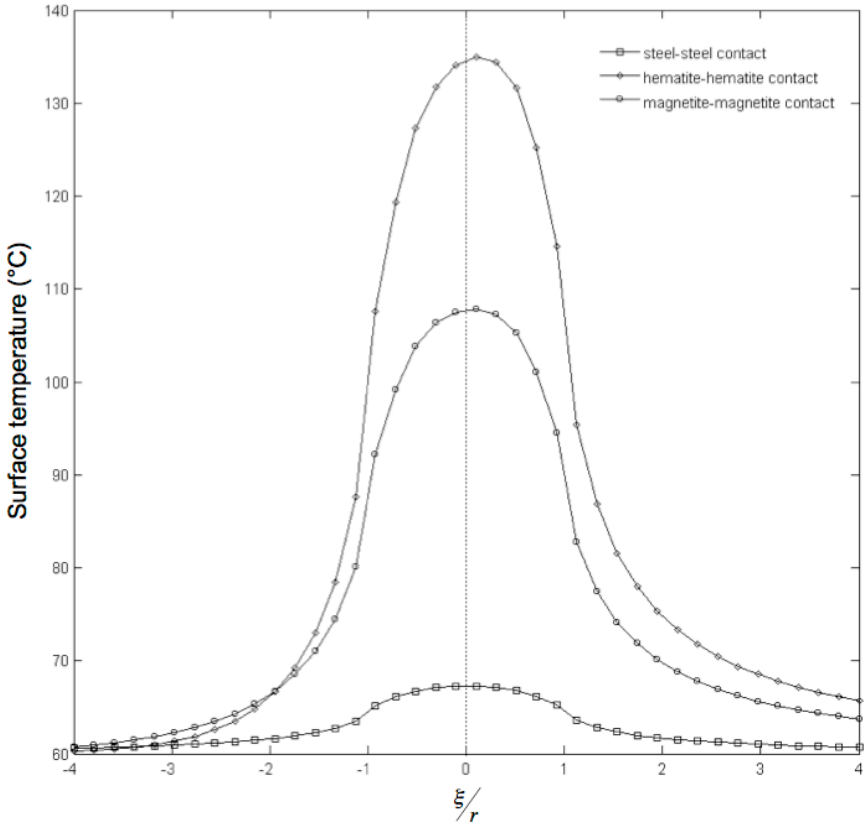


***Figure 41**. Contact temperature plotted against non-dimensional sliding direction for a steel-steel, hematite-hematite and magnetite-magnetite contact at a friction coefficient of 0,1 and the Hertzian contact radius.*

## 3.4. Scanning electron microscope (SEM) results

**Figure 42** shows the surface of the top specimen of an HFRR after the completion of an ISO 12156 test at an additive concentration of *2000 mg/l*. The surface shows small patches of oxide formation, which is another proof that contact is not on the boundary film alone and that metallic or metal oxide contact does occur.

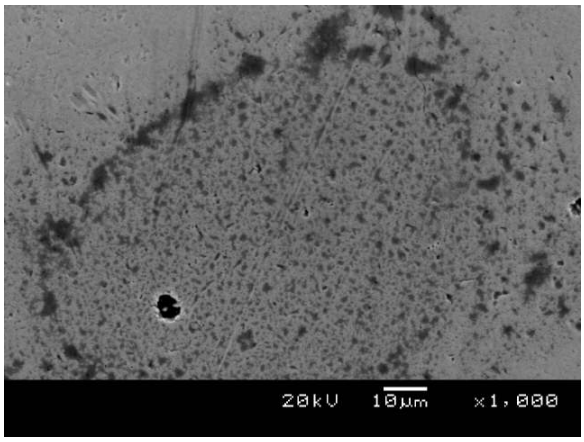


***Figure 42**. The surface of an HFRR top specimen (ball) after the completion of an ISO 12156 test lubricated with 2000mg/l palmitic acid in n-hexadecane, magnified 1000 times.*

**Figure 43** shows pictures taken of the top specimen after an ISO 12156 test using n-hexadecane as liquid fuel (no additive) and **Figure 44** shows pictures of the bottom specimen. The most prominent wear mechanism is *three* and two *body abrasive wear* caused by extreme *adhesive wear*. **Figure 43(a)** shows a wear particle moved to the side of the contact, causing abrasion of the top and bottom specimens (**Figure 44**).

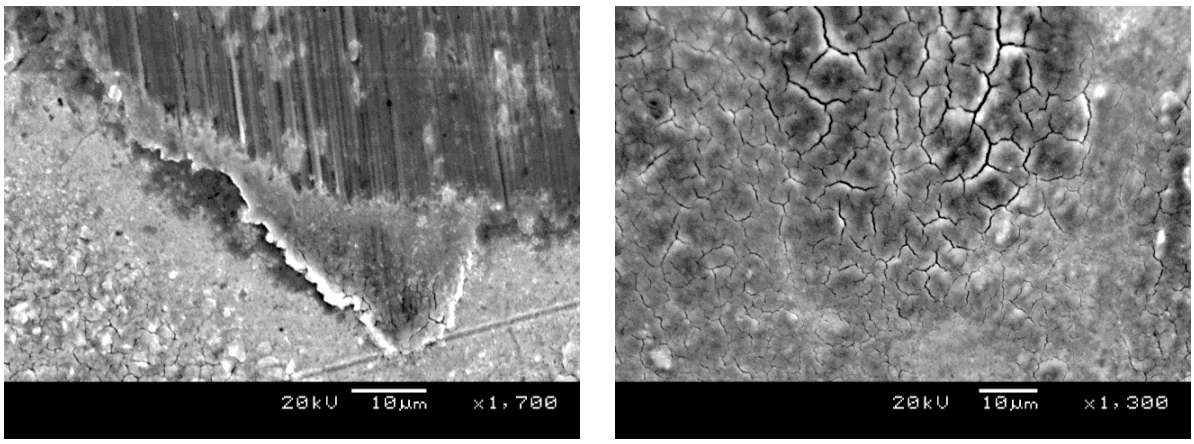


(a) (b)

***Figure 43**. The surface of an HFRR top specimen after an ISO 12156 test lubricated with n-hexadecane. (a) Transfer particles are formed due to adhesion and is moved to the side of the contact area causing abrasive wear. (b) Cracks on the surface just outside the contact area.*

**Figure 43**(b) brought another wear mechanism to light that was not detected by analysing the wear scar pictures with a light microscope: *fatigue wear*. This is an indication that the reciprocating motion causes a high degree of deformation in the material, which leads to cracks at weak spots in the material. **Figure 43(b)** gives no indication of wear particles forming form these cracks, but this could cause even more abrasive damage. This was not investigated further.

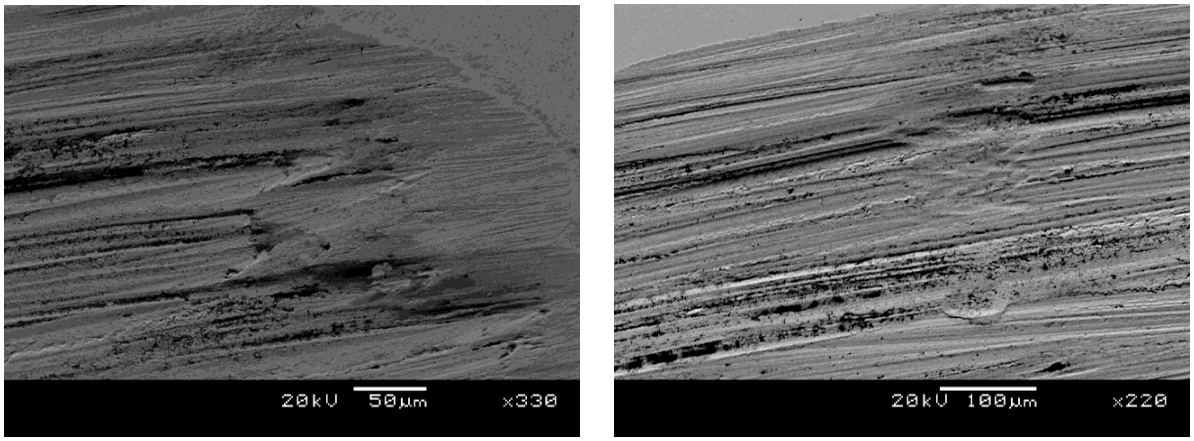


***Figure 44**. The bottom specimen of an HFRR after the completion of an ISO 12156 test lubricated with n-hexadecane. The surface is very rough and uneven and the formation of oxides are evident.*

The bottom specimen is very abraded and uneven. Three distinct colours are visible in **Figure 44**. The lightest colour is most probably steel, the black patches magnetite and the other colour should be hematite. This will have to be confirmed with Raman spectroscopy.

## 3.5. The effect of changed sliding conditions on friction and wear

Friction and wear tests were conducted at different combinations of frequency, load and temperature with the *2000 mg/l* palmitic acid concentration standard. **Figure 45** shows a shear stress-pressure relationship at different conditions of frequency and temperature. In most cases a linear relationship was obtained that agreed with equation (2.11). The values of $\tau_o$ and $\alpha$ were however much larger than the values obtained by Briscoe and

Evans (1982) and Tabor (1981) for stearic acid and stearate soap films. It is concluded that even at *2000 mg/l* palmitic acid friction is predominantly due to iron oxides.

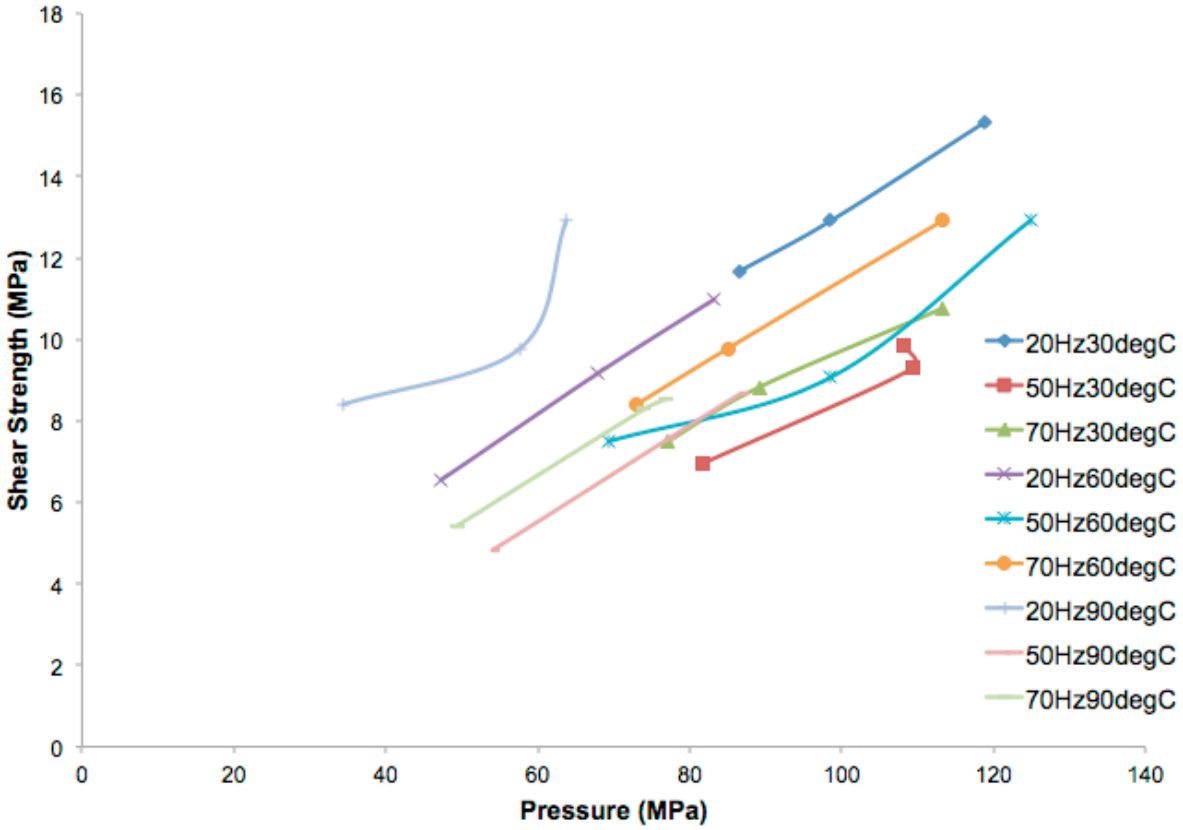


***Figure 45**. Shear stress-pressure relation at different conditions of frequency and temperature.*

The shear stress-temperature and shear stress-frequency relations did not compare well to those of Briscoe and Evans (1982). More data should be obtained to validate the results obtained. The *Eyring Equation* was not developed further due to uncertainties regarding the data and the combination of lubricant with oxides.

# Chapter VI

# CONCLUSIONS AND RECOMMENDATIONS

The transient temperature distribution on a semi-infinite disk due to a circular continuous oscillatory heat source was modelled. Modelling results compared well with those of Wen and Khonsari (2007). At lower Peclet numbers a steady state was reached quicker than at higher Peclet numbers and there was enough time for heat conduction into the body, causing a more distinct rise and fall of temperature on the surface, but a low average (steady) temperature. At high Peclet numbers, the maximum and minimum temperatures were closer together due to the limited time for heat conduction, causing a higher average (steady) temperature. The lower the Peclet number, the higher the maximum obtainable temperature.

The model was used to calculate the contact temperature of a contact similar to what can be expected in the HFRR apparatus. The initial contact temperature of a clean metal contact, at conditions set out by ISO 12156, was calculated as *205°C* at a friction coefficient of *2*, assuming that the size of the contact could be approximated by the Hertzian contact radius. Contact on an asperity with a radius of *1μm* could yield flash temperatures similar to the melting point of the steel for very short durations. High initial temperatures will encourage the formation of hematite and magnetite, which will alter the thermal properties of the interface. Contact temperatures calculated for hematite-hematite and magnetite-magnetite contacts at a friction coefficient of *1* was between *800°C* and *900°C*, assuming that the size of the contact could be approximated by the Hertzian contact radius. The difference in thermal conductivity of the oxides compared to the metal caused the large differences in surface temperature. A rapid temperature drop with increasing contact radius was observed.

There is a slight discrepancy between the ASTM D6079 and ISO 12156 with regard to the laboratory conditions, which could not be cleared up in this investigation. The effect of laboratory conditions is not understood. The theories presented in literature

could not be proved experimentally in this investigation. The poor repeatability of the test method is partially to blame. The other reason was that the laboratory conditions (humidity and temperature) were not controlled. Use of an environmental chamber will help to isolate the effect of humidity.

The model proposed by Fox (2005) was improved and fitted to the *WS1.4* vs. palmitic concentration data. A reasonable fit was obtained. The relationship between the size of the drop in *WS1.4*, the concentration range over which the drop takes place and thermodynamic properties of the lubricant and the surface warrants further study.

*FTIR* of the liquid samples alone could not provide enough information to establish which mechanisms played a role during any test, seeing that the data obtained were not conclusive.

*GC×GC/TOF-MS* showed the formation of hexane and heptane during an HFRR test performed according to the ISO 12156 standard. This is a strong indication of the *catalytic decomposition* of the $C_{16}$-hydrocarbons in the sample, which is most probably also responsible for the loss in volume recorded for all the tests performed.

*Reflectance FTIR microscopy* of the HFRR bottom specimen should be performed to indicate soap formation.

Analysis of the friction and wear mechanism of an unlubricated (dry) HFRR test contact revealed that *oxidative wear* was the prevailing mechanism. A thick layer of fine oxides was responsible for the lubrication. This layer thickened as time progressed leading to decreased friction coefficients with time. *Adhesion* seemed to play a dominant role in the initial stages of the test and *40%* of the final wear scar diameter was reached in the first minute of the *75* minute test. An average percentage film measurement of *94%* was recorded for the unlubricated test, proving that electrical contact resistance is not a very effective means of determining boundary lubricant efficiency. The electrical conductance of magnetite is about *100* times greater than that of hematite, and therefore the high percentage film measured can be attributed to the formation of hematite. *Raman spectroscopy* should be used to verify this.

An analysis of the friction and wear mechanisms of an HFRR contact lubricated with palmitic acid dissolved in n-hexadecane at concentrations of *50 mg/l*, *100 mg/l*, *250 mg/l*, *500 mg/l*, *750 mg/l*, *1000 mg/l*, *1500 mg/l* and *2000 mg/l* revealed that the friction

coefficient remained close to *0,1* for all concentrations above *100 mg/l.* At *0 mg/l*, *50 mg/l* and *100 mg/l* the friction varied between *0,15* and *0,45*. The “friction transition concentration” of palmitic acid was found to be *100 mg/l* in this investigation, which agreed well with literature.

A reaction kinetic study was performed to try and establish the time needed for adsorption of palmitic acid to the surface. Data could be obtained for the reaction of stearic acid on aluminium. It was assumed that the aluminium oxides are more reactive than iron oxides, so the results presented represent the best-case scenario. The time needed for adsorption was longer than the time of a single oscillation and it is concluded that a well-established film will not be formed after the test is started. However the lubricant was still able to provide some protection together with the metal oxides evidently formed in the contact zone. Before the onset of a test there is sufficient time to obtain full coverage at all the additive concentrations tested. An experimental analysis validated the calculation and indicated that the film only lasted around *2* seconds, after which the friction coefficient increased. Apart from the first *2* seconds, all the concentration standards showed friction coefficients far higher than obtained by Tabor (1981) and Briscoe and Evans (1982).

The dynamic analysis of the wear mechanism of *250 mg/l* palmitic acid showed similarities to the unlubricated test. Again the oxidative mechanism was observed but no sign of adhesive wear was visible. *40%* of the final wear scar diameter was also reached within the first minute. The lubricant evidently decreased *adhesion*, which is the most destructive friction and wear mechanism. According to literature this occurs through a mechanism of *junction growth*. The data acquisition system of the HFRR was not sufficiently fast to provide information regarding *junction growth*. Investigation of the friction and wear mechanisms at varying conditions of load, temperature and frequency indicated that lubricated friction was not a result of a lubricant film, but rather a combination of oxides and film with emphasis on the oxides.

A detailed analysis of the wear mechanism inside a common rail diesel injector is recommended, but it is highly unlikely that metal oxide lubrication plays a significant role.

# Chapter VII

# REFERENCES

Adamson, AW (1990) *Physical chemistry of surfaces 5th Edition*, John Wiley & Sons, New York.

Archard, JF (1959) "The temperature of rubbing surfaces", *Wear*, 2, 438-455.

Anastopoulos, G; Lois, E; Karonis, D; Kalligeros, S and Zannikos, F (2005) "Impact of oxygen and nitrogen compounds on the lubrication properties of low sulphur fuels", *Energy*, 30, 415 – 426.

Anastopoulos, G; Lois, E; Zannikos, F; Kalligeros, S and Teas, C (2002) "HFRR lubricity response of an additized aviation kerosene for use in CI engines", *Tribology International*, 35, 599 – 604.

Anastoploulos, G; Lois, E; Zannikos, F; Kalligeros, S and Teas, C (2001) "Influence of aceto acetic acid esters and di-carboxylic acid esters on diesel fuel lubricity", *Tribology International*, 34, 749 – 755.

ASTM D6079 (2005) "Standard Test Method for Evaluating Lubricity of Diesel Fuels by the High-Frequency Reciprocating Rig (HFRR)".

ASTM D975 (2009) "Standard specification for diesel fuel oils".

Barbour, RH; Rickeard, DJ and Elliott, NG (2000) "Understanding diesel lubricity", *SAE Technical Paper Series*, 2000-01-1918.

Bhushan, B (2002) *Introduction to Tribology*, John Wiley & Sons, New York.

Blizard, NC and Bennett, PA (1996) "A comparison of modified elevated temperature HFRR test data with scuffing BOCLE results", *SAE Technical Paper Series*, 961946.

Blok, H (1937) "Theoretical study of temperature rise at surface of actual contact under oiliness lubricating conditions", *Gen. Disn. Lubn. Inst. Mech. Eng.*, 2, 222-235.

Blok, H (1963) "The flash temperature concept", *Wear*, 6, 483-494.

Bowden, FP and Tabor, D (1939) "The area of contact between stationary and between moving surfaces", *Proceedings of the Royal Society of London. Series A, Mathematical and Physical Sciences*, 169, 391 – 413.

Bowden, FP and Tabor, D (1950) *The friction and lubrication of solids*, Oxford University Press, Great Britain.

Briscoe, BJ and Evans, DCB (1982) "The shear properties of Langmuir-Blodgett Layers", *Proceedings of the Royal Society of London. Series A, Mathematical and Physical Sciences*, 380(1779), 389 – 407.

Briscoe, BJ, Scruton, B and Willis, FR (1973) "Shear strength of thin lubricant films", *Proceedings of the Royal Society of London. Series A, Mathematical and Physical Sciences*, 333(1592), 99 – 114.

Carslaw, HS and Jaeger, JC (1959) *Conduction of Heat in Solids 2nd Edition*, Clarendon Press, Oxford University Press, England.

Çengel, YA (2006) *Heat and Mass Transfer A Practical Approach*, McGraw-Hill, Singapore.

Chang, I (2006) “Platform for modeling the boundary lubrication of nominally flat metallic surfaces”, *ASME Journal of Tribology*, 128, 677-680.

Chen, SH and Frank, CW (1989) “Infrared and fluorescence spectroscopic studies of self-assembled n-alkanoic acid monolayers”, *Langmuir*, 5(4), 978 – 987.

EN 590 (2008) “Automotive fuels – Diesel – Requirement and test methods”.

Fox, MF (2005) “A model for diesel fuel additive lubricity”, *Life cycle tribology. Proceedings of the 31st Leeds-Lyon Symposium on Tribology*, 48, 585 – 591.

Glovnea, RP; Forrest, AK; Olver, AV and Spikes, HA (2003) “Measurement of sub-nanometer lubricant films using ultra-thin film interferometry”, *Tribology Letters*, 15(3), 217 – 230.

Gonnet, P (2010a) “Increasing the reliability of adaptive quadrature using explicit interpolants”, *ACM Transactions on Mathematical Software* (in press).

Gonnet, P (2010b) “Numerical integration”, Personal Communication, Mathematical Institute, University of Oxford.

Greenwood, JA and Alliston-Greiner, AF (1992) “Surface temperatures in a fretting contact”, *Wear*, 155, 269 – 275.

Greenwood, JA and Williamson, JBP (1966) “Contact of nominally flat surfaces”, *Proceedings of the Royal Society of London. Series A. Mathematical and Physical Sciences*, 295(1442), 300 – 319.

Hamrock, BJ; Schmid, SR and Jacobson, BO (2004) *Fundamental of Fluid Film Lubrication 2nd Edition*, Marcel Dekker Inc., USA.

Heinkenschloss, M (2002) “romberg.m”, *Matlab Code*, http://www.caam.rice.edu/~caam353/matlab/integ/romberg.m [2010, July 20].

Hu, Y and Zhu, D (2000) “A full numerical solution to the mixed lubrication in point contacts”, *Journal of Tribology*, 122, 1 – 9.

ISO 12156-1 (2003) “Diesel fuel – Assessment of lubricity using the high-frequency reciprocating rig (HFRR) – Part 1: Test method”.

ISO 12156-2 (2005) “Diesel fuel – Assessment of lubricity using the high-frequency reciprocating rig (HFRR) – Part 2: Limit”.

Jaeger, JC (1943) “Moving sources of heat and the temperature at sliding contacts”, *Proc. Roy. Soc.*, 76, 203 – 224.

Jost, HP and Scofield, J (1981) “Energy savings through tribology: A techno-economic study”, *Proc. Inst. Mech. Engrs.*, 195(16), 151 – 173.

Kajdas, C; Makowska, M and Gradkowski, M (2006) “Tribochemistry of n-hexadecane in different material systems”, *Lubrication Science*, 18, 255 – 263.

Ketteler, G; Weiss, W; Ranke, W and Schögl (2001) “Bulk and surface phases of iron oxides in an oxygen and water atmosphere at low pressure”, *Physical Chemistry Chemical Physics*, 3, 1114 - 1122.

Kirchnerová, J and Cave, GCB (1976) “The solubility of water in low-dielectric solvents”, *Can. J. Chem.*, 54, 3909 – 3916.

Knothe, G and Steidley, KR (2005) “Lubricity of components of biodiesel and petrodiesel. The origin of biodiesel lubricity”, *Energy and Fuels*, 19, 1192 – 1200.

Lacey, PI; Gunsel, S; De La Cruz, J and Whalen, MV (2001) "Effects of high temperature and pressure on fuel lubricated wear", *SAE Technical Paper Series*, 2001-01-3523.

Ludema, KC (1996) *Friction, Wear, Lubrication. A textbook in Tribology*, CRC Press Inc., Florida, USA.

Margaroni, D (1998) "Fuel lubricity", *Industrial Lubrication and Tribology*, 50(3), 108-118.

MatWeb Material Property Data (2010) "Properties of AISI E-52100 steel", www.matweb.com [2010, July 20].

Matzke, M; Litzow, U; Jess, A; Caprotti, R and Balfour, G (2009) "Diesel lubricity requirements of future fuel injection equipment", *SAE Technical Paper Series*, 2009-01-0848.

Mølgaard, J and Smeltzer, WW (1971) "Thermal conductivity of magnetite and hematite", *Journal of Applied Physics*, 42(9), 3644 – 3647.

Nikanjam, M (1999) "Diesel fuel lubricity: On the path to specifications", *SAE Technical Paper Series*, 1999-01-1479.

Oláh, ZS, Szirmai, L and Resofszki, G (2005) "Micro and Nano Analysis of Wear Scar Surfaces – A Complementary Rating Method to the Evaluation of HFRR Test Results", MOL, Hungarian OIL and Gas plc., Százhalombatta, Hungary.

Onion, G and Suppeah (1984) "The generation and properties of boundary films formed by diesel fuel at a steel/steel conjunction", *Tribology International*, 17(5), 277 – 287.

PCS Instruments (2005) HFRR Installation & Test Preparation Manual, Hardware Version 1.

Perry, RH and Green, DW (1997) *Perry's Chemical Engineers' Handbook 7th Edition*, McGraw-Hill Companies Inc., USA.

Pourbaix, M (1966) *Atlas of electrochemical equilibria in aqueous solutions*, Pergamon Press, Oxford, England.

Rajagopal, KR and Szeri, AZ (2003) "On an inconsistency in the derivation of the equations of elastohydrodynamic lubrication", *Proc. R. Soc. Lond.*, 459, 2771-2786.

Rashmi, R; Sahoo, SK and Biswas, SK (2009) "Frictional response of fatty acids on steel", *Journal of Colloid and Interface Science* (in press).

Reynolds, O (1886) "On the theory of lubrication and its application to Mr. Beauchamp Tower's experiments, including an experimental determination of the viscosity of olive oil", *Philosophical Transactions of the Royal Society of London*, 177, 157-234.

Schaberg, PW; Morgan, PM, Myburgh, IS and Botha, JJ (1999) "An overview of the production, properties and exhaust emissions performance of Sasol slurry phase distillate diesel fuel," *TAE99*, Esslingen, Germany.

Selwood, PW (1975) *Chemisorption and Magnetization*, Academic Press Inc., New York.

Shampine, LF (2008) "Vectorized adaptive quadrature in Matlab", *Journal of Computational and Applied Mathematics*, 211, 131 - 140.

Skoog, DA; Holler, FJ and Nieman, TA (1998) *Principle of Instrumental Analysis 5th Edition*, Brooks/Cole Thomson Learning, USA.

Stachowiak, GW and Batchelor, AW (2005) *Engineering Tribology 3rd Edition*, Elsevier Butterworth-Heinemann, USA.

Spikes, HA (1993) “Boundary lubrication and boundary films”, *Tribology Series, Thin Films in Tribology, Proceedings of the 19th Leeds-Lyon Symposium on Tribology held at the Institute of Tribology, University of Leeds*, 25, 331 – 346.

Spikes, HA (2004) “Frontiers in liquid lubrication”.

Stokes, GG (1845) “On the theories of the internal friction of fluids in motion, and of the equilibrium and motion of elastic solids”, *Transactions of the Cambridge Philosophical Society*, 8(22), 287 – 342.

Subhalakshmi, K; Devaprakasam, D; Math, S and Biswas, SK (2008) “Use of the Eyring equation to explore the frictional responses of a $–CF_3$ and a $-CH_3$ terminated monolayers self-assembled on silicon substrate”, *Tribology Letters*, 32, 1 – 11.

Szeri, AZ (1998) *Fluid Film Lubrication Theory & Design*, Cambridge University Press, Cambridge, UK.

Tabor, D (1959) “Junction growth in metallic friction: The role of combined stresses and surface contamination”, *Proceedings of the Royal Society of London. Series A, Mathematical and Physical Sciences*, 251(1266), 378 – 393.

Tabor, D (1981) “The role of surfaces and intermolecular forces in thin films lubrication”, *Tribology Series*, *Microscopic Aspects of Adhesion and Lubrication, Proceedings of the 34th International Meeting of the Société de Chimie Physique,* 7, 651 – 682.

Tannhauser, DS (1962) “Conductivity of iron oxides”, *Journal of the Physics and Chemistry of Solids*, 23, 25 – 34.

Tian, X and Kennedy, FE (1994) “Maximum and average flash temperatures in sliding contacts”, *ASME Journal of Tribology*, 116, 167 – 174.

Timsit, RS and Pelow, CV (1992) “Shear strength and tribological properties of stearic acid films”, *ASME Journal of Tribology*, 114, 150 – 166.

Tower, B (1883) “First report on friction experiments”, *Proc. Inst. Mech. Engrs.*, 632 – 659.

Tsonopoulos, C (1999) “Thermodynamic analysis of the mutual solubilities of normal alkanes and water”, *Fluid Phase Equilibria*, 156, 21 – 33.

Wei, D and Spikes, HA (1986) “The lubricity of diesel fuels”, *Wear*, 111, 217 – 235.
Weideman, JAC (2002) “Numerical integration of periodic functions: A few examples”, *The American Mathematical Monthly*, 109(1), 21 – 36.

Wen, J and Khonsari, MM (2007) “Transient temperature involving oscillatory heat source with application in fretting contact”, *ASME Journal of Tribology*, 129, 517 – 527.

White, FM (2006) *Viscous Fluid Flow 3rd Edition*, McGraw-Hill, Singapore.

World Wide Fuels Charter (2002).

Yoshizawa, HI; Chen, YL and Israelachvili, J (1993) “Fundamental mechanisms of interfacial friction. 1. Relation between adhesion and friction”, *Journal of Physical Chemistry*, 97, 4128 – 4140.

Zhmud, B and Roegiers, M (2009) “New base oils pose a challenge for solubility and lubricity”, *Tribology and Lubrication Technology*, 2009(7), 34 – 39.